PLANAR RASTER-SCANNING SYSTEM FOR NEAR-FIELD MICROWAVE IMAGING

PLANAR RASTER-SCANNING SYSTEM FOR NEAR-FIELD MICROWAVE IMAGING

By

HAOHAN XU, B.ENG.

A Thesis

Submitted to the School of Graduate Studies

in Partial Fulfillment of the Requirements

for the Degree

Master of Applied Science

McMaster University

MASTER OF APPLIED SCIENCE (2011) McMaster University
(Electrical and Computer Engineering) Hamilton, Ontario

TITLE: **Planar Raster-scanning System for Near-field Microwave Imaging**

AUTHOR: HaoHan Xu
B.Eng. (Electrical and Biomedical Engineering,
McMaster University, Hamilton, Canada)

SUPERVISORS: Natalia K. Nikolova, Professor,
Department of Electrical and Computer Engineering, McMaster University
Dipl.Eng. (Technical University of Varna)
Ph.D. (University of Electro-Communication)
P.Eng. (Province of Ontario)
Fellow, IEEE

NUMBER OF PAGES: XXI**,** 192

ABSTRACT

Microwave imaging is a promising new imaging modality under research for breast cancer detection. This technique images/reconstructs the internal dielectric composition of the breasts and relies on the contrast between the dielectric properties of malignant tissues and healthy tissues to pinpoint the abnormality. Over the years, new imaging algorithms were proposed and many imaging systems were developed in accordance. However, none of the proposed systems has made it to the market.

In this thesis, a prototype planar raster-scanning system for near-field microwave imaging is presented. This system measures the scattering parameters while scanning a 2-D plane over the imaged object (phantom) in a raster pattern. The development of this system aids significantly in our research of microwave imaging for breast cancer detection because it enables us to carry out numerous experiments and to develop and verify new imaging algorithms.

Our contribution also lies in conducting a comprehensive study of the dynamic range of the developed system. Each source of noise/uncertainty from the system is identified and studied for the benefits of future improvements.

Typical imaging results of phantoms with different dielectric properties are also provided to showcase the performance of the developed system.

ACKNOWLEDGEMENTS

It is a great pleasure for me to acknowledge many people who made this thesis possible.

First and foremost I would like to express my sincere gratitude to my supervisor, Dr. Natalia K. Nikolova for her expert supervision and guidance, continuous support and patience during the course of this work. I am grateful for the opportunity given by Prof. Nikolova to be part of the Computational Electromagnectics Laboratory and study in an upcoming research area. For the past two years, her patience, motivation, enthusiasm and immense knowledge have contributed a lot to my personal growth. I could not have imagined having a better advisor for my M.A.Sc. study.

I also want to express my gratitude to Tyler Ackland and Robert Zimmerman for the help in assembling the scanner. Tyler's expertise in electrical components is invaluable in successful completion of this work. My sincere thanks also go to Prof. Mohamed Bakr and Prof. James Reilly from whose lectures I benefited greatly. I also want to thank all the colleagues and friends

from Computational Electromagnectis Laboratory for all the interesting discussions and fruitful comments and for making our laboratory a pleasant work place.

Last but not least I want to express my deepest love to my parents for their constant encouragement and endless support. Without their support, I would never reach this far.

CONTENTS

LIST OF FIGURES

CHAPTER 1

INTRODUCTION

Microwave imaging has long been viewed as a promising technique in applications such as medical imaging, non-invasive testing, sub-surface sensing and concealed weapon detection [1][2][3]. However, despite the ample published literatures on the subject, the current state is that microwave imaging is still widely regarded as an emerging modality since many practical issues exist and mature imaging systems are yet to be developed and commercialized. This holds true especially in the case of medical imaging.

1.1. Overview of Microwave Imaging Setups

The goal of microwave imaging is basically to image/reconstruct the internal dielectric composition of the imaged object from measured microwave

signals scattered from or generated by the imaged object. In the first case, the object scatters the incident field generated by the acquisition system. This is the case of active microwave imaging. In the second case, which is relevant in tissue imaging, the imaged organ naturally generates microwave radiation depending on the internal temperature. This is the case of passive microwave imaging. This thesis focuses on the active microwave imaging approaches. Based on the type of applications and algorithms embedded, the implementations of active microwave imaging system have several different approaches, each of them is described below.

For sub-surface imaging applications, a pioneering imaging system was proposed back in 1973 [4]. It employs a radiating horn and an elemental dipole antenna as transmitter/receiver. The data acquisition is done with the transmitter/receiver unit scan over a 2-D aperture on one side of the target. For medical applications, pioneering work was done in the 1979 by Larsen *et al*. [5]. They developed a water-immersed imaging setup, with which they successfully imaged a canine kidney [6]. In this imaging setup, two horn antennas are immersed in a water tank aligned along each other's boresight. The object to be imaged is scanned in between the antennas in a raster pattern. Other proposed imaging system using raster-scanning approaches were developed for sub-surface sensing [7], breast cancer detection [8][9]. Even though all these setups ([4] to [10]) use raster scanning approach in the data acquisition, the actual imaging systems do have several differences. For the systems proposed in [5] and [9],

(both for medical applications), the sensors are placed on both sides of the object to be imaged, which means that both scattered field and transmitted field can be obtained. During the measurements, the two antennas move together in the raster pattern. The schematic of this kind of scanning setup is shown in Fig. 1.1. For the systems proposed in [4][7] (sub-surface sensing) and [8] (medical application), the transmitter and receiver are located on the same side of the target, and move simultaneously during measurements. In this way, only the scattered field can be obtained. The schematic is shown in Fig. 1.2. There is another special case of a raster scan, which is proposed in [10]. In this setup, sensors are located on both sides of the target. However, during the scan, one of the sensors is kept fixed while the other one moves in the raster pattern. The schematic is shown in Fig. 1.3.

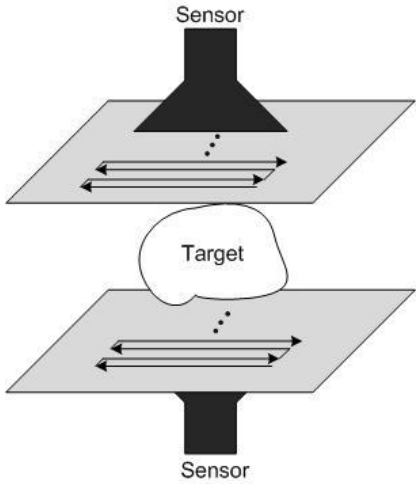

Fig. 1.1. Schematic for the raster-scanning setup with sensors on both sides of the target. The two sensors move together while being aligned along each other's boresight.

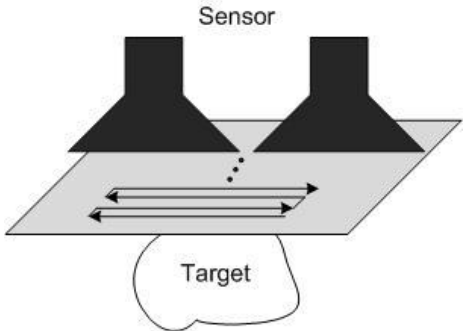

Fig. 1.2. Schematic for the raster-scanning setup with both transmitter and receiver on one side of the target. The two sensors move together in the raster pattern.

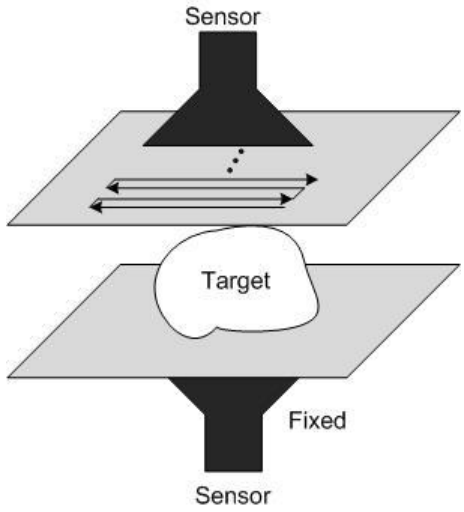

Fig. 1.3. Schematic for the raster-scanning setup with sensors on both sides of the target. One sensor is kept fixed and the other sensor moves in the raster pattern.

Despite the planar-scanning approaches described above, there is also another type of scan approach, cylindrical surface scan approach, which is used in [15]. In this implementation, a single sensor is used to both transmit and receive the back scattered signal. The transceiver is installed on a vertical placed rail, which can then move vertically. The target is placed on top of a rotating motor. With this configuration, the system can effectively scan the outer circumference

of a cylinder containing the target for back scattered signal. The schematic is shown in Fig. 1.4.

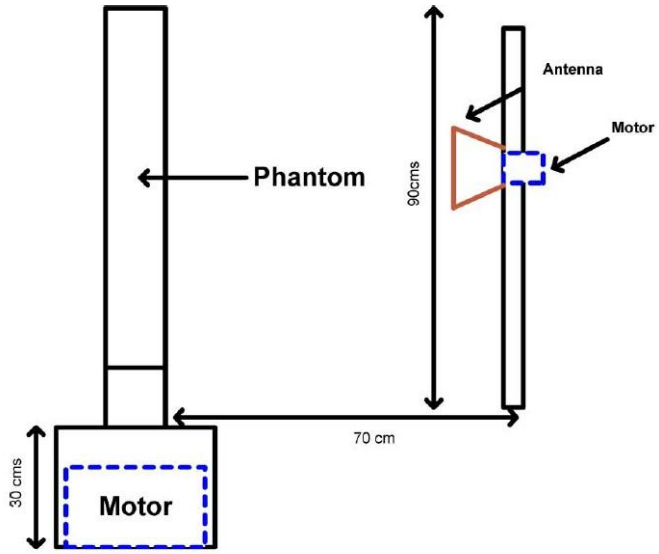

Fig. 1.4. Schematic of the cylindrical scan system (from [15]).

Another imaging approach found in the literatures is the multi-static approach, which exploits an antenna array. This technique employs electronically switched antennas in an array, eliminating the need to move the sensors or the object during a measurement. Based on the specific applications, the shapes of the array are different. In [11] and [12], the array is built to form a focused beam using Vivaldi antennas, and it is suitable for sub-surface sensing. In [13] and [14], both proposed imaging systems are for medical application, in particular, breast-cancer detections. Although antennas used in these two cases are different, [13] uses bow-tie antenna and [14] uses dipoles, the antenna array is in the same circular shape, with the target (breast) placed within. The schematic showing this kind of setup is in Fig. 1.5. In this case, both forward and back scattered signal

can be measured. Also, in the case of 3-D imaging, the circular array is scanned vertically along the target to acquire slices of the imaging object.

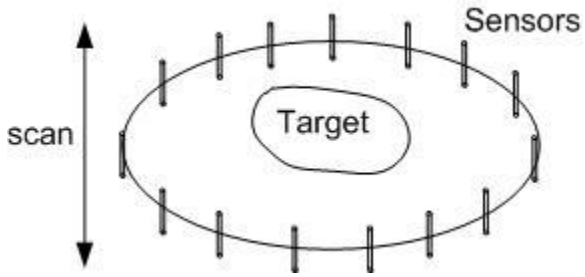

Fig. 1.5. Schematic for multi-static antenna array approach.

Another type of imaging system using multi-static approach is seen in [16]. This type of approach is designed particularly for breast-cancer detection. In this implementation, imaging sensors are placed on a hemi-spherical surface, which is used to constrain the breast to be imaged. The illustration for this system is shown in Fig. 1.6.

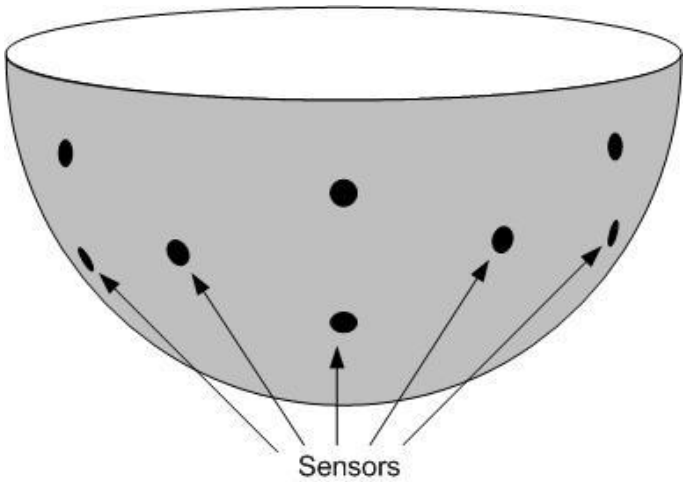

Fig. 1.6. Schematic for hemi-spherical multi-static antenna array approach.

In [17], an array-scan hybrid approach is proposed for the application of concealed weapon detection. It has a fixed linear array of transceivers parallel to

the ground. During operation, this array scans over vertical direction, combined with electronically switched array components, the full 2-D plane data are acquired. The scan configuration is shown in Fig. 1.7.

Although, there are several different approaches in data acquisition, they all can be categorized as either scanning or multi-static approaches.

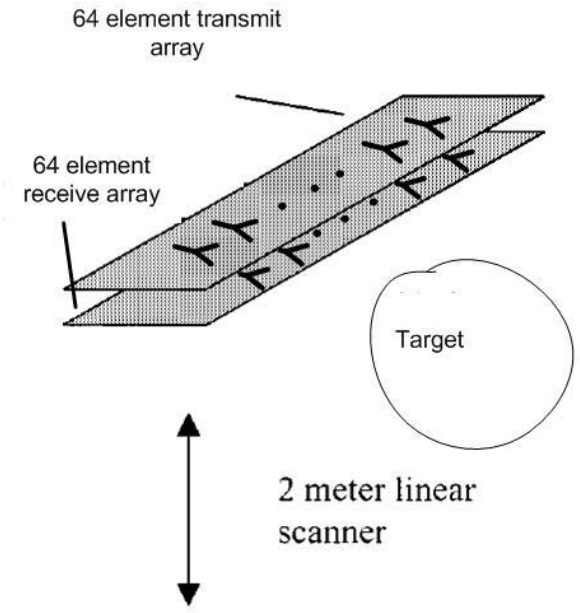

Fig. 1.7. Illustration of the array-scan hybrid setup in [17].

1.2. Comparison between Scanning and Array

The scanning approach and the multi-static array approach each has its own advantages and disadvantages.

The scanning approach needs only one set of transmitter/receiver antennas. This eliminates the need for RF switches and leads to substantially smaller cost in making the sensors as compared to the antenna-array technique. This technique is also the only option when the sensors are large, i.e. larger than the required spatial sampling rate. In addition, in the scanning approach, the spatial sampling rate is adjustable and can be controlled by the scanning mechanism. In contrast with an antenna array, the spatial sampling distance is fixed.

However, the scanning technique does suffer from the need to use moving mechanical parts. This brings along some problems.

(1) Mechanical scanning complicates the design of the overall imaging system.

(2) The moving parts of the scanning setup are likely to introduce uncertainties in the measurement, which may affect the overall dynamic range of the system.

(3) Scanning data acquisition is slower than the acquisition with an electronically switched antenna array.

Items 1 and 2 are manageable by carefully designing the system. Item 3 is an intrinsic problem in applications which require very quick data acquisition. The biggest drawback in multi-static approach on the other hand, is the impossibility to adjust spatial sampling rate, or to employ relatively large sensors. Thus, in our case, we select the scanning approach and implement a complete imaging system based on it. In particular, we developed a planar raster-scanning imaging system.

1.3. Outline of the Thesis

Chapter 2 covers the design and the implementation of the raster-scanning setup. It first describes the hardware with detailed drawings and specifications. Then the software implementation of the control of the system is discussed. Lastly, issues with the current setup and possible improvements are discussed.

Chapter 3 focuses on the study of the dynamic range of the implemented imaging system. First, it analyzes the intrinsic noise floor of the VNA, which represents the minimum uncertainty level associated with the system. Then, several factors that could affect the uncertainty level (dynamic range) of the system are discussed. These include the use of low-noise amplifier (LNA) and the uncertainties associated with the mechanical motion during measurements. Finally, the chapter presents assessments on the uncertainty level obtained in full scan measurements.

Chapter 4 focuses on presenting the results obtained from the imaging system. It first compares the measured results with the simulation results. Then, it presents some of the typical imaging results obtained from full scan measurements of phantoms with different dielectric properties.

For convenience, the thesis concludes with chapter 5 with a summary and recommendations for future work. A list of components and the user manual of the implemented imaging setup are given in the Appendix A and Appendix B, respectively. The dielectric properties of the phantoms used in this thesis is given

in Appendix C. A summary of the bibliography is also given in the end of the thesis.

1.4. Contributions

The author has contributed substantially to the following original developments presented in the thesis:

(1) Designed and built an imaging system which can provide automated planar raster-scanning measurements through Matlab or LabView control (The LabView control portion isn't entirely completed).

(2) Constantly improving the capability and reliability of the built system.

(3) Studied the dynamic range of the built system, which ensures the reliability of measurement data.

(4) Collected extensive measurements data for various purposes. Parts of the measurements contributed to publications of [18] and [19].

References

[1] M. Pastorino, *Microwave Imaging.* Hoboken, NJ: John Wiley & Sons, 2010, pp.1–3.

[2] L.E. Larsen and J.H. Jacobi, "Microwave interrogation of dielectric targets. Part I: By scattering parameters," *Med. Phys.*, vol. 5, no. 6, 1978, pp. 500–508.

[3] J.-C. Bolomey and C. Pichot, "Microwave tomography: From theory to practical imaging systems," *Int. Journal of Imaging Systems and Technology*, vol. 2, pp. 144–156, 1990.

[4] R.D. Orme and A.P. Anderson, "High-resolution microwave holographic technique. Application to the imaging of objects obscured by dielectric media," *Proc. IEE*, vol. 120, no. 4, pp. 401–406, April 1973.

[5] L.E. Larsen, J.H. Jacobi and C.T. Hast, "Water-immersed microwave antennas and their application to microwave interrogation of biological targets," *IEEE Trans. Microwave Theory Tech.*, vol. MTT-27, no. 1, pp. 70–78, Jan. 1979.

[6] L.E. Larsen and J.H. Jacobi, "Microwave scattering parameter imagery of an isolated canine kidney" *Med. Phys.*, vol. 6, pp. 394–403, 1979.

[7] G. Junkin and A.P. Anderson, "Limitations in microwave holographic synthetic aperture imaging over a lossy half-space," *IEE Proc. F Communications, Radar and Signal Processing, ,* vol. 135, no. 4, pp. 321–329, August 1988.

[8] M. Elsdon, M. Leach, S. Skobelev and D. Smith, "Microwave holographic Imaging of breast cancer," *2007 Int. Symp. Microwave, Antenna, Propagation and EMC Technologies for Wireless Communications*, pp.966–969, Aug. 2007.

[9] R.K. Amineh, M. Ravan, A. Trehan and N.K. Nikolova, "Near-field microwave imaging based on aperture raster scanning with TEM horn antennas," *IEEE Trans. Antennas and Propagation*, vol. 59, no. 3, pp.928–940, Mar. 2011.

[10] H. Kitayoshi, B. Rossiter, A. Kitai, H. Ashida and M. Hirose, "Holographic imaging of microwave propagation," *IEEE MTT-S Int. Microwave Symposium Digest*, vol. 1, pp. 241–244, 1993.

[11] F.-C. Chen and W.C. Chew, "Time-domain ultra-wideband microwave imaging radar system," *Proc. of IEEE Instrumentation and Measurement Technology Conference 1998 (IMTC '98)*, vol. 1, pp. 648–650, May 1998.

[12] F.-C. Chen, W.C. Chew, "Microwave imaging radar system for detecting buried objects," *IEEE International Geoscience and Remote Sensing Symposium 1997 (IGARSS '97)*, vol. 4, pp. 1474–1476, Aug 1997.

[13] C.-H. Liao, L.-D. Fang, P. Hsu and D.-C. Chang, "A UWB microwave imaging radar system for a small target detection," *IEEE Antennas and Propagation Society International Symposium 2008 (APS 2008)*, pp.1–4, July 2008.

[14] P.M. Meaney *et al*., "A clinical prototype for active microwave imaging of the breast," *IEEE Trans. Microwave Theory and Techniques*, vol. 48, no. 11, 2000.

[15] D. Flores-Tapia, G. Thomas and S. Pistorius, "A wavefront reconstruction method for 3-D cylindrical subsurface radar imaging," *IEEE Trans. Image Processing*, vol. 17, no. 10, pp. 1908–1925, Oct. 2008.

[16] M. Klemm, I.J. Craddock, J.A. Leendertz, A. Preece, and R. Benjamin, "Radar-based breast cancer detection using a hemispherical antenna array—experimental results," *IEEE Trans. Antennas and Propagation*, vol. 57, No. 6, pp. 1692–1704, Jun. 2009.

[17] D.M. Sheen, D.L. McMakin and T.E. Hall, "Three-dimensional millimeter-wave imaging for concealed weapon detection," *IEEE Trans. Microwave Theory and Techniques*, vol. 49, no. 9, pp. 1581–1592, Sep 2001.

[18] R.K. Amineh, K. Moussakhani, H.H. Xu, M.S. Dadash, Y. Baskharoun, L. Liu and N. K. Nikolova, "Practical issues in microwave raster scanning," *Proc. of the 5th European Conference on Antennas and Propagation (EUCAP 2011)*, pp. 2901–2905, April 2011.

[19] A. Khalatpour, R.K. Amineh, H.H. Xu, Y. Baskharoun, N.K. Nikolova, "Image quality enhancement in the microwave raster scanning method," *International Microwave Symposium (IMS 2011)*, June 2011.

CHAPTER 2

IMPLEMENTATION OF THE RASTER-SCANNING IMAGING SYSTEM

Introduction

Planar raster-scanning is a common method used in microwave imaging, e.g., in microwave holography. The idea is similar to the raster scan technique used in conventional television where images are formed by electron beams sweeping across the screen in a raster order. In the microwave imaging experimental setup, however, the scenario is such that two transmitting/receiving antennas each are

placed on the opposite side of the medium to be studied facing each other. The two antennas then move coherently in a raster pattern to obtain measurements from the medium.

While there are numerous commercial X-Y tables in the market, none of them is suitable for the specific measurement tasks that we perform. Thus, a custom-made planar raster-scanning setup is developed and tested.

2.1 Design Constraints and Requirements

According to [1], a modern microwave imaging setup should have these properties:

- providing adequate data (spatial sampling rate, frequency range, etc.) with respect to the basic requirements of the processing technique to be used;
- obtaining sufficient accuracy with respect to the environmental perturbations and constraints for the considered application;
- as rapid as possible; and
- accommodating cost constraints.

The properties listed above are only guidelines. By combing them with our specific requirements, we have a new set of constraints and requirements for the system to be built:

(1) Positioning precision: The accumulated errors during a scan should be minimal. Scan results should be highly repeatable.

(2) Fast motion: The whole measurement process for a 10 by 10 cm^2 phantom with 5 mm step length should be within 30 min.

(3) Adjustable antenna and phantom mount: For measurements of phantoms with different thicknesses.

(4) Fail-safe: Should the system fail, the power should be cut down preventing overheating of the electrical components.

(5) Easy recovery: Should the system fail, there should be an easy recovery process (e.g., with a press of a button).

(6) User friendly interface: Easily configurable and self explanatory control software.

(7) Reasonable cost.

2.2 Overview of the Final Design

The complete raster-scanning setup consists of a raster-scanning table, a vector network analyzer (VNA), a personal computer (PC), microwave imaging antennas sensors, power supplies and cable connectors, etc. A simplified block diagram of the system is shown in Fig. 2.1. Also, a picture of the completed raster-scanning system is shown in Fig. 2.2.

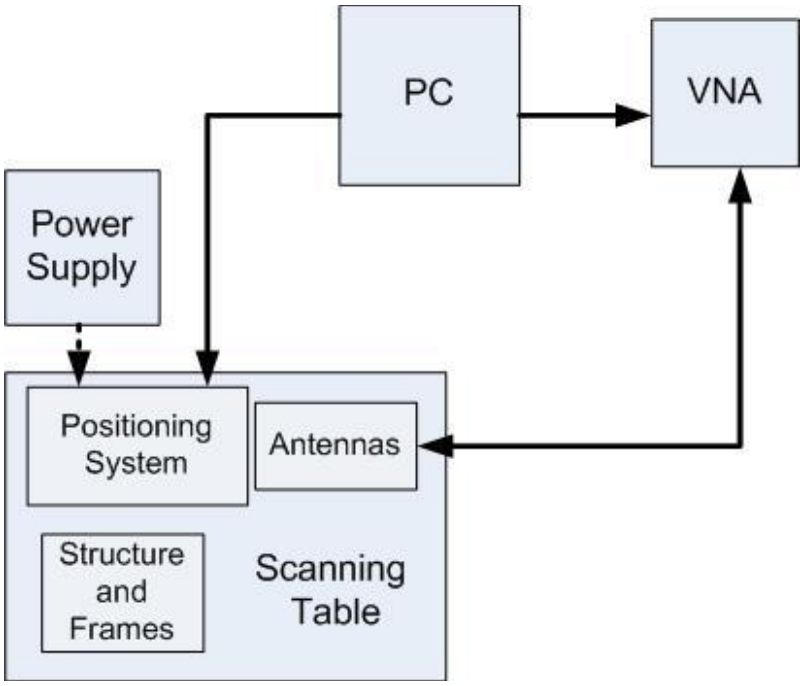

Fig. 2.1. Block diagram of the raster-scanning setup.

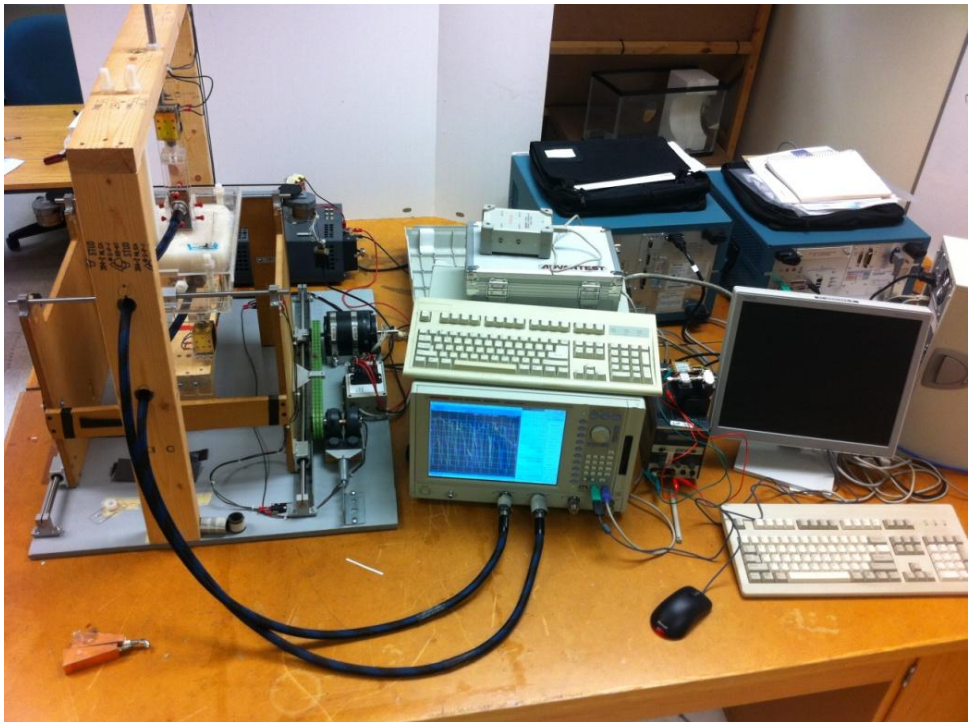

Fig. 2.2. The completed scanning setup.

The operation of this raster-scanning system is simple. A PC controlled scanning table carrying the testing phantom moves in a raster pattern in a 2-D plane. It stops at each sampling point for the VNA to take measurements. Note that in this configuration, the antennas are fixed relative to the lateral plane and it is the tested object (phantom) which is moving in a raster pattern. The fact that the antennas are fixed and the phantom moves is due to two reasons. First, microwave imaging measurements require high precision. Moving the antennas around changes the position and curvature of the RF cables which is likely to introduce higher uncertainty in comparison with a system where the tested object moves. Second, the high quality coaxial cables connecting the antennas and the VNA are heavy and stiff, which makes them rather difficult to move.

2.3 Hardware Implementation

In this section, the hardware implementation of the setup is described. It is divided into 3 parts: raster-scanning table, control and power circuits, fail-safe circuit.

2.3.1 Raster-scanning Table

1) Main frame

The main frame of the scanner (Fig. 2.3) is made of composite board. It is mounted on two rails driven by a heavy duty step motor (big motor) in the X direction. Two additional rails are installed on top of the scanner frame and two pieces of flat plexiglass plates are mounted on these rails to carry the phantom

(phantom holder). In addition, a small step motors is installed on each end of one of the top rails. These two small step motors are used to move the plexiglass in Y direction. One of the small motor is a dummy as it is used only to hold the timing belt in place. With both the big motor and the small motors working together, the scanning table can move to any position in a 2-D plane. The structure is described in more detail in Figs. 2.4 to 2.6. The dimensions of the scanner frame as well as the phantom holder are described in Appendix A.

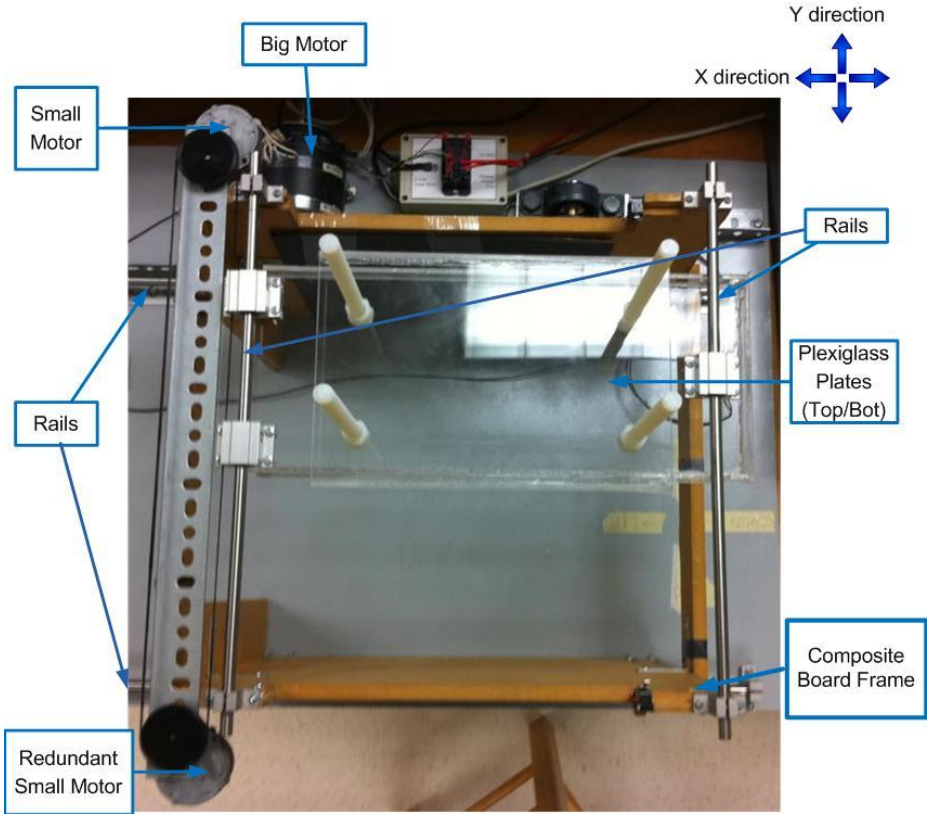

Fig. 2.3. Main frame in top view.

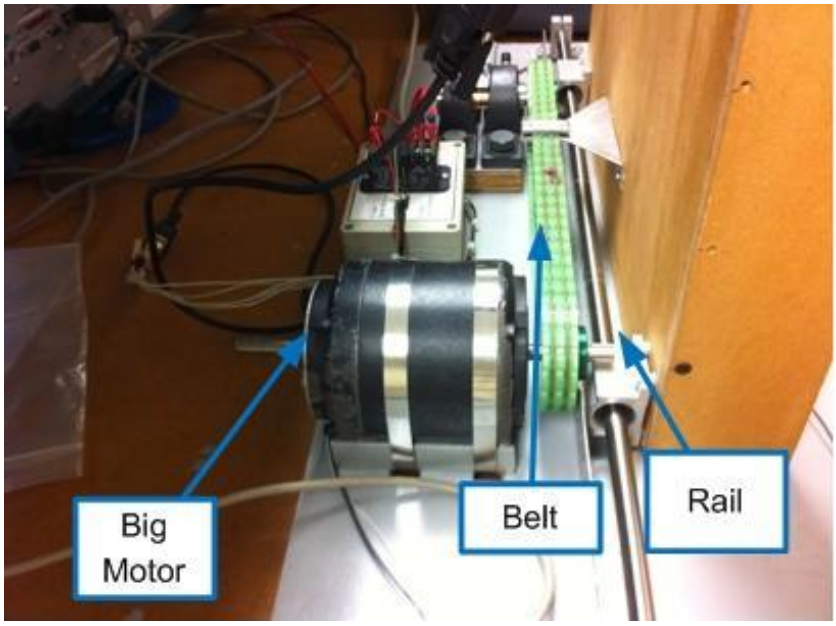

Fig. 2.4. Large motor and belt driving the composite board frame.

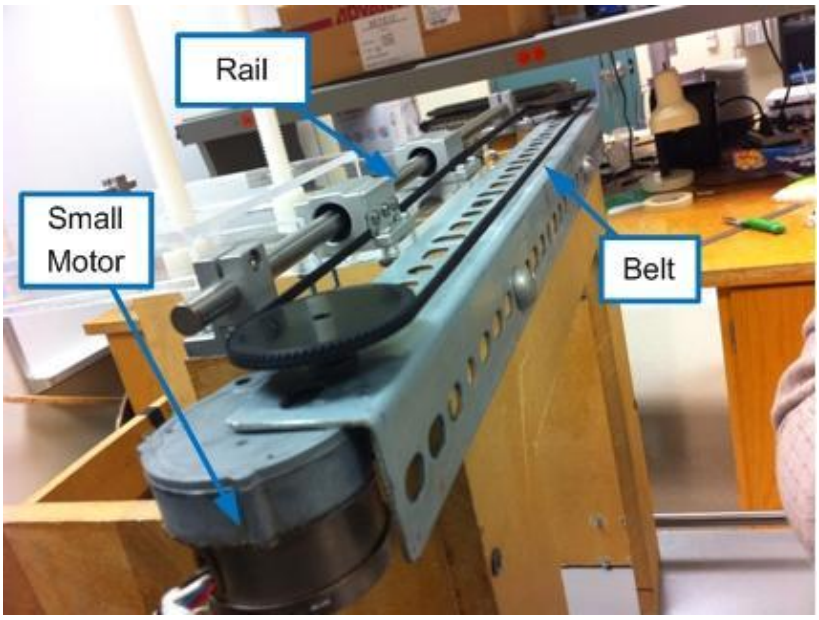

Fig. 2.5. Small motor and belt driving the rails with the plexiglass plates.

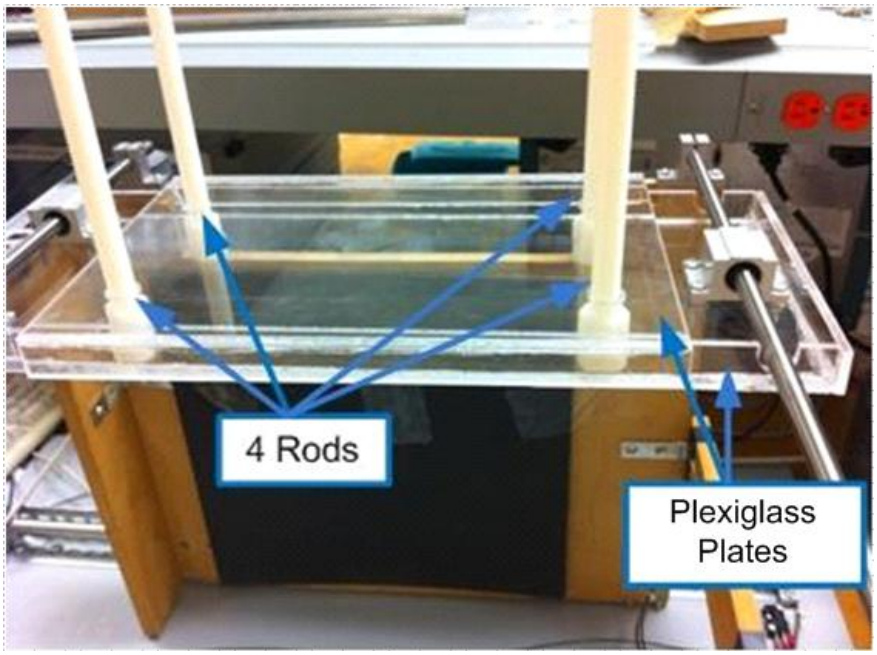

Fig. 2.6. Phantom holder made from plexiglass.

The phantom holder is made of two pieces of plexiglass plates. A phantom is inserted between the plates and four rods with nuts are then used to fix it in place. This gives flexibility in holding phantoms of different thickness.

Fig. 2.7 shows a phantom placed between the two plexiglass plates. Two nuts are screwed in from both ends of the rods to fix the phantom in place. The black sheet in front of the phantom is a sheet of microwave absorber. Absorbing sheets are placed on all four exposed sides of the phantom during measurements to reduce ambient noise and to suppress RF leakage along the phantom-air interface.

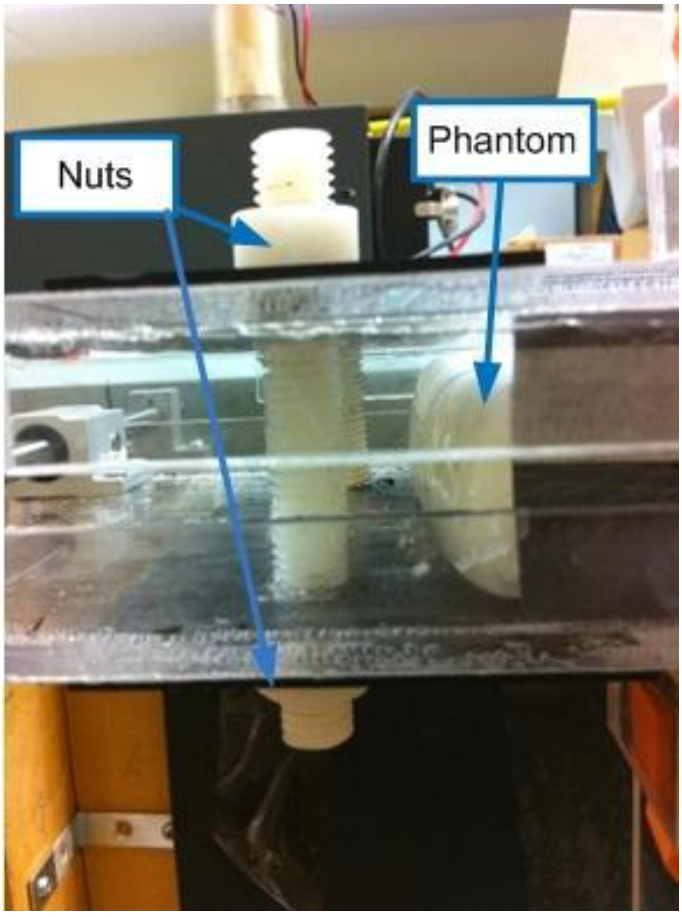

Fig. 2.7. Close-up of the rod tightening the plates on both sides of the phantom.

2) Antenna mount

The antenna mount is shown in Fig. 2.8. It is a square shaped wooden frame with a branch arm in the lower left part of the frame. The frame is rigid with three holes drilled on the top arm. Through these three holes, three rods are installed. One rod is used to mount the solenoid and the antenna. The other two rods, together with a plastic slab, are used to form a bracket supporting the weight of the coaxial cable. There are also two holes drilled on the right arm for the two coaxial cables to go through. In addition, the branch arm serves as a support for the bottom antenna which is also fixed to a rod. Initially, the rods used to mount the antennas and the solenoids were made of plastic. However, during measurements, the plastic rod turned out to be not rigid enough to hold the solenoids and the antennas in place. Thus, these two rods were changed to metal rods to provide much sturdier mount.

A close view of the antenna mount is shown in Fig. 2.9. The top antenna is placed in an antenna holder. The antenna holder is fixed to the end of a solenoid which is fixed to the metal rod (not shown in this figure). The coaxial cable connects to the top antenna from the right and is supported by a plastic slab attached to the end of two rods. The bottom antenna is also attached to the end of a solenoid which is fixed to the metal rod from the branch arm. Close-ups for each part are shown in Figs. 2.10 and 2.11.

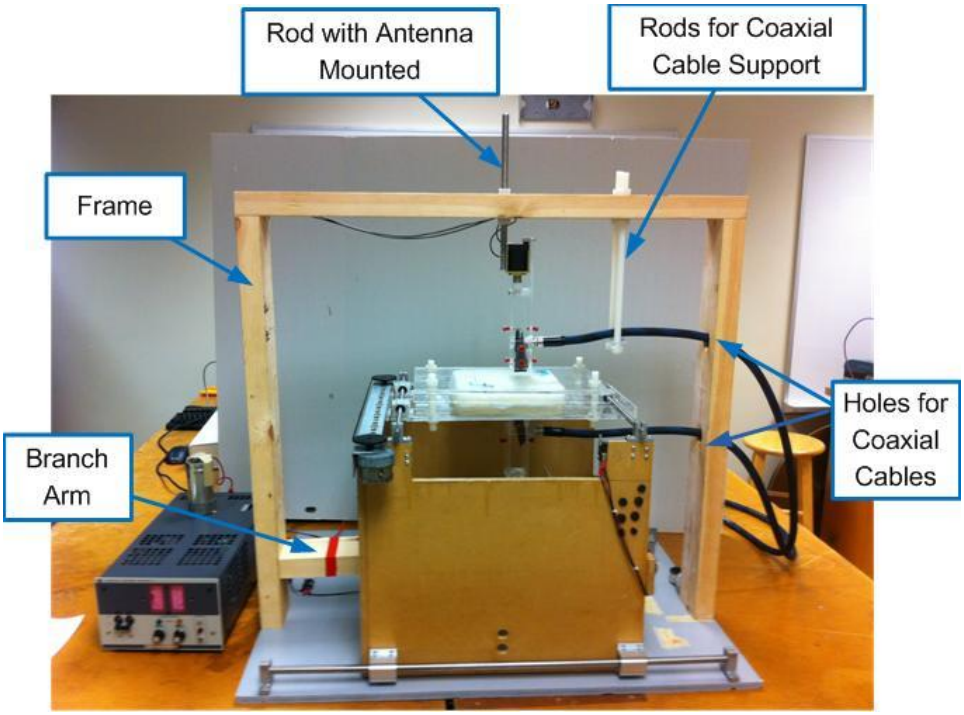

Fig. 2.8. Antenna mount frame.

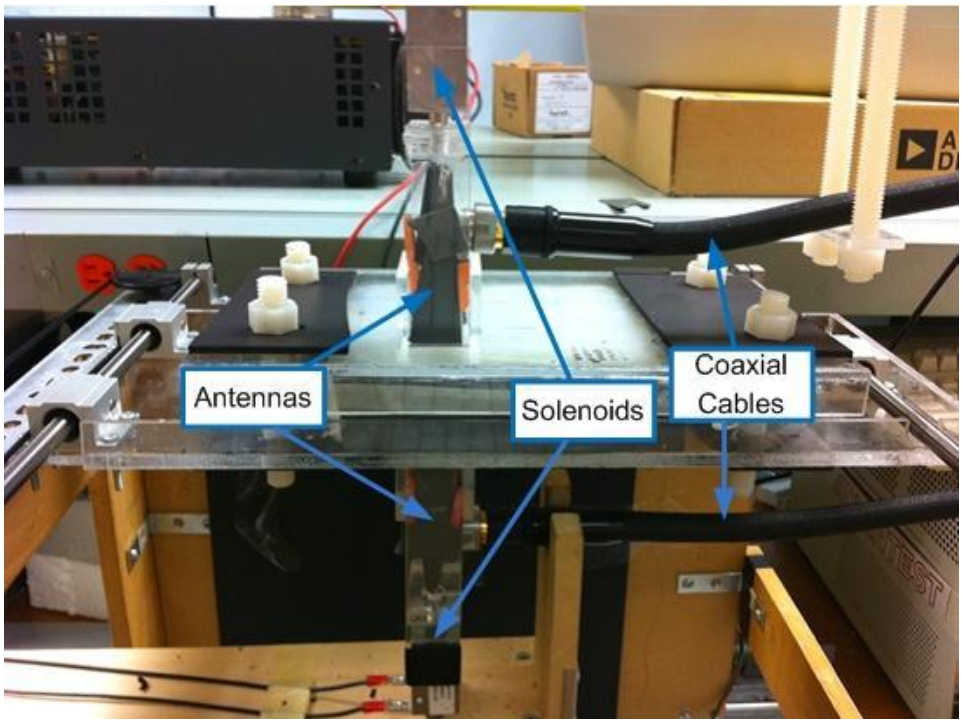

Fig. 2.9. Close view of the configuration of the two antennas.

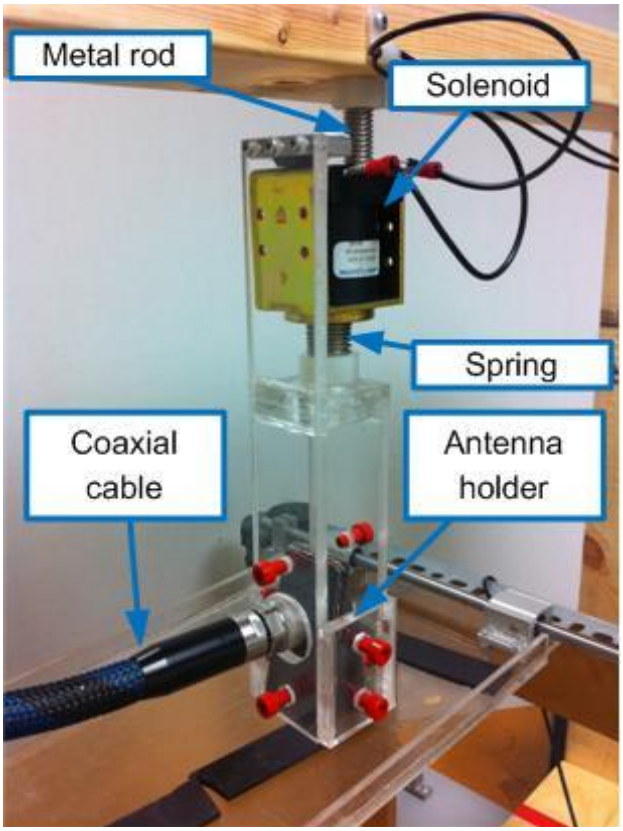

Fig. 2.10. Top antenna mount (antenna 1 shown).

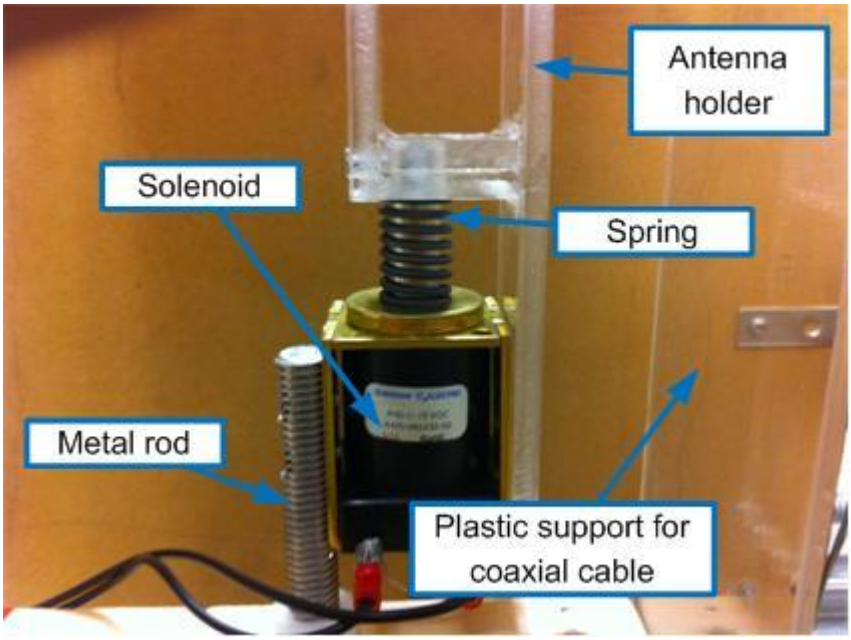

Fig. 2.11. Bottom antenna mount.

As Fig. 2.10 shows, the top antenna is mounted in a plexiglass antenna holder which is attached to the end of a solenoid. When the solenoid is off, the spring between the antenna holder and solenoid extends. The antenna is lowered and its aperture touches the plexiglass plate constraining the phantom. When the solenoid is on, the antenna is pulled up preventing any contact with the plate. Similar configuration is also implemented in the bottom antenna mount. When the solenoid is off, the antenna is pushed up by the spring, making good contact with the plexiglass plate. When the solenoid is on, the antenna is dragged down. This is shown in Fig. 2.11.

This solenoid mechanism is needed in the setup because when the phantom is moving, contact between the antenna and the plexiglass plate may cause excessive drag and wear of the hardware. Also, the friction between the plates and the antenna aperture may cause the antenna to tilt at an angle thus increasing the uncertainties of the measurement.

The plexiglass antenna holder is designed to hold two types of pyramidal horn antennas. Fig. 2.10 shows antenna 1 (side-feed antenna) fitted in the antenna holder. Fig. 2.12 shows antenna 2 (antenna with a rear feed) fitted in the antenna holder. In either case, at least 6 of the 8 red screws can touch the side of the antenna, holding it in place.

The dimensions of the antenna mount frame as well as the antenna holder are described in Appendix A.

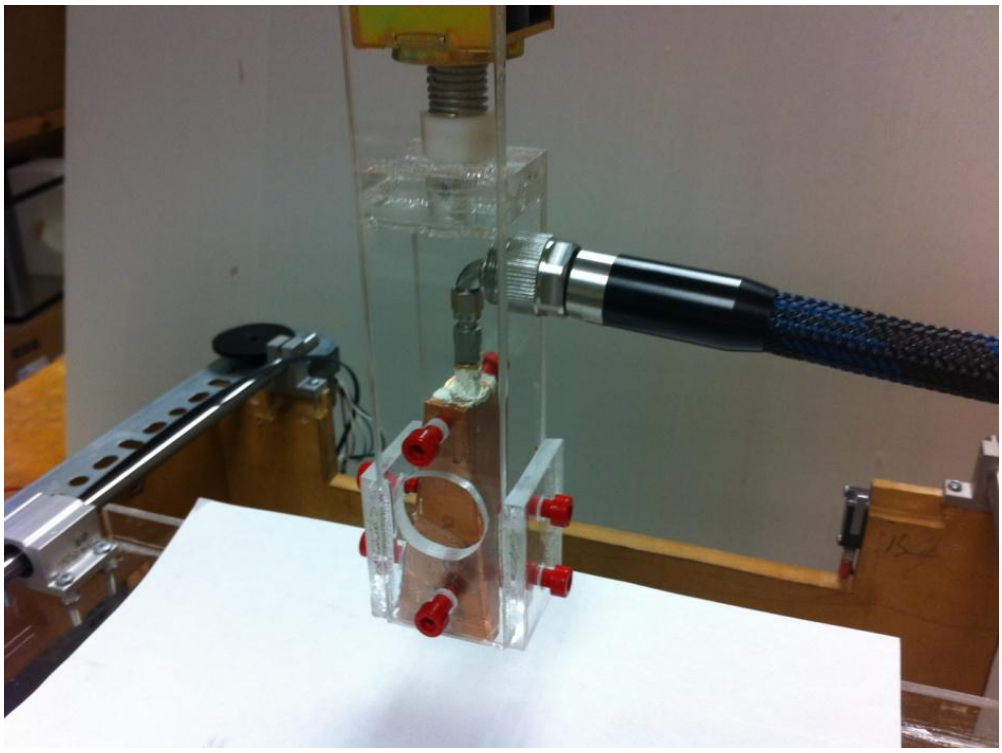

Fig. 2.12. Antenna 2 fitted in the top antenna holder.

2.3.2 Control and Power Circuits

Fig. 2.13 is more detailed block diagram of the raster-scanning setup. It shows the electrical connections in the system. The link between the PC and the Control Box is a parallel cable. The link between the GPIB (general purpose interface bus) card and the VNA is a GPIB cable. The links between the VNA and the antennas are coaxial cables. The black dash arrow means power cord. The solid-line arrows mean regular wire connections. The arrow direction in Fig. 2.13 represents the direction of the signal flow. Bi-directional arrows, like the parallel port line, mean that the PC can both write and read from the parallel port. Unidirectional lines, like the GPIB line, mean that the PC only writes to the GPIB bus.

While the coaxial cable, the parallel cable and the GPIB cable are simple connections, the connections for the components enclosed by the red dash closed-loop line are much more complicated. The detailed circuitry of these parts is shown in Fig. 2.14. The connections of each component are shown in detail in the close-ups shown in Figs. 2.15 to 2.20.

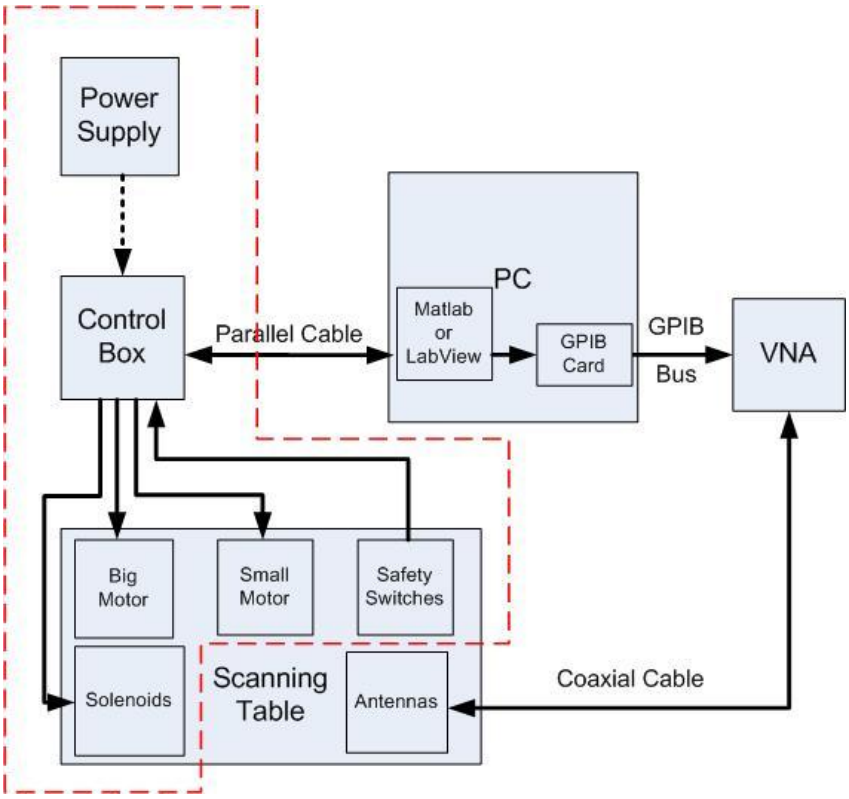

Fig. 2.13. Block diagram showing the electrical connections of the raster-scanning system.

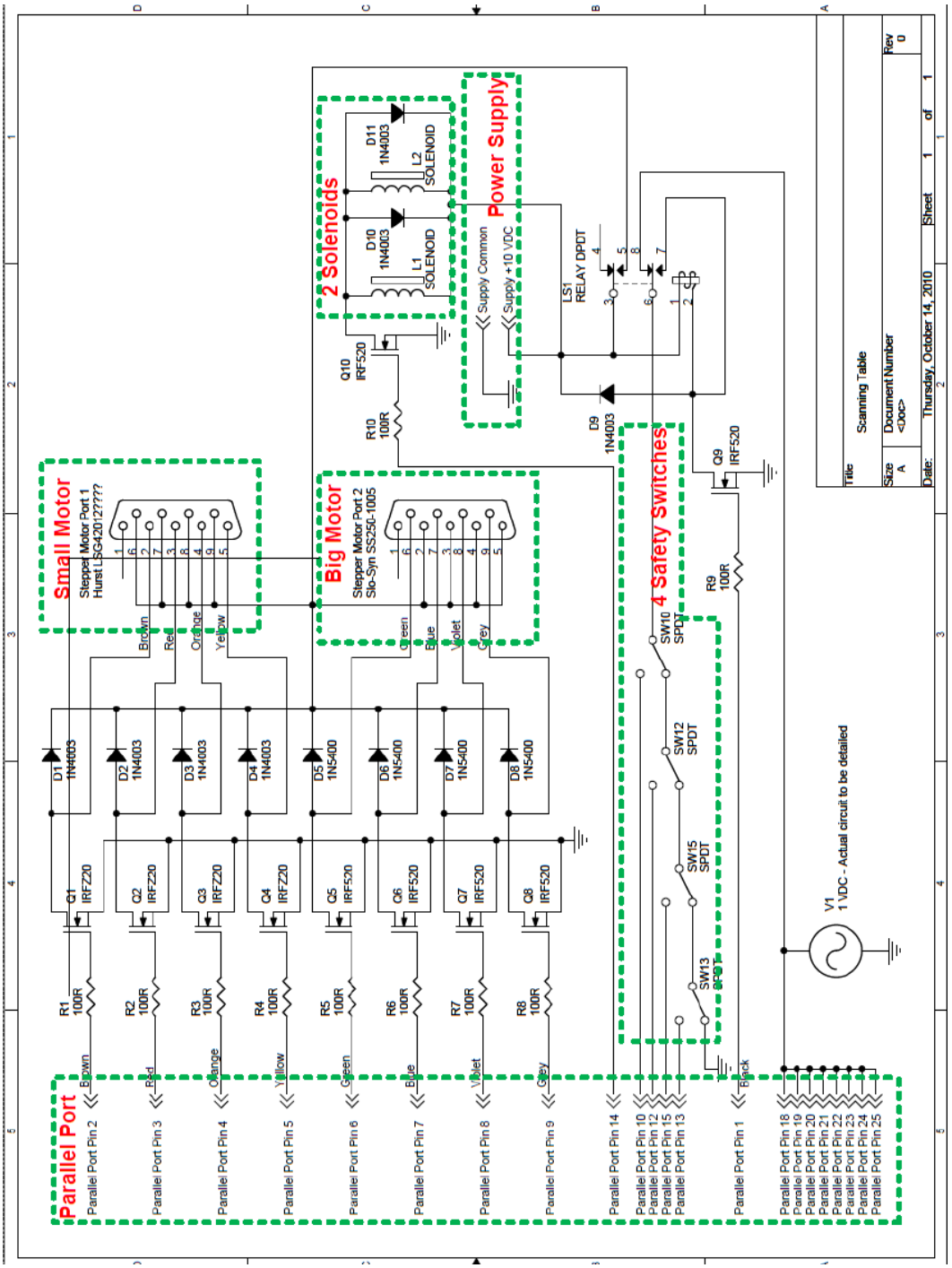

Fig. 2.14. Schematic for the parts enclosed by the red-dash close-loop line in Fig. 2.13.

Each of the blocks enclosed by the green dash lines represents a component specified in the title. The remaining parts are all enclosed in the Control Box. The Control Box contains mainly a MOSFET switching circuit for the step motor control, a power MOSFET, and a relay for power control.

Fig. 2.15 shows the external view of the Control Box. Fig. 2.16 shows the inner view of the Control Box.

Fig. 2.17 and Fig. 2.18 show the connections for the step motors. For easy reference, each wire has been tagged with the corresponding color according to the schematic in Fig. 2.14.

Fig. 2.19 shows the connection of the bottom solenoid. Fig. 2.20 shows the connections for one of the safety switches.

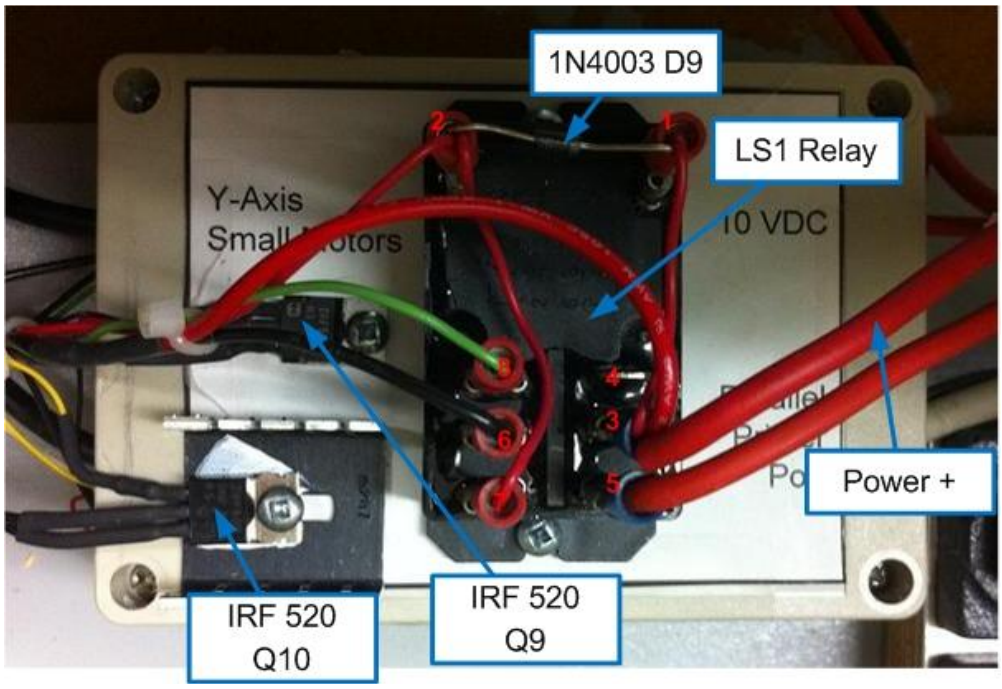

Fig. 2.15. Close-up of the Control Box.

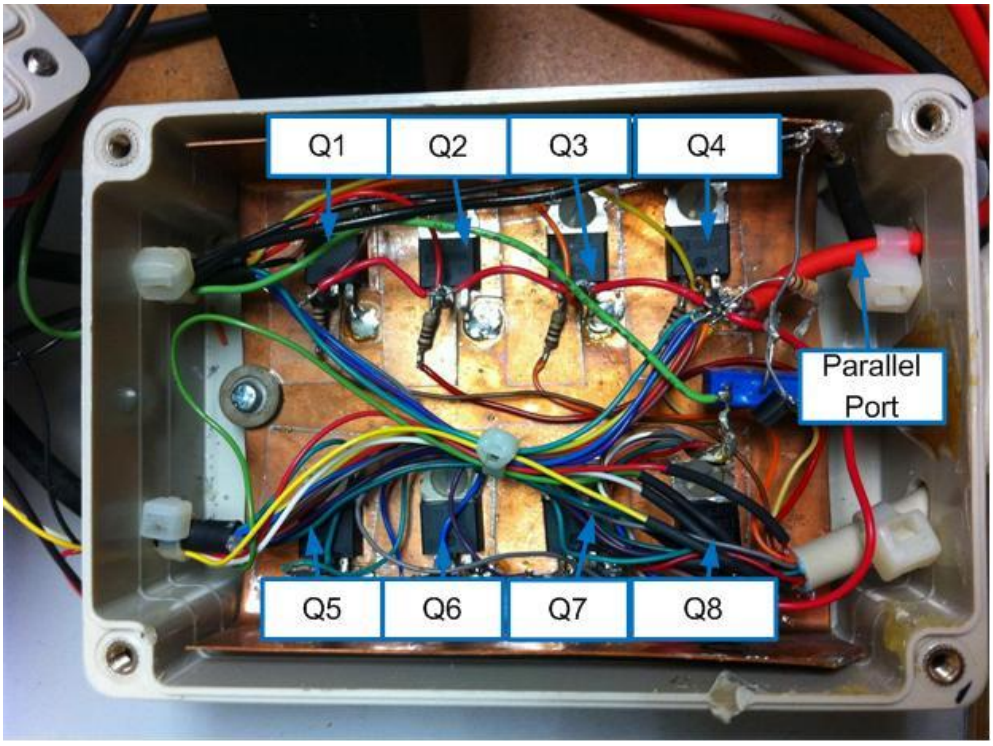

Fig. 2.16. Inner view of the Control Box.

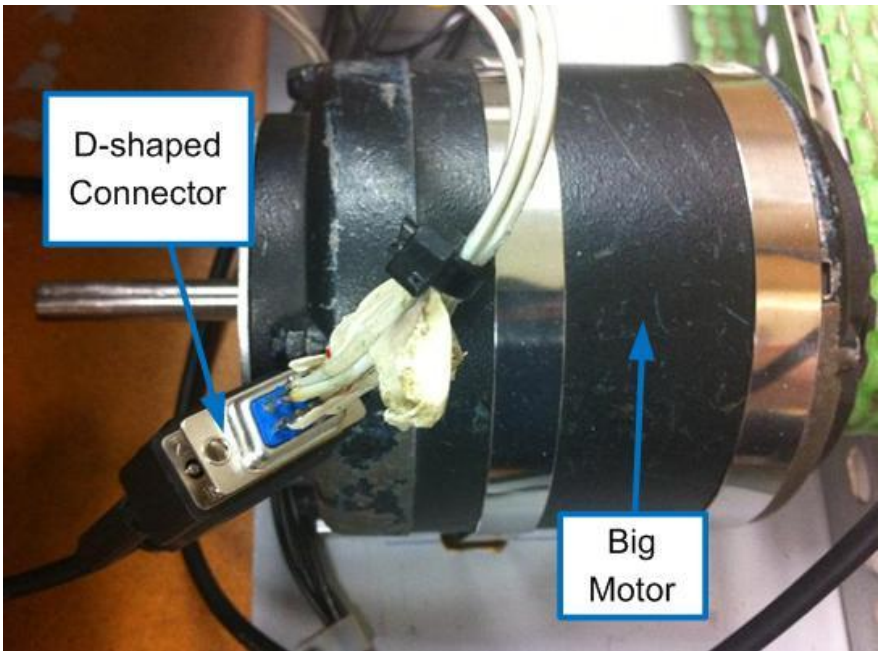

Fig. 2.17. Connections of the big motor.

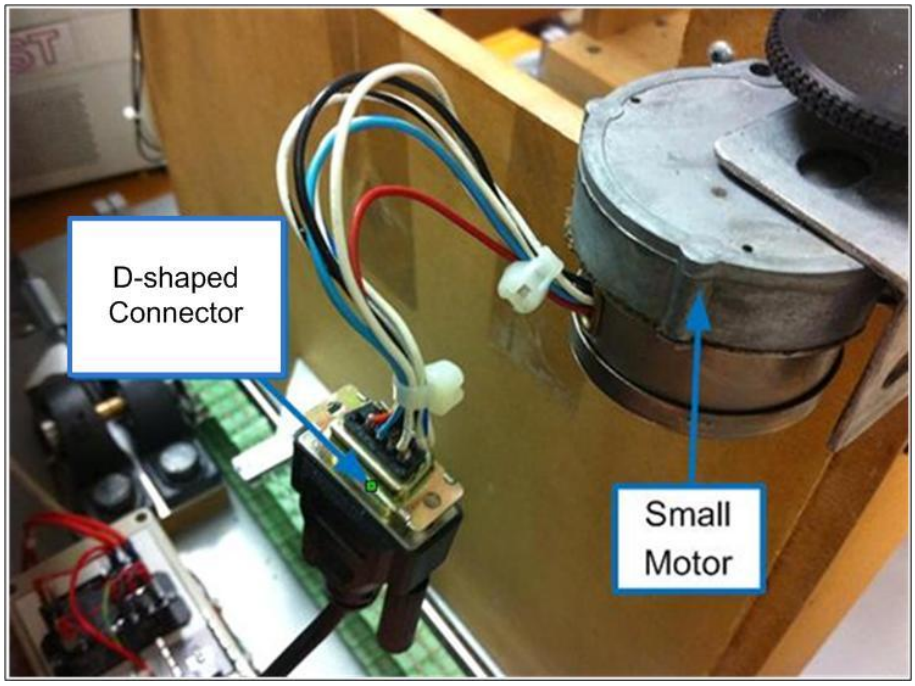

Fig. 2.18. Connections of the small motor.

Fig. 2.19. Connections of the bottom solenoid.

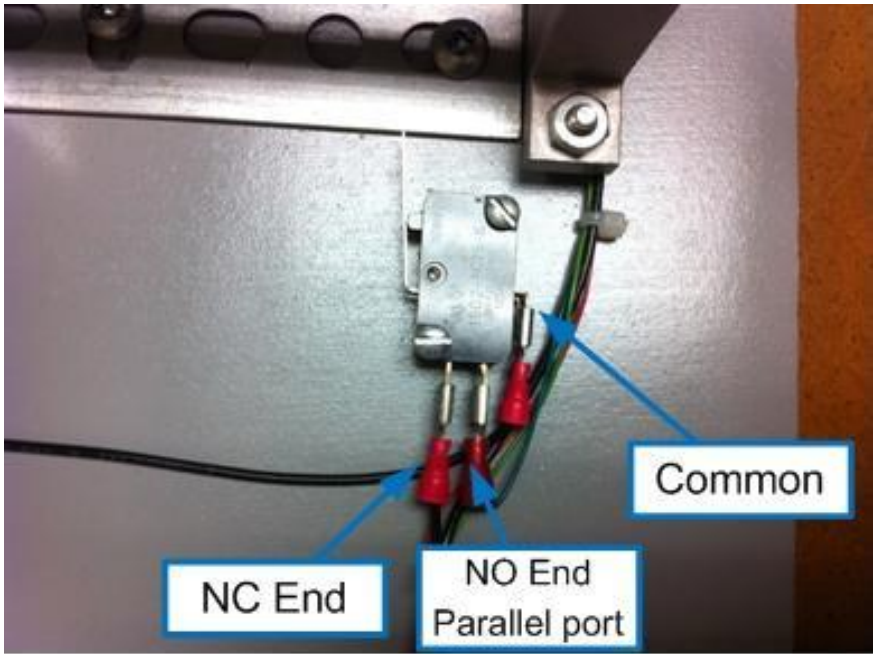

Fig. 2.20. Connections of one of the safety switches.

2.3.3 Fail-safe Circuit

Because the system involves step motors, solenoids and relays, safety measures are taken to ensure that the scanning system is fail-safe.

The safety features of the system involve 2 major parts. First, there are diodes used to discharge the solenoids (see Fig. 2.19). These diodes ensure quick discharge of the current in the solenoid when it is off.

Second, there are 4 safety switches installed at the end of the 4 directions in which the scanner can move. This is shown in Fig. 2.21. Switches 1 and 2 are installed directly on the base board. These switches are triggered when the scanner moves too far either left or right. Switches 3 and 4 are installed on the scanner's moving frame. They are triggered when the plates of the phantom holder move too far up or down.

Fig. 2.22 shows the close-up of the switch at the right end of the scanner. When the scanner moves too far to the right, the scanning table frame hits the trigger of the switch which shuts down the power to the step. The same mechanism is used for switches 3 and 4. Switch 3 is shown in Fig. 2.23.

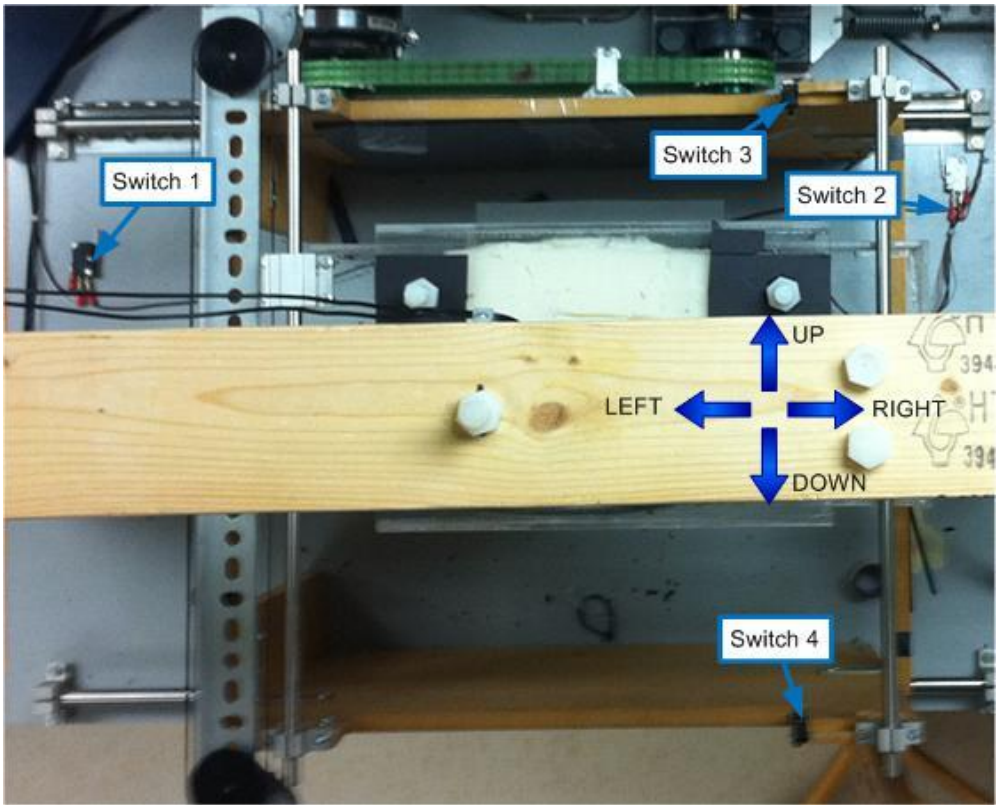

Fig. 2.21. Safety switches installed in the system. The photo shows a top view of the scanning setup.

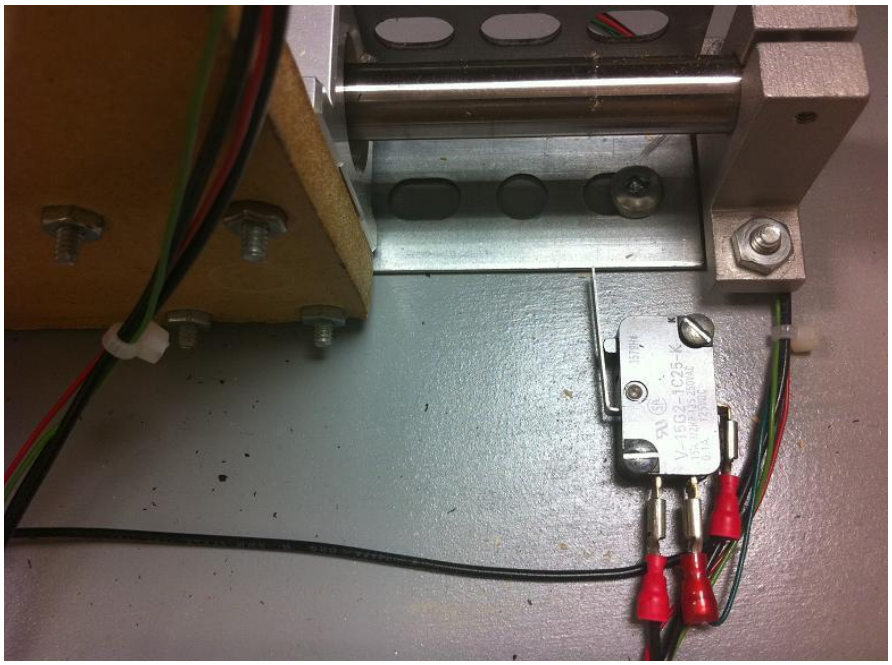

Fig. 2.22. Close-up of switch 2 at the right end of the scanner.

Fig. 2.23. Close-up of switch 3 at top of the scanning table frame.

As part of this safety feature, the electrical circuit is designed so that the scanner is able to recover from a failure caused by one or more switches being triggered. The details of this recovery process are discussed in section 2.4. Further details are provided in the operation manual in the Appendix B.

2.4 Software Implementation

Control is essential for a system of multiple components to work as a whole. This section covers the software design as well as the control algorithm of the software.

As Fig. 2.13 shows, the central control component of the system is a computer loaded with control software (Matlab [2] or LabView [3]) as well as a GPIB card. Both Matlab and LabView control scripts are implemented (the LabView script has not been finished at the time of writing this thesis). In this

chapter, we focus on the Matlab implementation. Note that for any Matlab script, there is a LabView version developed, or is being under development.

A customized Matlab script is written to integrate the scanner and the VNA. The script contains two major parts. One part is the script used to control the scanning table (step motors and solenoids) through the parallel cable. The other part is used to control the VNA through the GPIB bus. The control bus and software control algorithm are described in the following sections.

2.4.1 Control Bus

The parallel bus used in this system is with the standard 25-pin D-shaped connector. The pin assignment of the port is shown in Fig. 2.24.

The red highlighted pins (pins assignment started with letter C) are the control registers. They provide bidirectional signal communication (in/out). The yellow highlighted pins (pins assignment started with letter D) are the data registers. They also provide bidirectional communication. The blue highlighted pins (pins assignment started with letter S) are status registers, which only "read" the signal from the port. The rest (green highlighted) are grounds/common.

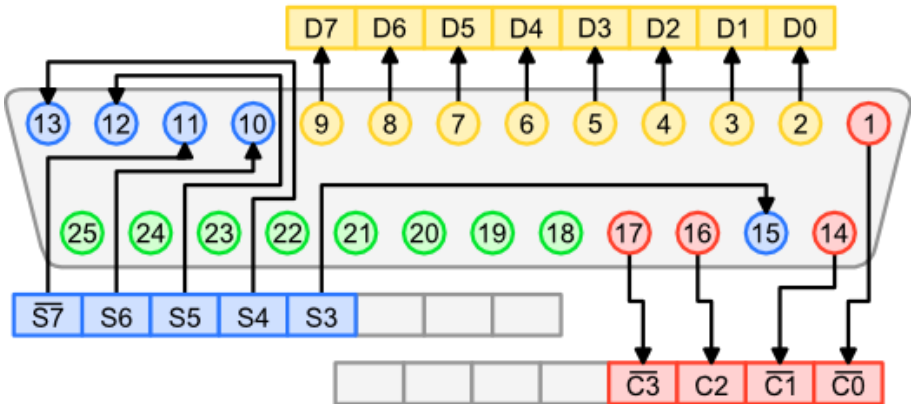

Fig. 2.24. Pin layout for a standard 25-pin parallel port (from [4]).

In the software, pins 1 and 14 from the control registers are used. Pin 1 is used for the recovery process when the safety switches are triggered. When pin 1 is enabled, an alternative current path is formed for the step motors to operate. Pin 14 is used to operate the solenoids.

The status pins are used to read the status of the emergency switches. Since there are 5 pins and only 4 switches, there is a pin that is not used. The mapping for the status pin and the switches is shown in the Table 2.1.

Table 2.1
Pin assignment for the status registers

Pin Number	**Assignment**	**Wire Color**
10	Left End	white
12	Right End	solid dark green
15	Up End	green with white strips
13	Down End	red with white strips
11	Unused	

The data register pins are used to provide the motors with stepping sequences. Since each motor needs 4-bit stepping sequences and there are 8 bits of data buses available, the lower 4 bits from the data registers is used to drive the small motor. The upper 4 bits are used to drive the big motor.

The ground pins are soldered together to drain current and to make a closed circuit.

The GPIB, or general purpose interface bus, is an interface designed for communication between electrical devices. It can be viewed as a special type of parallel bus, consisting of 8-bit data bus, 3-bit handshake interface, 5-bit bus

management interface and 8 ground lines. The GPIB standard, or IEEE 488.2-1987 standard, is widely adopted by hardware manufacturers. In addition, many commercially available or free software suites exist for easy control of different devices through the GPIB bus. For this project, instrument control toolbox, which is an add-on to the Matlab software, is used since the script used to control the parallel bus is also written in Matlab. Also, an Agilent E2078A/82350A GPIB card is installed in the computer to make connections between the VNA and the computer.

According to the definition of the GPIB device functions, the model adopted in this application is one talker and one listener. The computer where the Matlab scripts run is the talker. It sends out messages to the GPIB bus. At the other end, a VNA is the listener. It receives the messages through the bus and performs specific tasks. While there are many common interface messages for the GPIB interface, devices from different hardware vendors may have different commands. The lists of GPIB commands are usually included in the operation manual of the device. In the setup that we are currently working on, an Advantest VNA R3770 is used. Thus, the script is written according to its operation manual. It is possible that some of the commands need to be altered if a different VNA is used.

To make the operation of the system more user-friendly, a GUI (graphic user interface) is generated using Matlab GUI guide. The interface is shown in Fig. 2.25.

Fig. 2.25. Control interface of the scanning setup.

For the description of the above GUI and the operating procedure, please refer to Appendix B.

2.4.2 Software Control Algorithm

The algorithms behind the software which controls the system are discussed here. There are mainly 3 "functions" for the system to perform: initial positioning of the scanner; 1-D/2-D scan and recovery from failure caused by triggering the safety switches.

First, the basic mechanism to enable and disable the step motors is described. As shown in Fig. 2.14, the upper left parallel pins 2 to 9 are used to drive the stepping motor through two D-type 10-pin connectors. Close-ups for the

connections are shown in Fig. 2.17 and Fig. 2.18. They are responsible for the stepping sequences for each step motor. In the middle section of Fig. 2.14, the 4 safety switches are connected in series. Pins 10, 12, 13 and 15 are connected to the normally open terminal of each safety switch. In this way, whenever a switch is triggered, its status can be accessed through one of the status pins. Again in Fig. 2.14, the relay LS1 in the middle right section serves as a latch which is used to enable and disable the step motors. Its operation mechanism is described below.

1. When the circuit is in its initial state, contacts (3, 6) of the relay touch contacts 4 and 8, respectively; thus there is no power applied to the terminals of the step motors.
2. To enable the circuit, Q9 MOSFET is turned on by parallel port pin 1 for a short period of time (controlled by software), causing a closed loop for the solenoid. The metal contacts 3 and 6 of the relay are attracted down to touch contacts 5 and 7, respectively.
3. Q9 is off shortly after step 2 since signal from pin 1 is off, but contact 6 touching contact 7 creates a new closed loop for the solenoid. The current path now goes to ground through the four switches in series. In this state, there is power available across the step motors. Sending stepping sequences through pins 2 to 9 makes the motors turn.
4. In the event that the scanner hits one of the four safety switches, the current loop for the solenoid is interrupted. Thus, contact 3 detaches from contact 5, which effectively cuts the power from the step motors. And the

status pin connected to the switch is pulled down to ground, which is registered by the software.

5. To bring the system on again, the software first checks the status of the switches and determines in which direction the scanner should move in order to release the pressed switch. Then, it enables the Q9 MOSFET through pin 1 and moves the scanner away from the pressed switch. After the software sees that all switches are closed, it drops the signal from pin 1 and the system is restored.

Step 5 above is the recovery process when the system encounters failure due to any of the 4 safety switches being turned on. The process is illustrated in Fig. 2.26. in a flow chart form.

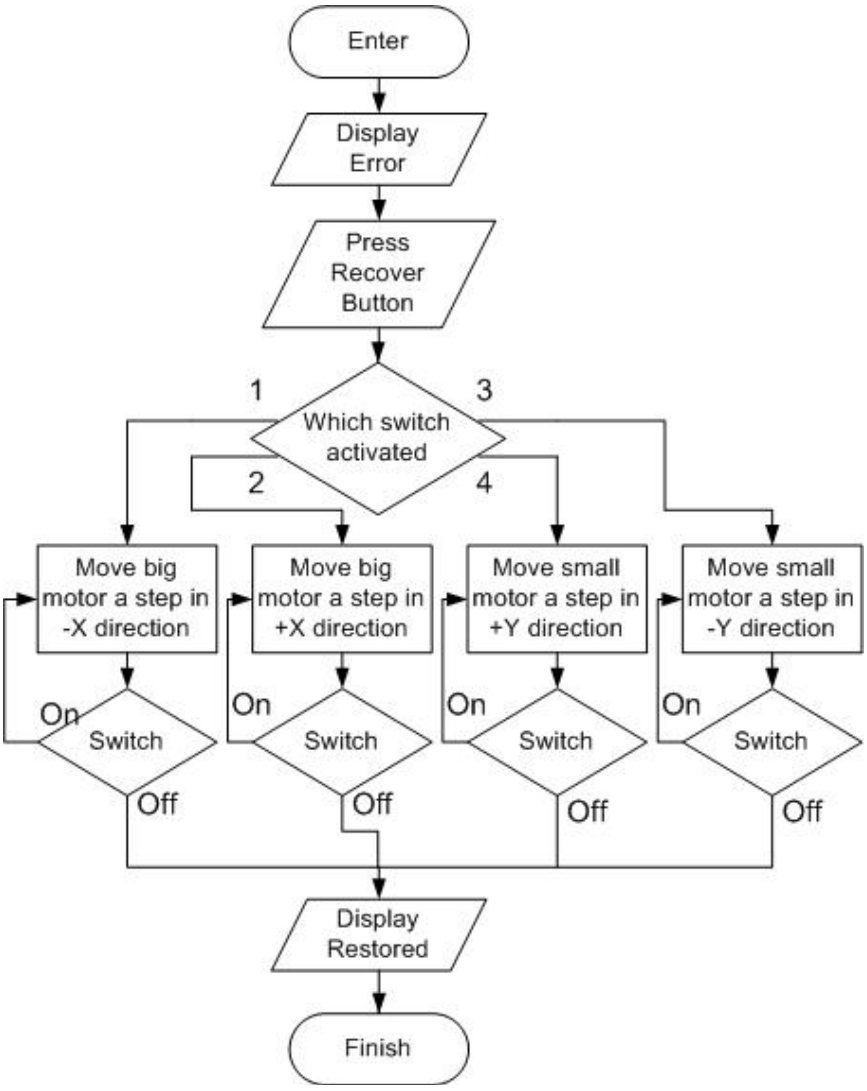

Fig. 2.26. Flow chart for system recovery from failure caused by triggering a safety switch.

The flow chart describing the scanning table initial positioning is shown in Fig. 2.27. When the scanner initial positioning is performed, the software first checks the user input data, which specifies the direction and distance of moving. Then, it runs through a stepping loop until the target position is reached. However, it is possible that users could make a mistake and put a value too big for the scanner to travel. In this case, the scanner triggers one of the safety switches and the step motors are cut from power. A system recovery procedure (exceptions routine) is then needed to bring up the system again. Please note that the exceptions routine in Fig. 2.27 is identical to the process described in Fig. 2.26.

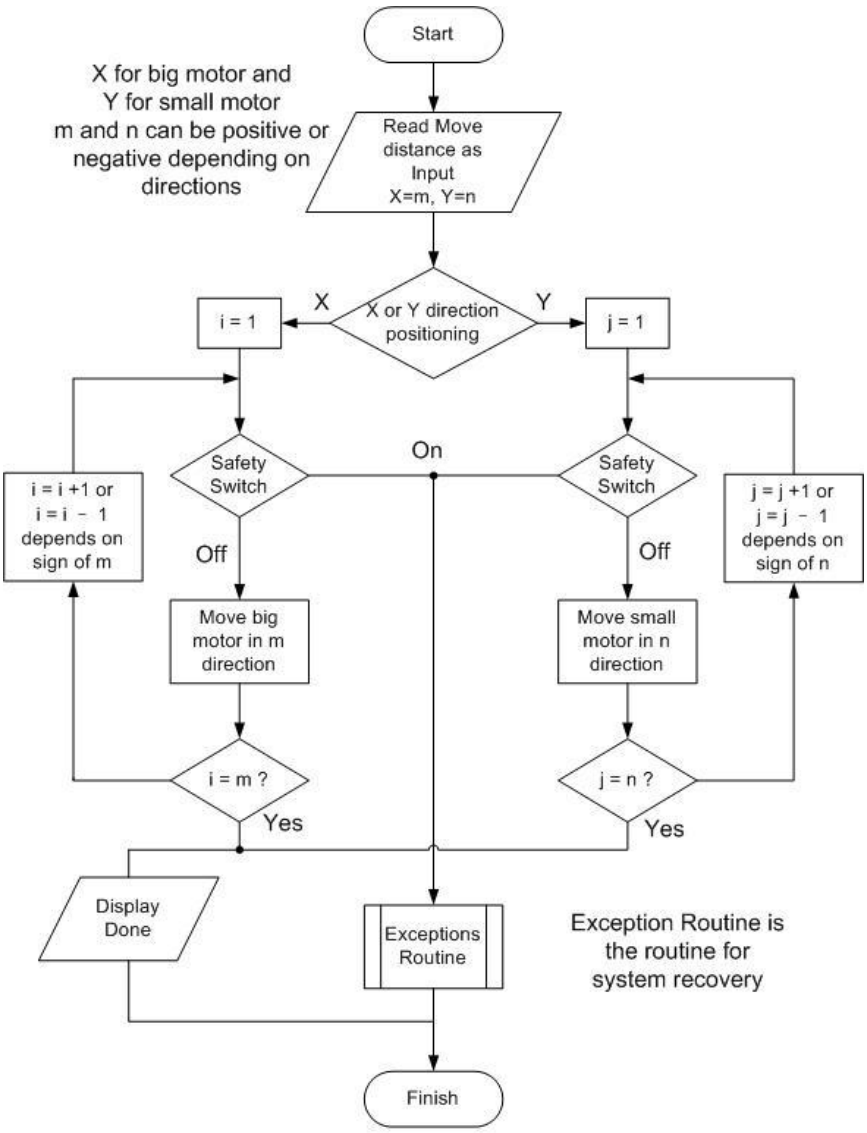

Fig. 2.27. Flow chart for scanner initial positioning.

The flow chart describing the 1-D/2-D scan procedure is shown in Fig. 2.28. Upon request by the user for a 1-D/2-D scan, the software first determines whether it is a 1-D scan or a 2-D scan. For 1-D scan, it then determines if it is an X direction or a Y direction scan (1-D scan is available only in positive directions) and the scan distances "m" or "n" (m for X direction and n for Y direction). Then the software performs a double-nested loop and takes VNA measurements with spatial sampling rate "a" or "b" (a for X direction and b for Y direction). Upon exceptions (safety switches triggered), the system goes into exception subroutine which is the system recovery routine described in Fig. 2.26.

For a 2-D scan, the software performs a raster scan by entering a triple nested loop. The scanner first moves in the +X direction, taking measurements according to the spatial sampling rate specified as "a". When the scanner reaches the distance denoted by "m", it then moves in the +Y direction for a distance specified by spatial sampling rate "b". After that, the scanner reverses direction and moves in the –X direction, etc. The procedure for the raster scan is illustrated in more detail in the operating manual which is in Appendix B. If the safety switches are triggered, the software enters exception subroutine and performs system recovery process as described before.

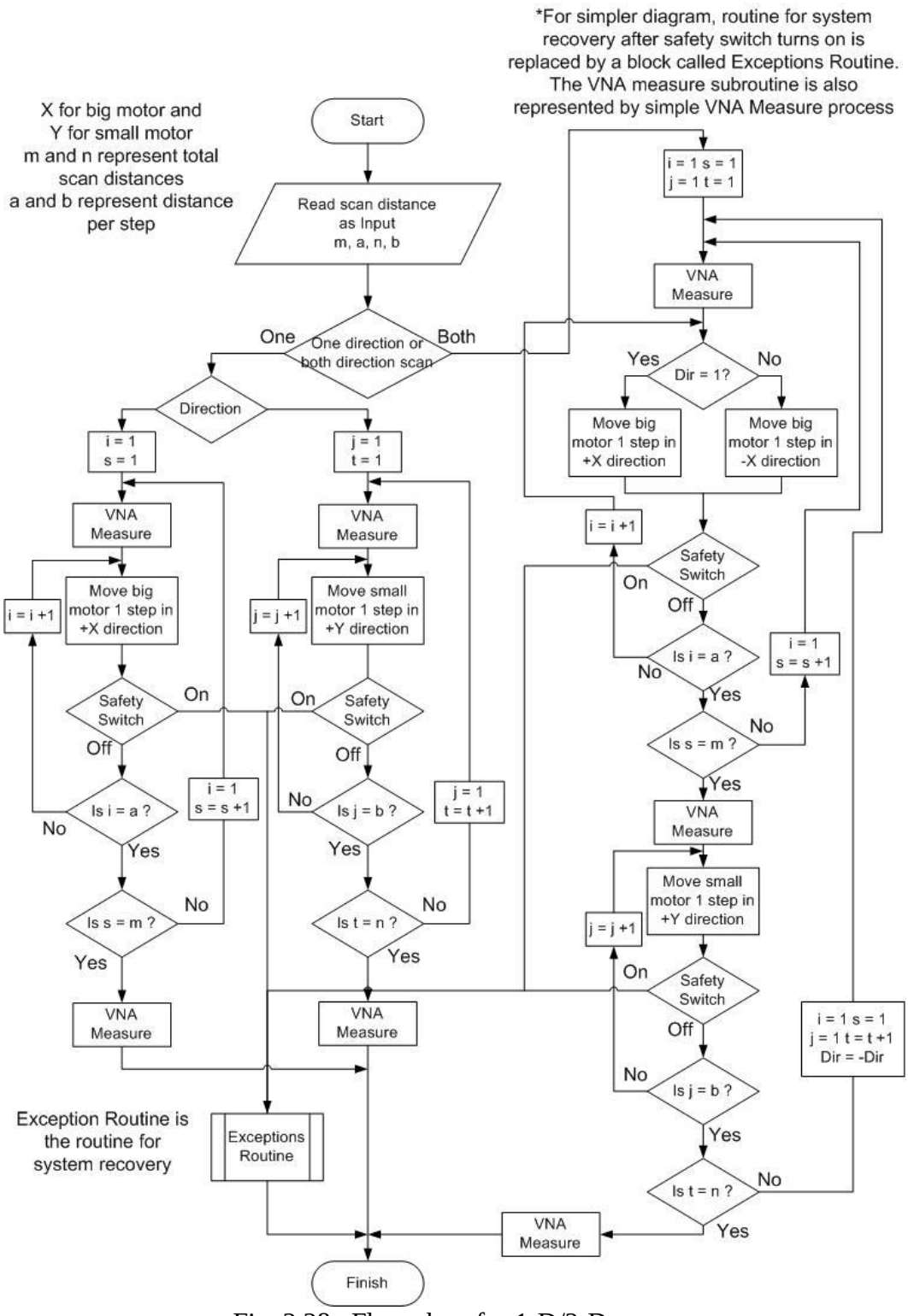

Fig. 2.28. Flow chart for 1-D/2-D scan.

2.5 Improvements and Recommendations

Many improvements have been made to the raster-scanning system since first built. With the current step motors, the moving/scanning speed is fixed. With proper VNA settings, a fast 2-D scan can be achieved. Thus, most of the efforts focus on how to make the system "quieter" than it is now. One example for such improvement is mentioned in section 2.4.1. The rods on which the solenoids and the antennas are mounted are used to be made of plastic. However, in a typical measurement, it is observed that the plastic rod shakes a lot. Thus, the accuracy of the antenna position can be affected. Metal rods were used to replace the plastic rods, which reduced the shaking substantially. Another example is the change of the solenoid and the spring. In the original design, two weak solenoids and springs were installed. During measurement, it was observed that occasionally the weak solenoid could not pull the antennas far enough from the plexiglass plate of the phantom holder. Thus the antenna was "dragged" across the plexiglass plate, causing its tilting. Later, stronger solenoids and springs are used to solve this problem.

In current measurements, the thickest phantom is 5 mm. But for more realistic and practical scenarios, the phantom thickness should be larger which in turn will reduce the signal level significantly, especially in the high-frequency end. Thus, it is crucial to make the system quieter, which means lower noise level. For further improvements of the system, a comprehensive study of the uncertainty level of the system is needed and this is discussed in Chapter 3.

References

[1] J.-C. Bolomey and C. Pichot, "Microwave tomography: From theory to practical imaging systems," *Int. Journal of Imaging Systems and Technology*, vol. 2, pp. 144–156, 1990.

[2] MATLAB 2010, The MathWorks Inc., 3 Apple Hill Drive, Natick, MA, 2010. [Online]. http://www.mathworks.com/.

[3] LabView ver. 8.5, National Instruments Corporation, 11500 N MoPac Expressway Austin, TX 78759-3504 USA, 2011. [Online] http://www.ni.com.

[4] EEWeb Electrical Engineering Community. *25-pin Parallel Port pin Assignments* [Online] http://www.circuit-projects.com/control-circuits/parallel-port-used-to-control-peripheral-electronics.html

CHAPTER 3

DYNAMIC RANGE OF THE RASTER-SCANNING SYSTEM

Introduction

As any measurement system, the planar raster-scanning system is limited by certain accuracy level which is a result of multiple factors. This accuracy level is defined as the dynamic range of the system which represents the strongest and weakest signals that can be picked up in the measurements. In our system, we are measuring reflection and transmission coefficients (*S*-parameters) over a lossy

phantom, which is always a negative value in dB units (or below 1 as a ratio). Thus, the dynamic range of the system is limited only by the lower bound, the weakest signal. To claim that the developed system can produce accurate and reliable measurement data, a comprehensive study on the dynamic range of the system is needed. This is also an essential step in finding the limitation factors and improving the performance of the system.

3.1. Types of Uncertainties in the System

The types of uncertainties in the planar raster-scanning system can be broke down into two categories, internal uncertainties and external uncertainties. Internal uncertainties are intrinsic to the measuring instruments. An example is the dynamic range of the VNA, which is an intrinsic property of which we have limited control. Also, the antennas (or the microwave sensors) are a source of internal uncertainties. External uncertainties on the other hand include: uncertainties introduced by the positioning mechanism of the scanning table, uncertainties introduced by external wire connections, uncertainties introduced by additional active components (amplifiers, etc.). In most cases, we have control over the factors which affect external uncertainties. Thus, by studying the effects of each factor, we can learn how to reduce the uncertainty level, which in turn will lead to higher dynamic range of the scanning system.

3.2. Noise Floor of the VNA

This section demonstrates the study of the intrinsic dynamic range of the VNA (Advantest R3770). It also exploits the possibility to improve the performance by using low-noise-amplifier (LNA).

3.2.1. Intrinsic Noise Associated with the VNA

The intrinsic noise floor of the VNA defines the weakest signal that can be measured by the VNA. Three sets of scenarios are measured.

1) Port 1 and port 2 are matched with 50 ohm loads.
2) Port 1 is matched with a 50 ohm load and port 2 is open.
3) Port 1 is matched with a 50 ohm load, port 2 is connected with antenna sensors as follows:
    a. port 2 is connected to antenna set 1 directly;
    b. port 2 is connected to antenna set 2;
    c. port 2 is connected to antenna set 2 through a right angle RF adapter.

The settings of the VNA are shown in the table below. These settings are optimized for real phantom measurements and they are applied to all measurements in this thesis unless otherwise specified.

Table 3.1. VNA settings for phantom measurements

Settings	**Value**
Frequency Range	3 GHz – 10 GHz
Power	8 dBm
Averaging Factor	16
Resolution Bandwidth (IF)	10 kHz
Frequency Sampling Points	201
Smoothing	10%

Fig. 3.1 shows the transmission coefficient S_{21} versus frequency in scenario 1. Both ports of the VNA are matched with 50 ohm loads. If both ports are ideally decoupled and isolated, S_{21} should be equal to 0. However, in practice, there is certain power leaking from port 1 into port 2. This is due to the internal coupling of the VNA and should be regarded as the limit between signal and noise. Also, note that there is a jump of noise level at around 8 GHz. According to the Advantest VNA manual [1], the VNA has 3 receivers across its operating frequency range. This jump represents the boundary between two receivers which is at 7.92 GHz. By fitting a step line (red line in bold), we find the dynamic range of the VNA to be 123 dB (i.e., 8 dBm - (-115) dB) from 3 GHz to 7 GHz, and 108 dB from 7 GHz to 10 GHz.

Fig. 3.2 shows S_{21} measured in scenario 2. Port 1 is matched and port 2 is open. Theoretically, since port 1 is matched, there is no power leaking from port 1. Port 2 is open, so it is possible to pick up environment noise as well as the

internally coupled signal shown in Fig. 3.1. In practice, the measured data is very similar to the graph obtained in the previous scenario and the same step line fitting for the dynamic range applies.

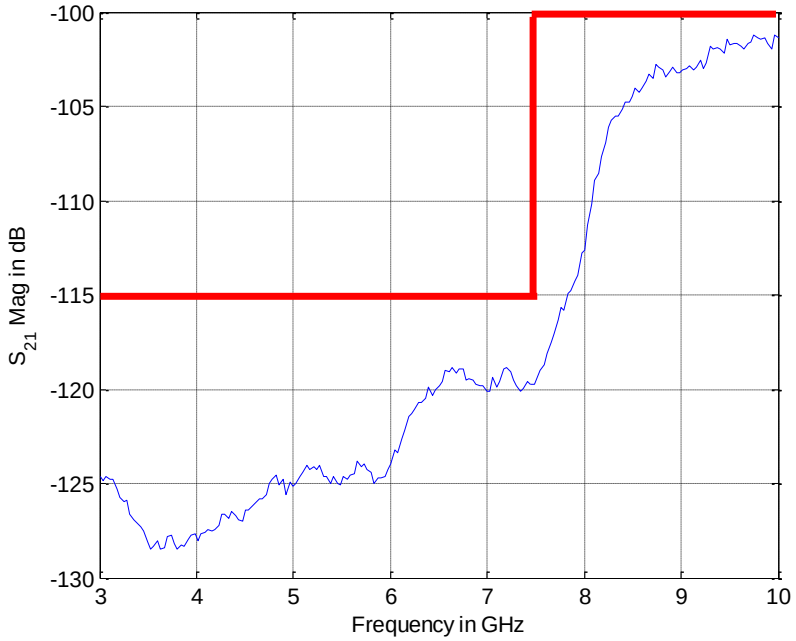

Fig. 3.1. S_{21} measured in scenario 1: ports 1 and 2 are matched with 50 ohm loads.

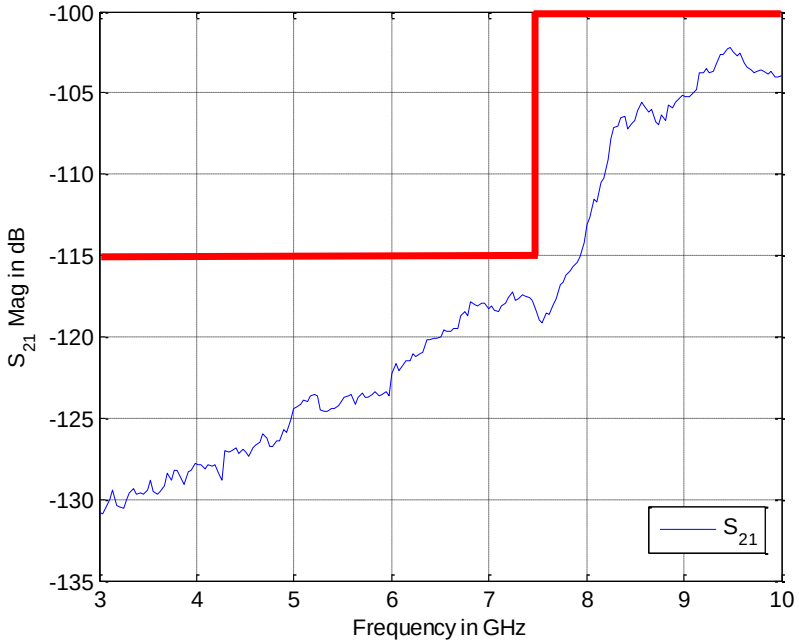

Fig. 3.2. S_{21} measured in scenario 2: port 1 is matched and port 2 is open.

In scenario 3, port 1 is matched and port 2 is connected to the antenna. This is similar to scenario 2 except that with an antenna attached to port 2, it is more likely to pick up leaking power (if any) from port 1. There are 3 sub-cases in scenario 3 since there are two different pyramidal horn antennas, namely antenna 1 and antenna 2, which are shown in Fig. 3.3. sub-cases (a) and (b) are measurements with antenna 1 or antenna 2 connected to port 2. Additionally, since the coaxial feed of antenna 2 is in the back, a right-angle adapter is needed when installing the antenna on the antenna holder. A third sub-case (c) is needed to verify the effect of this right angle adapter.

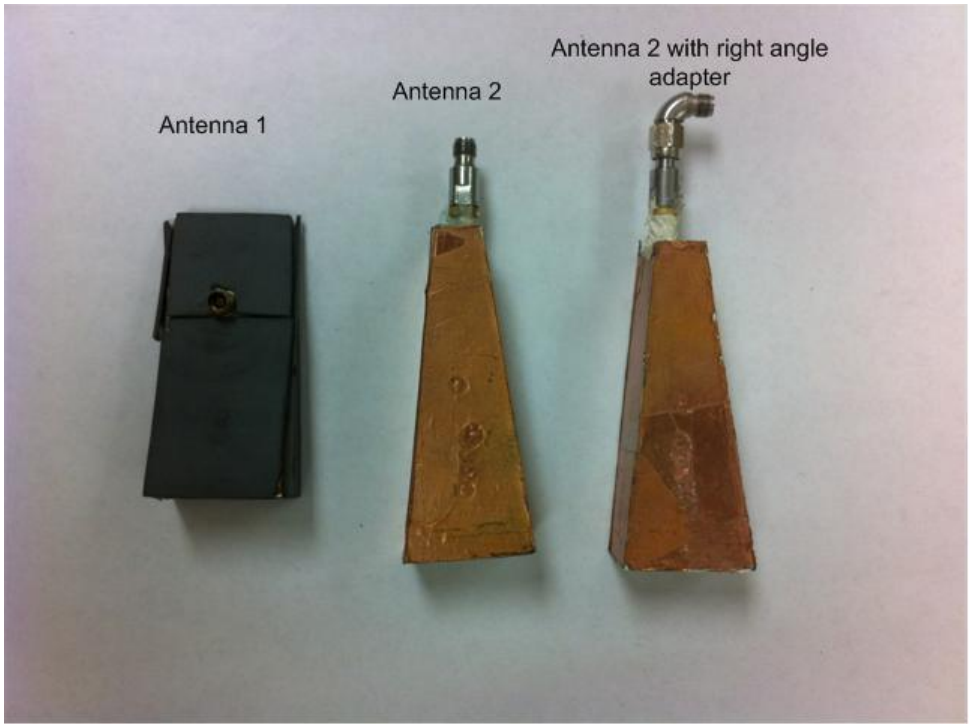

Fig. 3.3. Two pyramidal horn antennas and the right-angle adapter.

Fig. 3.4 shows the measurement results for all three cases. It is clear that the noise levels between 6 GHz and 8 GHz are higher as compared to the previous measurements resulting in a different fitting line. Thus, with the antennas connected to the VNA, the dynamic range of the "partial" system is 118 dB (i.e., 8 dBm - (-110) dB) from 3 GHz to 7 GHz and 108 dB from 7 GHz to 10 GHz.

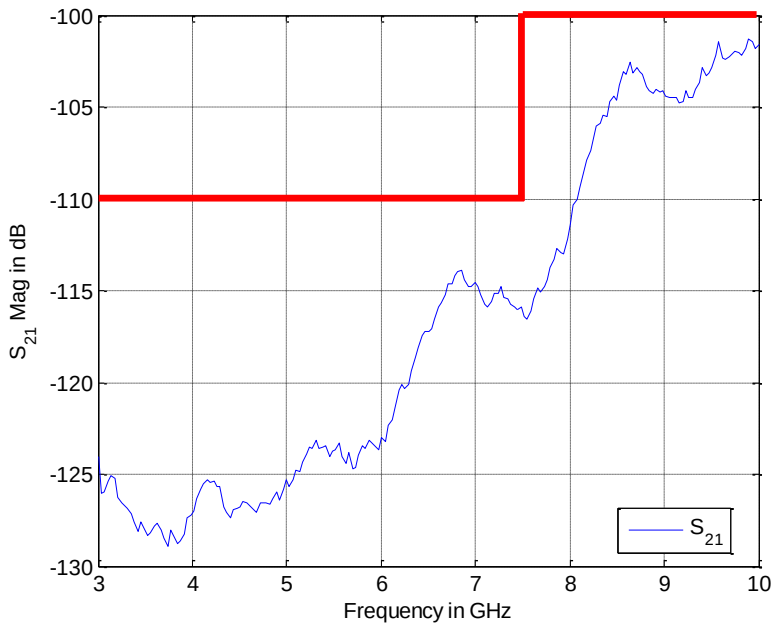

(a)

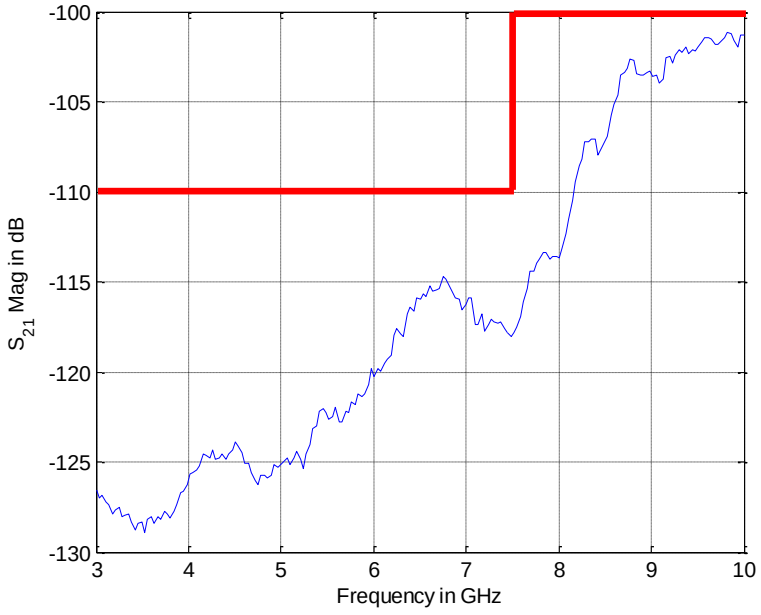

(b)

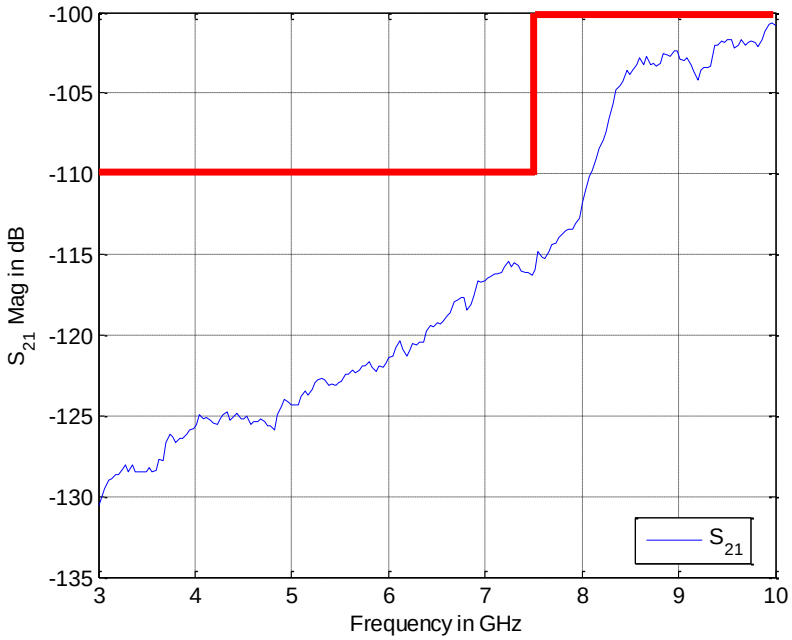

(c)

Fig. 3.4. S_{21} measured in scenario 3. Port 1 is matched. (a) Port 2 is connected with antenna 1. (b) Port 2 is connected with antenna 2. (c) Port 2 is connected to antenna 2 through a right-angle adapter.

3.2.2. The Effect of Using Low-noise Amplifier (LNA)

According to the noise formula for cascaded system:

$$T_{cas} = T_{e1} + \frac{T_{e2}}{G_1} + \frac{T_{e3}}{G_1 G_2} + \ldots, \tag{3.1}$$

the noise temperature of cascaded RF systems is dominated by the first-stage amplifier given it has a moderate gain and the latter stages do not present large noise figures [2] [3].

In (3.1), T_{cas} is the noise temperature of the cascaded system, T_n denotes the equivalent noise temperature of the n^{th} stage, and G_n denotes the gain in the n^{th} stage. Thus, theoretically, by cascading two LNAs to the receiving port (port 2), we should expect improvements in the dynamic range of the system [3] - [5]. To study this effect, the same three sets of measurements as in section 3.2.1 are performed and the results are shown below.

Fig. 3.5 shows the experimental setup. Port 1 of the VNA is matched with a 50 ohm load. The output of the two-stage cascaded LNA is connected to port 2 of the VNA while its input is loaded in the manner described in the beginning of sub-section 3.2.1. The specifications of each stage of the LNA are shown in Table 3.2.

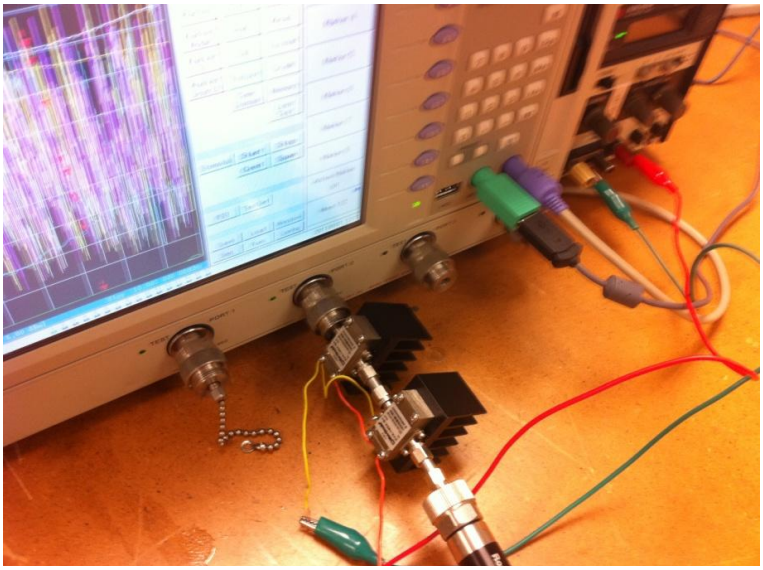

Fig. 3.5. Cascaded LNAs connected to port 2. Port 1 is matched.

Table 3.2. Specifications of the LNA ZVA-183+

Frequency (GHz)	0.7 to 18
Gain	26 dB
Maximum Output Power (1dB Compr.)	24 dBm
Noise Figure	3 dB

Fig. 3.6 shows the measured transmission coefficient when port 2 of the VNA is connected to the LNA output while the LNA input is loaded with a 50 ohm load. Despite the fact that the gain in this cascaded setup is 52 dB, the noise floor represented by the step fitting line only goes up by 35 dB as compared to the no-LNA measurement cases.

Fig. 3.7 shows the result when port 2 of the VNA is connected to the input of LNA and the LNA input is open. The result shows a higher noise floor from 5 GHz to 8.5 GHz.

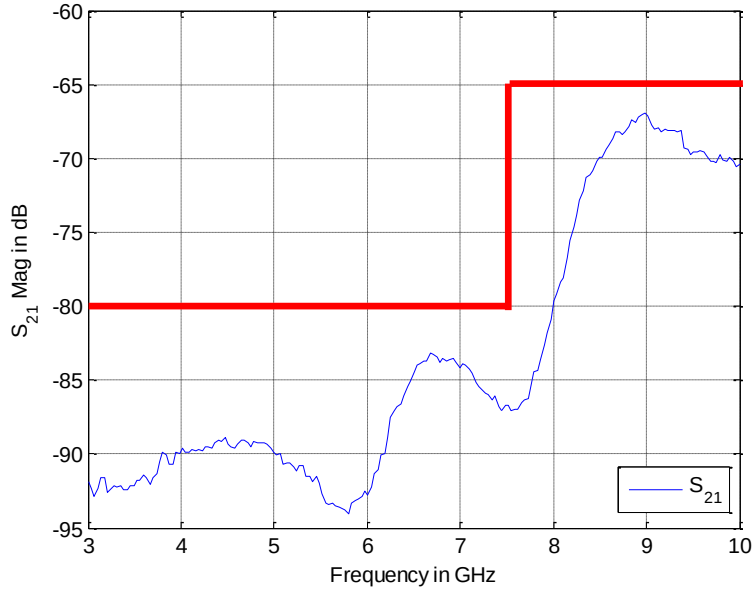

Fig. 3.6. S_{21} measured in scenario 1. Port 1 of the VNA is matched. Port 2 of the VNA is connected to the output of the LNA while the input of the LNA is loaded with a 50 ohm load.

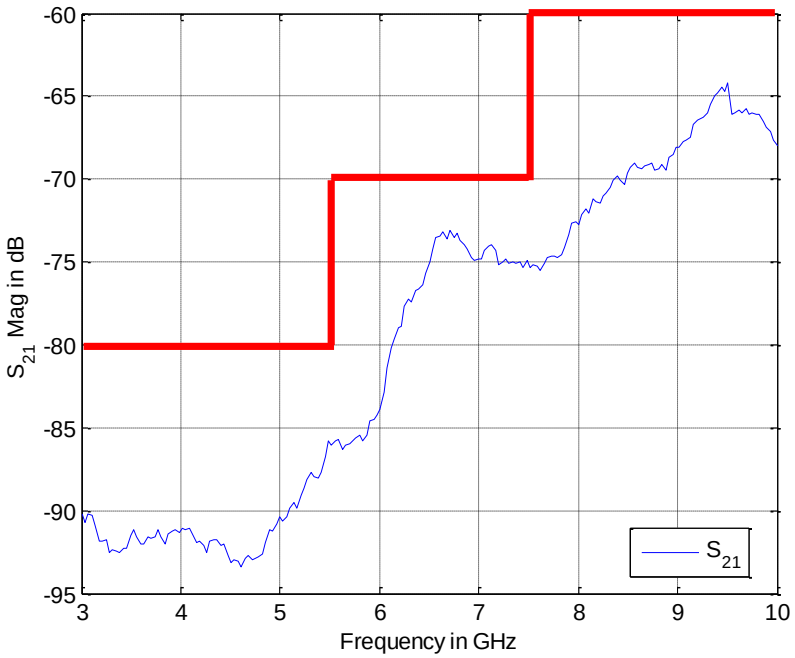

Fig. 3.7. S_{21} measured in scenario 1. Port 1 of the VNA is matched. Port 2 of the VNA is connected to the output of the LNA while the input of the LNA is left open.

Fig. 3.8 shows the 3 sub-cases when antennas are connected to the input of the LNA. Notably when antenna 2 is connected, the noise floor is higher. By choosing the worst case results (scenario 3, sub-case b and c), we can conclude that with the help of the two-stage LNA, the dynamic range of the system is 135 dB (i.e., 8 dBm - (-75) dB + 52 dB) from 3 GHz to 5.5 GHz and 123 dB (i.e., 8 dBm - (-63) dB + 52 dB) from 5.5 GHz to 10 GHz. Compared to the no-LNA case, the dynamic range obtained is improved by about 15 dB.

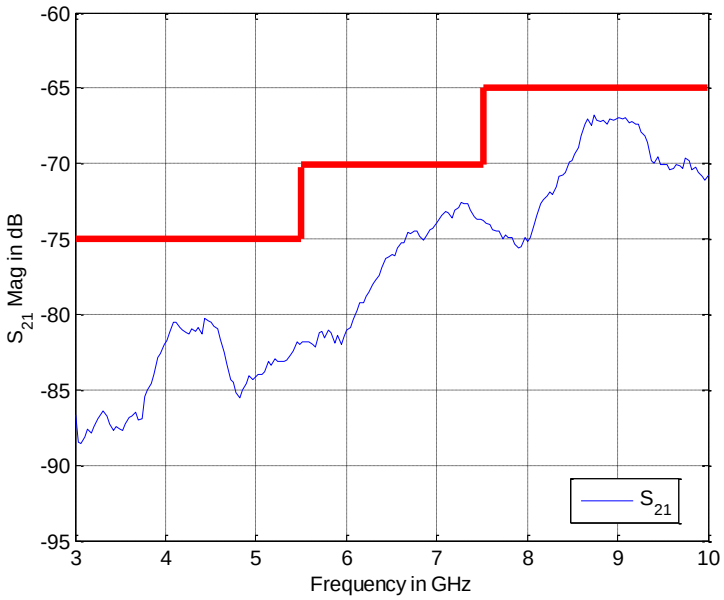

(a)

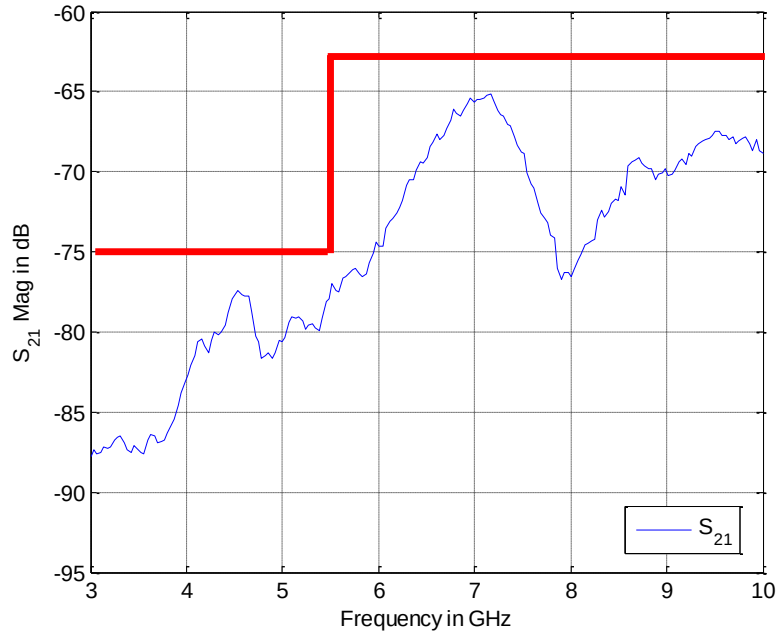

(b)

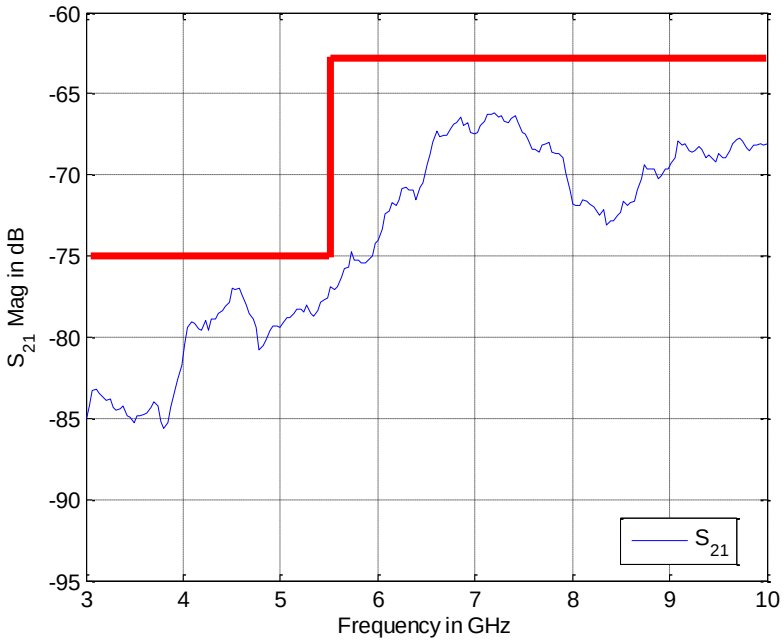

(c)

Fig. 3.8. S_{21} measured in scenario 3. Port 1 is matched. (a) Port 2 is connected with antenna 1 through the LNA. (b) Port 2 is connected with antenna 2 through the LNA. (c) Port 2 is connected to antenna 2 through the LNAs with a right-angle adapter.

3.3. Uncertainties Associated with Positioning

One of the key components of the raster-scanning system is its scanning setup. It includes a lateral scanning table driven by step motors and two vertical solenoids loaded with springs. Fig. 3.9 illustrates the positioning system. In our raster-scanning measurement setup, solenoids with springs move the antennas in the vertical direction and two step motors move the scanning table in the lateral direction. These motion are the source of external uncertainties. In this section, the uncertainties associated with the positioning mechanism are studied and measured in terms of a new measure, namely, the signal to uncertainty ratio (SUR).

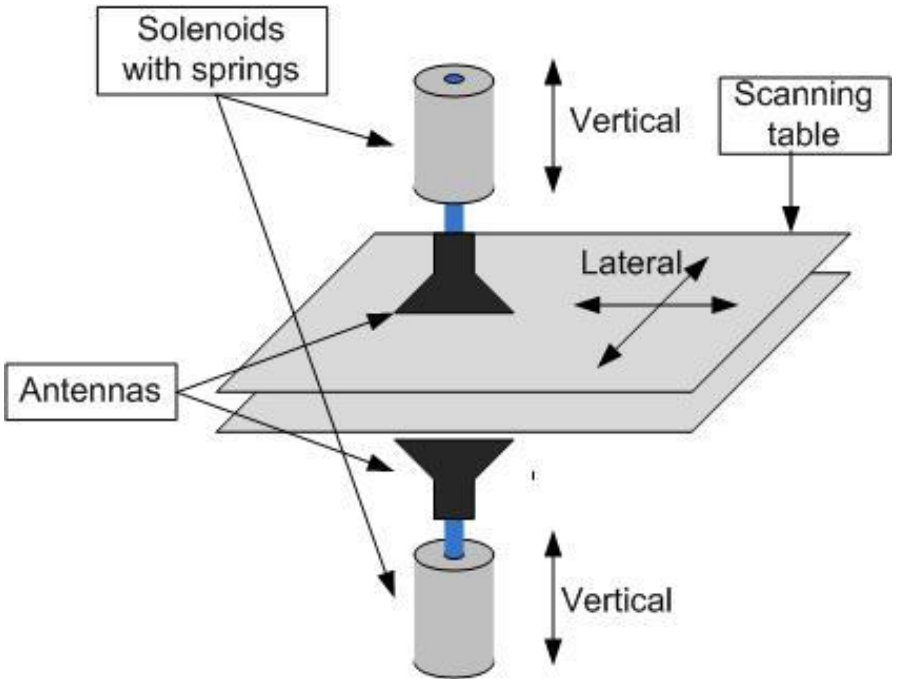

Fig. 3.9. Illustration of the positioning system.

3.3.1. Uncertainties Associated with Vertical Motion

The uncertainties introduced by the vertical motion of the antenna come from two factors. As illustrated in Fig. 3.10, the antenna may be slightly misaligned due to a rotation around the solenoid shaft. Also, the antenna may be tilted at an angle with respect to the scanned planar surface due to imperfect mounting in the antenna holder.

To quantitatively measure the uncertainties, a measurement scenario involving only the vertical motion of the scanning table is performed first. In this scenario, the two antennas are aligned along each other's boresight at the opposite sides of the phantom. When the solenoids are turned on, both antennas retract from the phantom. When the solenoids are off, the springs push the antennas to "snap" onto the plexiglass plates constraining the phantom. In this position, one VNA sweep (3 GHz to 10 GHz) is performed and the results (S_{21} magnitude and phase) are saved. Twenty of these measurements are taken, and the average signal level is calculated:

$$S_{21\_av\_signal} = \sum_{i=1}^{n} S_{21}^{i} \Big/ n \tag{3.2}$$

where n is the number of measurements (n = 20). S_{21} is a complex number.

The uncertainty is defined as the difference between two measured signals (from the i-th and the j-th measurement):

$$S_{21\_uncertainty}^{ij} = S_{21}^{i} - S_{21}^{j}, \quad \begin{matrix} i, j = 1, \ldots, n \\ i \neq j \end{matrix} \tag{3.3}$$

The averaged uncertainty is calculated by averaging the uncertainties of all possible combinations of signal pairs in one set of measurements:

$$S_{21\_av\_uncertainty} = \sum_{\substack{i=1, j=2 \\ i \neq j}}^{n} \left(S_{21\_uncertainty}^{ij} \right) \Big/ \binom{n}{2} \tag{3.4}$$

Then, the signal-to-uncertainty level (SUR) is calculated as the ratio between the averaged signal level and the averaged uncertainty level:

$$\mathrm{SUR} = 20 * \log_{10}\left(\left| S_{21\_av\_signal} \right| \Big/ \left| S_{21\_av\_uncertainty} \right| \right) \tag{3.5}$$

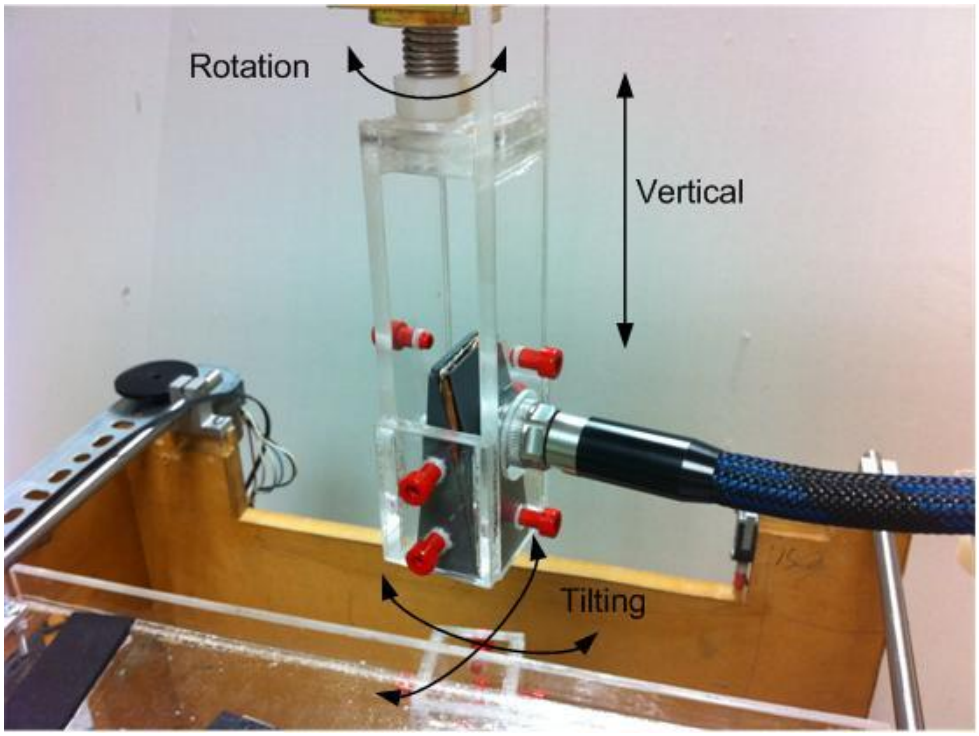

Fig. 3.10. Illustration of the source of the uncertainties associated with the vertical antenna motion.

The results obtained by measurements with antenna 1 on a low-loss homogeneous phantom are shown in Fig. 3.11. The results for antenna 2 are shown in Fig. 3.12. As these figures have shown, for either set of antennas, the averaged signal level decreases with frequency, which is as expected. The uncertainty level, which is a random process, demonstrates a similar trend. By using a step line fitting both cases, we conclude that we are facing an uncertainty level of -80 dB from 3 GHz to 7.5 GHz and -100 dB from 7.5 GHz to 10 GHz.

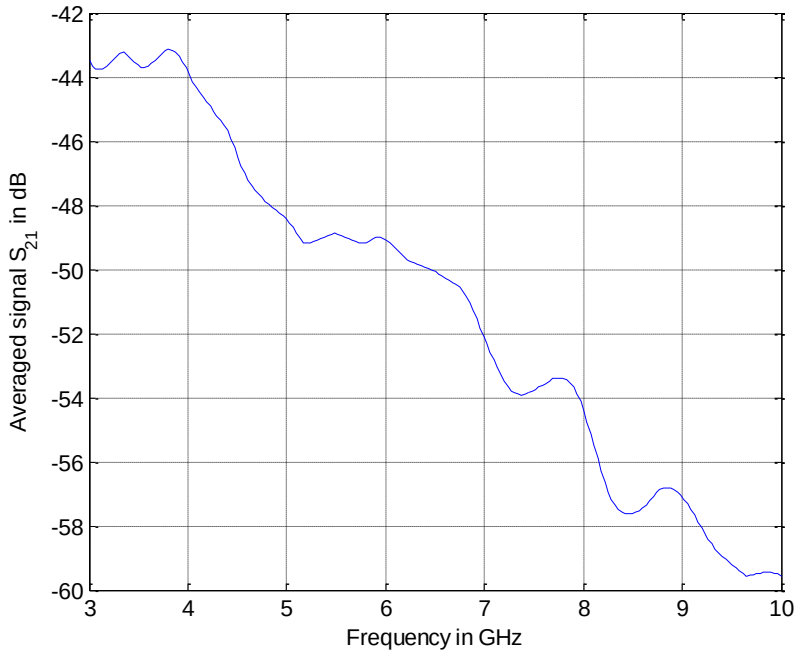

(a)

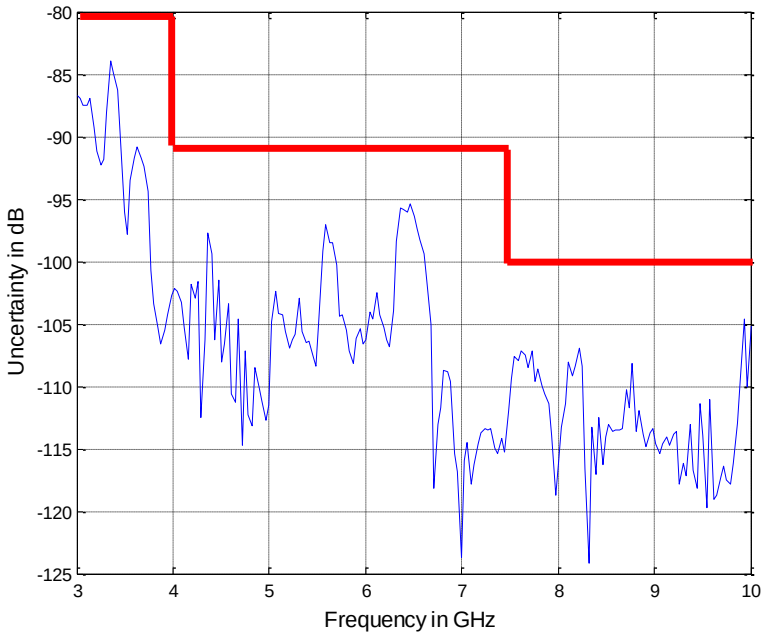

(b)

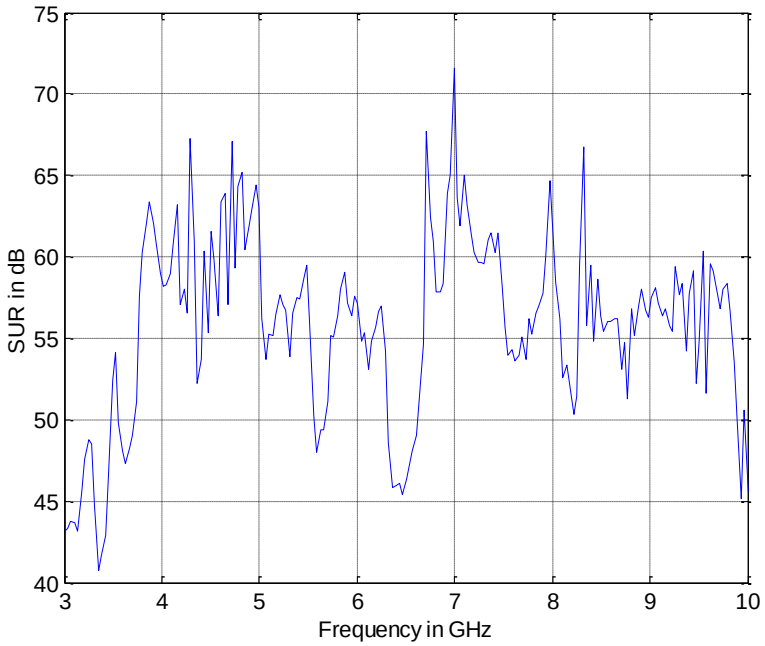

(c)

Fig. 3.11. Results for antenna 1 for vertical motion only. (a) Averaged signal. (b) Averaged uncertainty. (c) Signal-to-uncertainty ratio.

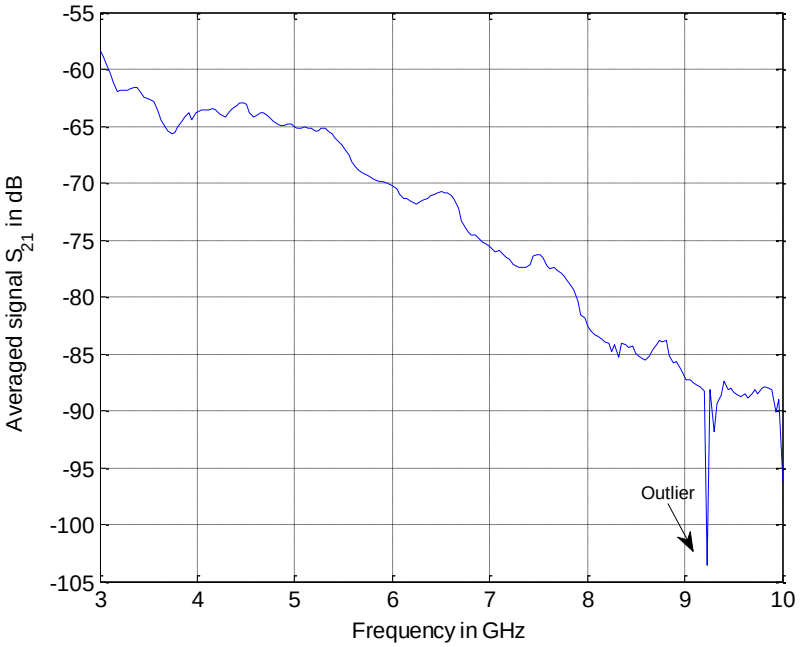
-55
-60
-65
-70
-75
-80
-85
-90
-95
-100
-105
3
4
5
6
7
8
9
10
Averaged signal S_{21} in dB
Frequency in GHz
Outlier

(a)

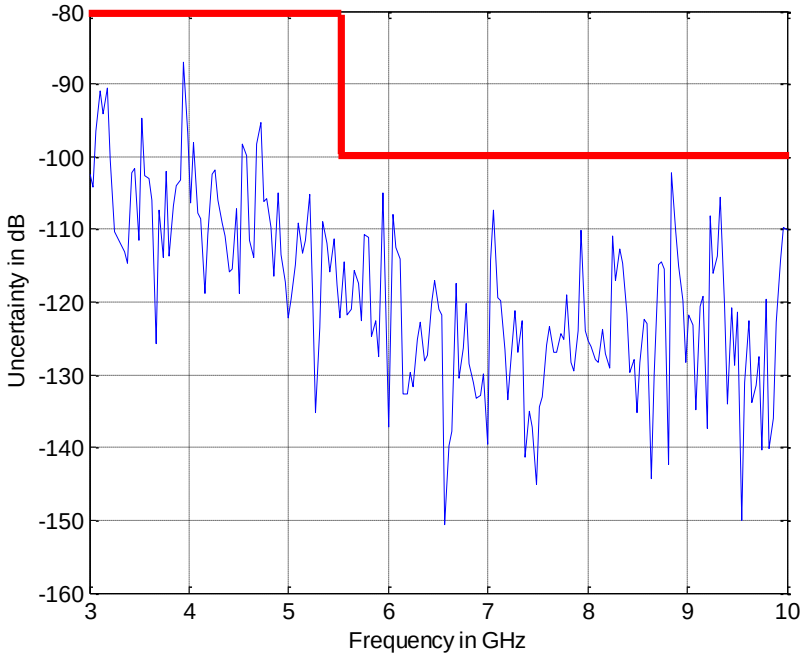
-80
-90
-100
-110
-120
-130
-140
-150
-160
3
4
5
6
7
8
9
10
Uncertainty in dB
Frequency in GHz

(b)

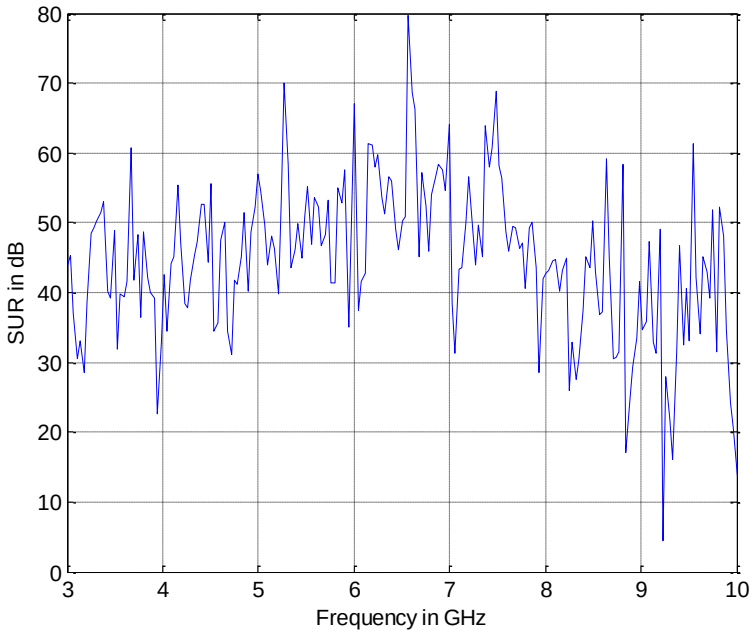

(c)

Fig. 3.12. Results for antenna 2 for vertical motion only. (a) Averaged signal. (b) Averaged uncertainty. (c) Signal-to-uncertainty ratio.

This uncertainty level is higher than the noise floor of the instrument obtained in section 3.2. Thus we can conclude that the uncertainty level of the system deteriorates due to the vertical motion of the antennas. However, the SUR plots for both antennas still show acceptable signal-to-noise ratio in the sense that the measured signal is much stronger than the uncertainty level of the system.

Alternative evaluation method:

The evaluation method used above uses the S_{21} in complex form. Thus the uncertainty level incorporates contributions by the uncertainties in both S_{21} magnitude and S_{21} phase. When VNA performs an *S*-parameter sweep, the results

are in the form of S_{21} magnitude and S_{21} phase. Thus, it is worth to evaluate the uncertainty separately for magnitude and phase.

For uncertainties associated with the magnitude, the averaged signal is calculated as:

$$S_{21\_av\_signal} = \sum_{i=1}^{n} \left| S_{21}^{i} \right| \Big/ n \tag{3.6}$$

where n is the number of measurements (n = 20). The averaged uncertainty is calculated by averaging the uncertainties of all possible combinations of signal magnitude pairs in one set of measurements:

$$S_{21\_av\_uncertainty} = \sum_{\substack{i=1,\, j=2 \\ i \neq j}}^{n} \left(\left| S_{21}^{i} \right| - \left| S_{21}^{j} \right| \right) \Big/ \binom{n}{2} \tag{3.7}$$

Then, the SUR is calculated using formula (3.5). The results for antenna 1 are shown in Fig. 3.13. The results for antenna 2 are shown in Fig. 3.14.

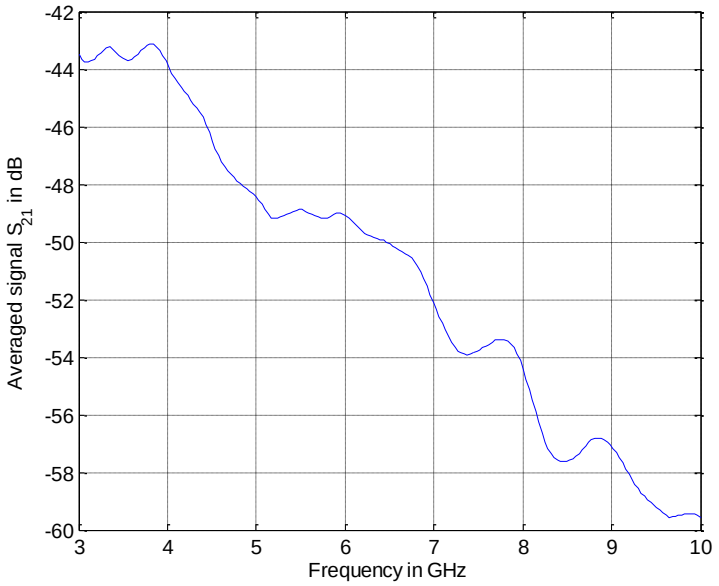

(a)

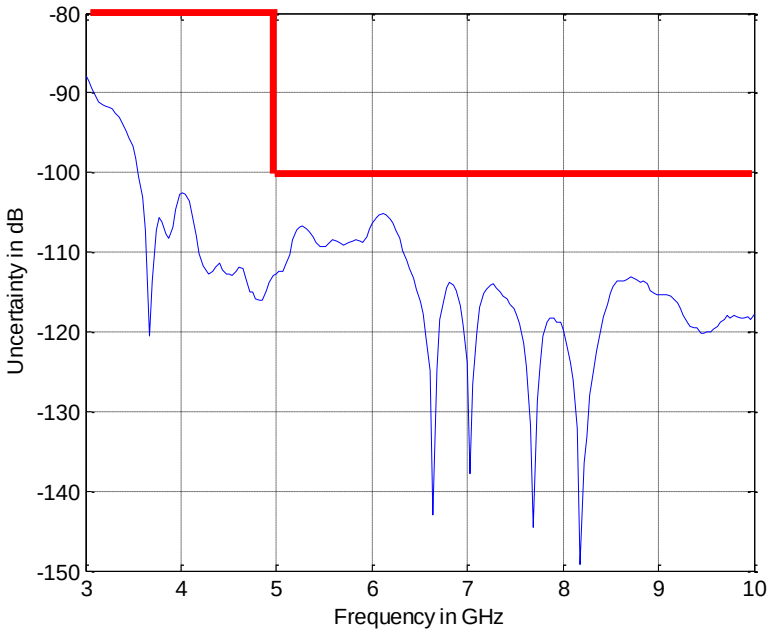

(b)

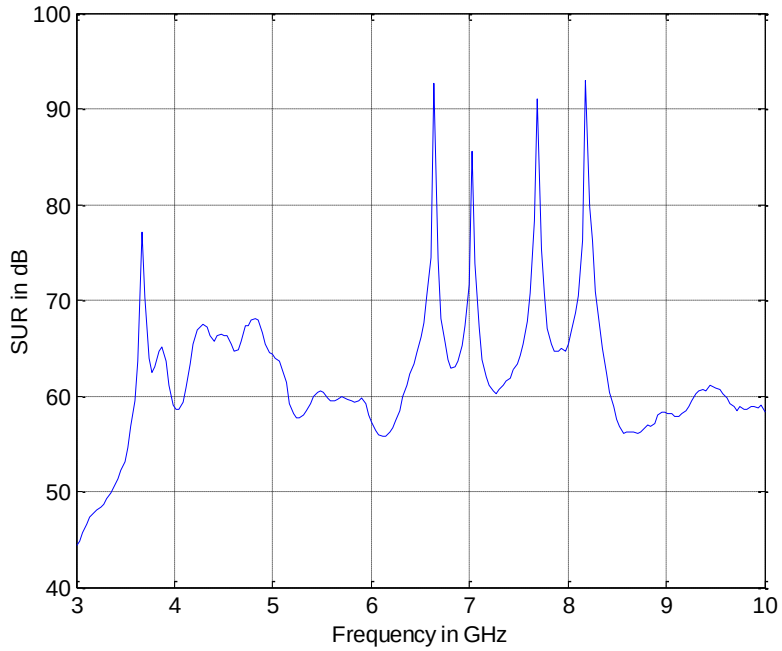

(c)

Fig. 3.13. Results for antenna 1 for vertical motion only when using magnitude information only. (a) Averaged signal. (b) Averaged uncertainty. (c) Signal-to-uncertainty ratio.

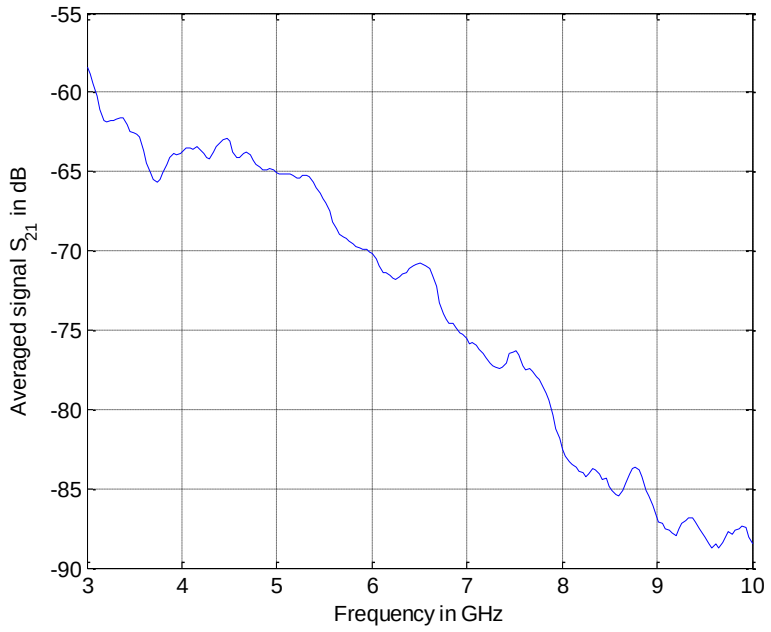
-55
-60
-65
-70
-75
-80
-85
-90
3
4
5
6
7
8
9
10
Averaged signal S_{21} in dB
Frequency in GHz

(a)

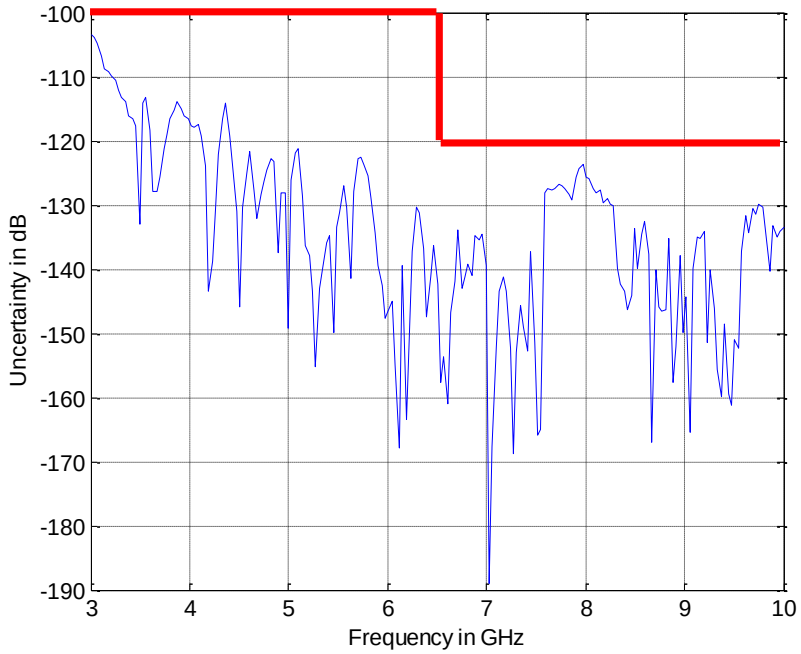
-100
-110
-120
-130
-140
-150
-160
-170
-180
-190
3
4
5
6
7
8
9
10
Uncertainty in dB
Frequency in GHz

(b)

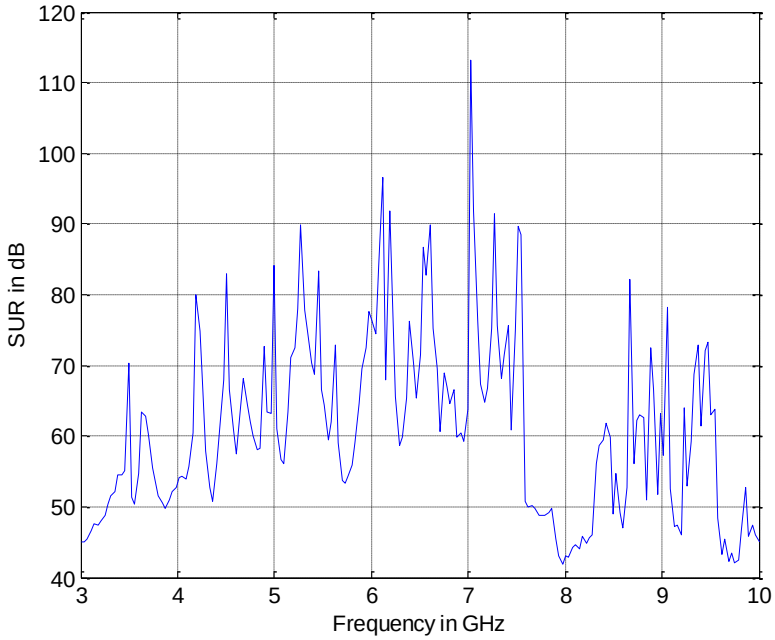

(c)

Fig. 3.14. Results for antenna 2 for vertical motion only when using magnitude information only. (a) Averaged signal. (b) Averaged uncertainty. (c) Signal-to-uncertainty ratio.

Based on Fig. 3.13, the measurements with antenna 1 give comparable results between complex-value evaluation and magnitude-only evaluation. This indicates that the phase uncertainty, which is defined as

$$\sphericalangle S^{ij}_{21\_\text{uncertainty}} = \sphericalangle S^{i}_{21} - \sphericalangle S^{j}_{21} \tag{3.8}$$

is small. This is confirmed in Fig. 3.15, which is a plot of the averaged phase differences versus frequency calculated using

$$\sphericalangle S_{21\_\text{av\_uncertainty}} = \sum_{\substack{i=1,\, j=2 \\ i \neq j}}^{n} \left(\sphericalangle S^{ij}_{21\_\text{uncertainty}} \right) \Bigg/ \binom{n}{2} \tag{3.9}$$

Where n is the number of measurements (n = 20). The two points which are far from the 0 degree line are regarded as outliers since there are 201 frequency sampling points in the plot.

Based on Fig. 3.14, the magnitude-only evaluation for antenna 2 produces a much higher SUR values. The uncertainty plot (Fig. 3.14 (b)) shows that the uncertainty level is below -100 dB from 3 GHz to 6.5 GHz and -120 dB from 6.5 GHz to 10 GHz by using step line fitting. This is much better than the results obtained using complex-number evaluation. This indicates big errors in the phase information, which is confirmed in Fig. 3.16. The phase measured with antenna 2 fluctuates significantly, especially in the high frequency range. This behavior is confirmed by repeated measurements with antenna 2 on different phantoms, conclude that it is an intrinsic problem, which is likely to be the result of loose connections inside the antenna.

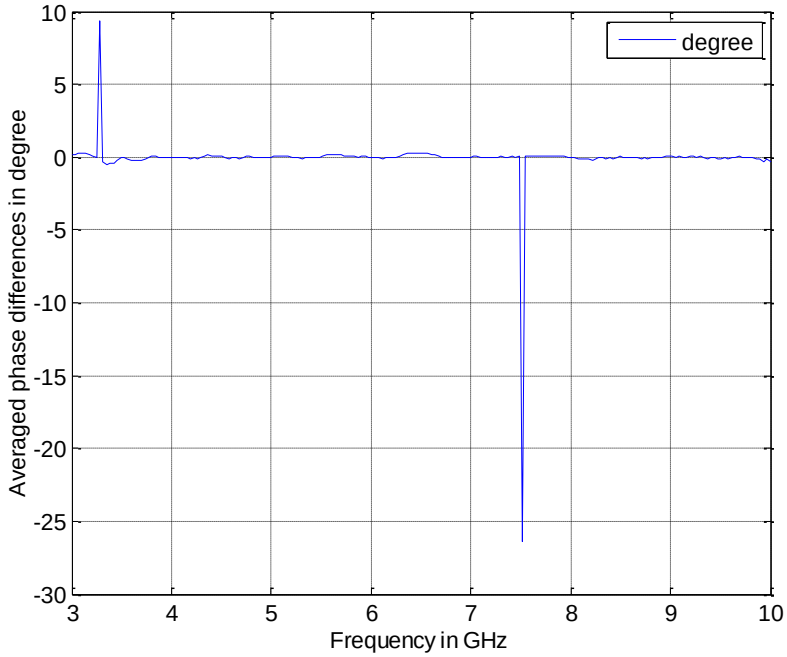

Fig. 3.15. Averaged phase uncertainty for antenna 1.

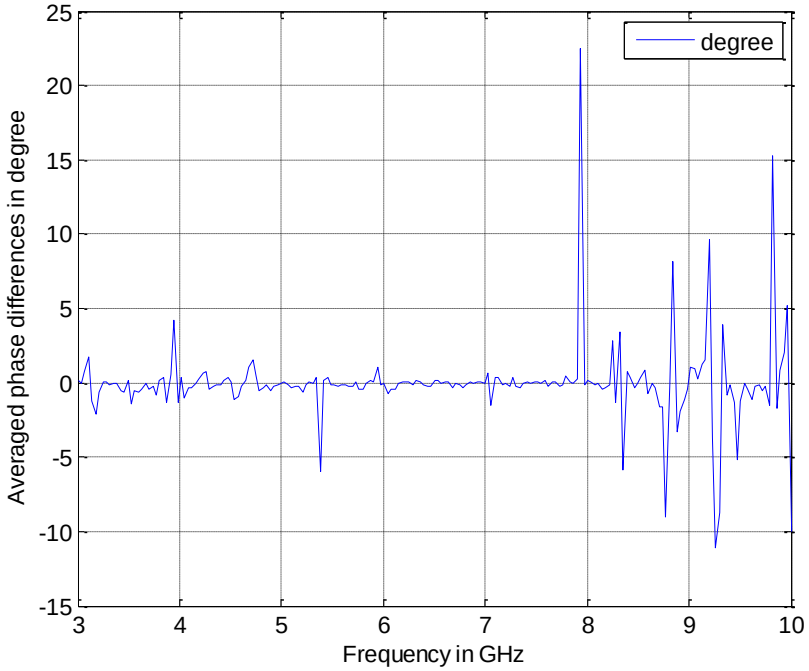

Fig. 3.16. Averaged phase uncertainty for antenna 2.

3.3.2. Uncertainties Associated with Lateral Motion

The uncertainties associated with lateral motion result from two factors. The first factor is the accumulated error in movement distance with the step motors. The second factor is the shaking of the scanning table due to the lateral motion.

To quantitatively measure the uncertainties, a measurement scenario involving only the lateral motion of the scanning table is performed. In this scenario, the two antennas are aligned along each other's boresight on the opposite sides of the phantom. The solenoids are off permanently, and the heights of the antennas are adjusted so that the apertures of the antennas are not touching the plexiglass plates constraining the phantom. The step motors move the scanning table over a 40 mm by 40 mm plane in a raster order with 10 mm spatial sampling rate. At each sampling point, a VNA sweep from 3 GHz to 10 GHz is performed and the results (S_{21} magnitude and phase) are saved. Ten of these measurements are taken. Averaged signal level, averaged uncertainty level and SUR are calculated using formulas (3.2), (3.4) and (3.5), respectively. However, since these are 2-D measurements, the results are in 3-dimensional matrix form containing data at each frequency point at each spatial sampling point. To visualize the results, 2-D pseudocolor plots showing the intensity of the results at each spatial sampling point are generated at 3 frequencies (3 GHz, 6 GHz, 10 GHz) separately. Also, instead of plotting 2-D SUR directly, histograms are plotted showing the distribution of the SUR. The *x*-axis shows the SUR in dB, the *y*-axis shows the number counts of points associated with each SUR bin.

To demonstrate the differences between the averaged signal and averaged uncertainty, common color bars are used for each pairs of plots at the same frequency.

Fig. 3.17 and Fig. 3.18 show the results for antenna 1. Fig. 3.19 and Fig. 3.20 show the results for antenna 2. In both measurements, the averaged signal is much stronger than the averaged uncertainty at all 3 sampling frequencies.

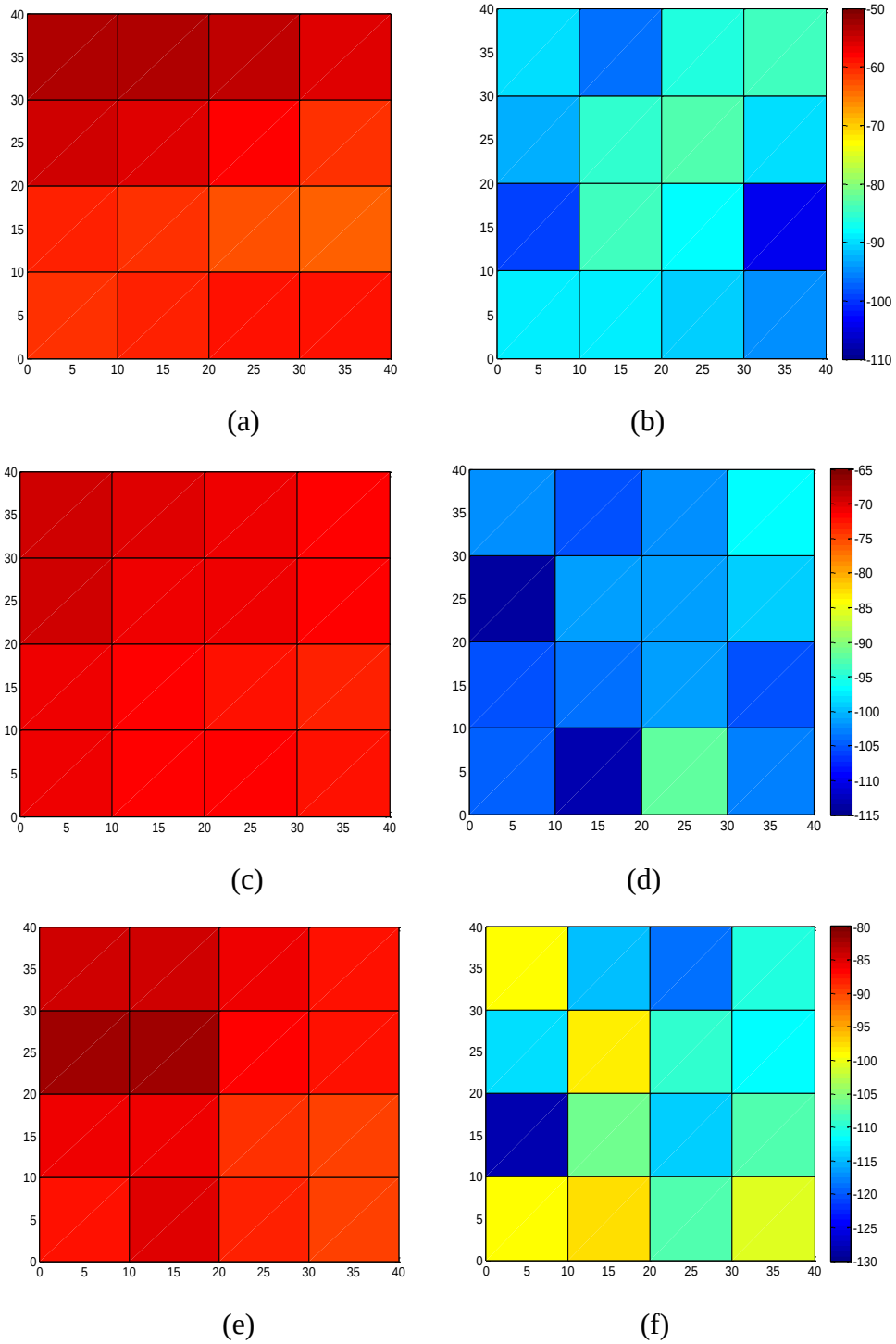

Fig. 3.17. Results for antenna 1 for lateral motion only when using complex-value evaluation. 2-D plot of averaged signal in dB at: (a) 3 GHz; (c) 6 GHz; (e) 10 GHz. 2-D plot of averaged uncertainty in dB at: (b) 3 GHz; (d) 6 GHz; (f) 10 GHz.

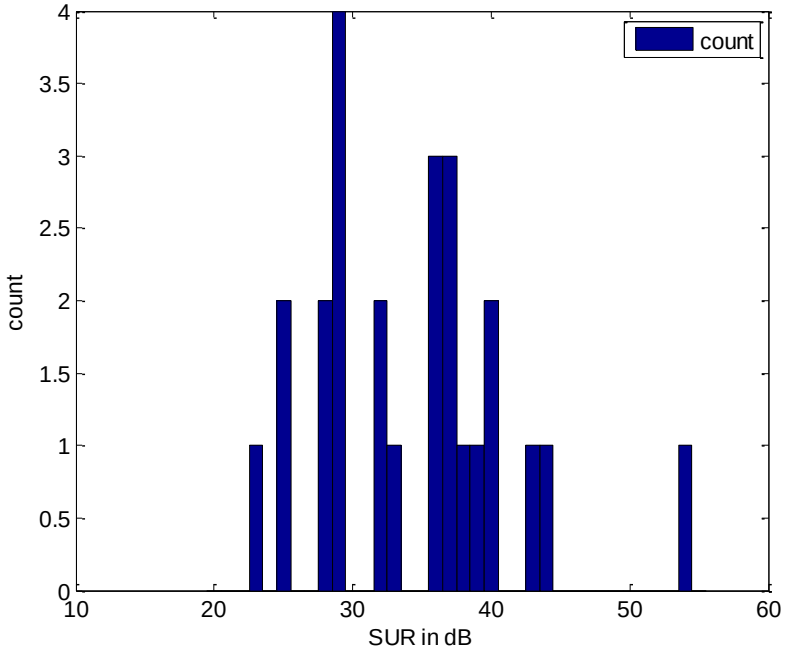
count
count
SUR in dB
0
0.5
1
1.5
2
2.5
3
3.5
4
10
20
30
40
50
60

(a)

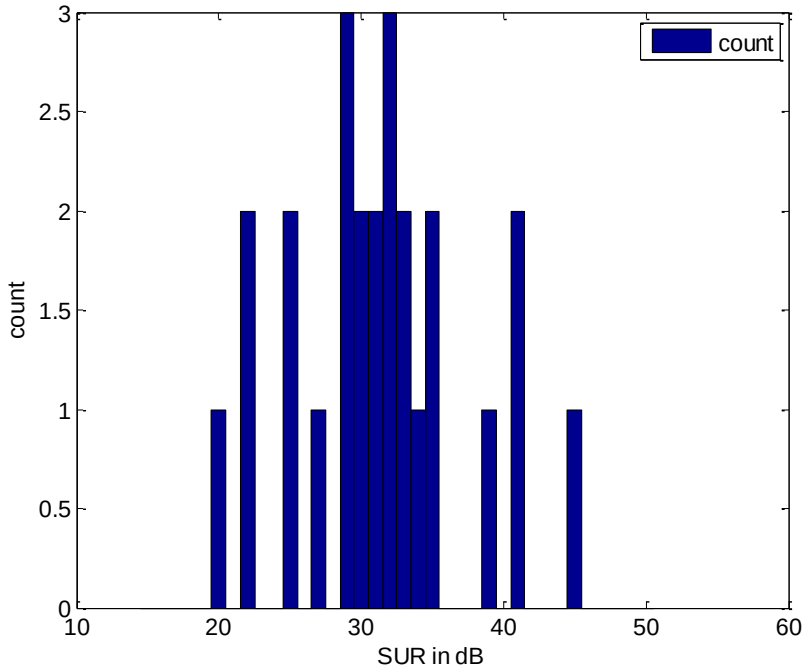
count
count
SUR in dB
0
0.5
1
1.5
2
2.5
3
10
20
30
40
50
60

(b)

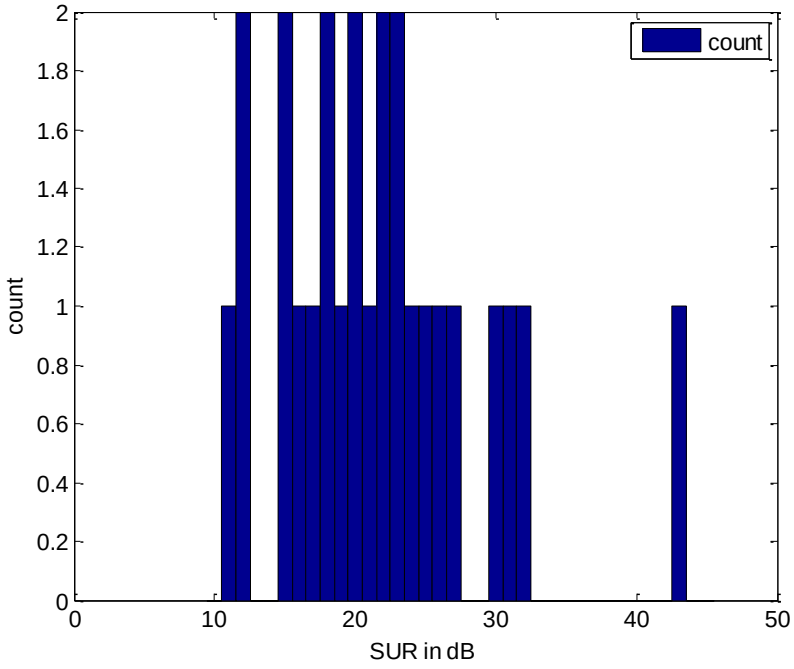

(c)

Fig. 3.18. Results for antenna 1 for lateral motion only when using complex-value evaluation. Histogram of SUR distribution at: (a) 3 GHz; (b) 6 GHz; (c) 10 GHz.

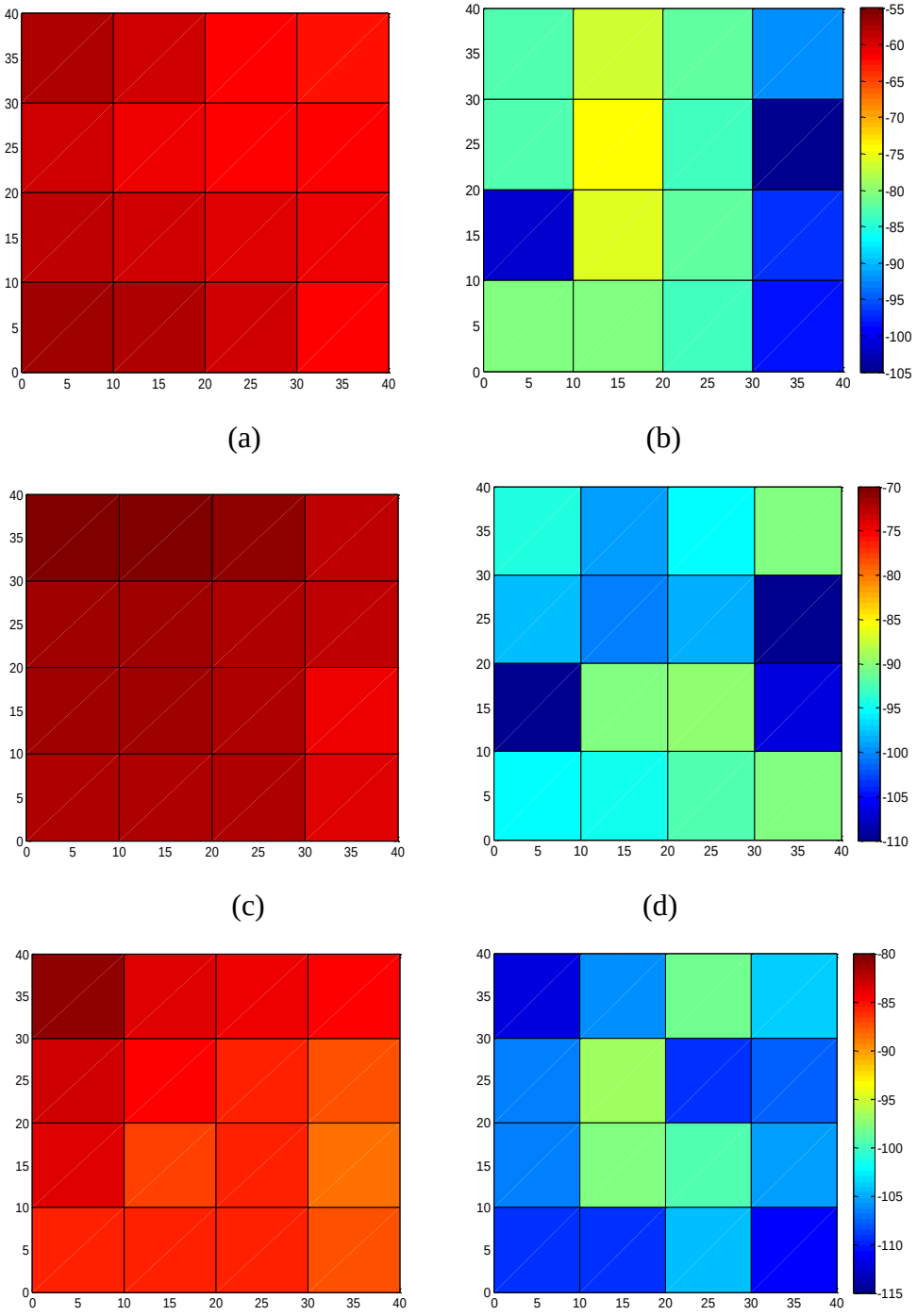

Fig. 3.19. Results for antenna 2 for lateral motion only when using complex-value evaluation. 2-D plot of averaged signal in dB at: (a) 3 GHz; (c) 6 GHz; (e) 10 GHz. 2-D plot of averaged uncertainty in dB at: (b) 3 GHz; (d) 6 GHz; (f) 10 GHz.

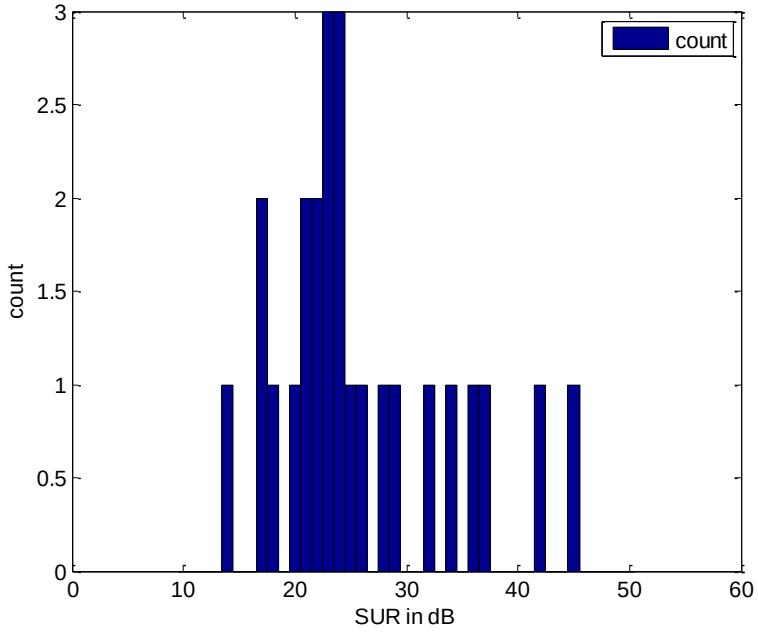
count
count
SUR in dB
0
0.5
1
1.5
2
2.5
3
0
10
20
30
40
50
60

(a)

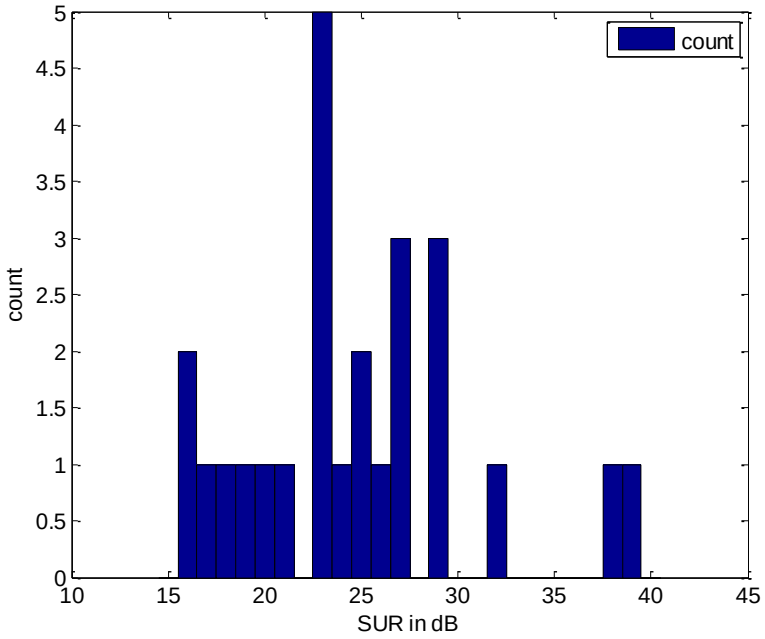
count
count
SUR in dB
0
0.5
1
1.5
2
2.5
3
3.5
4
4.5
5
10
15
20
25
30
35
40
45

(b)

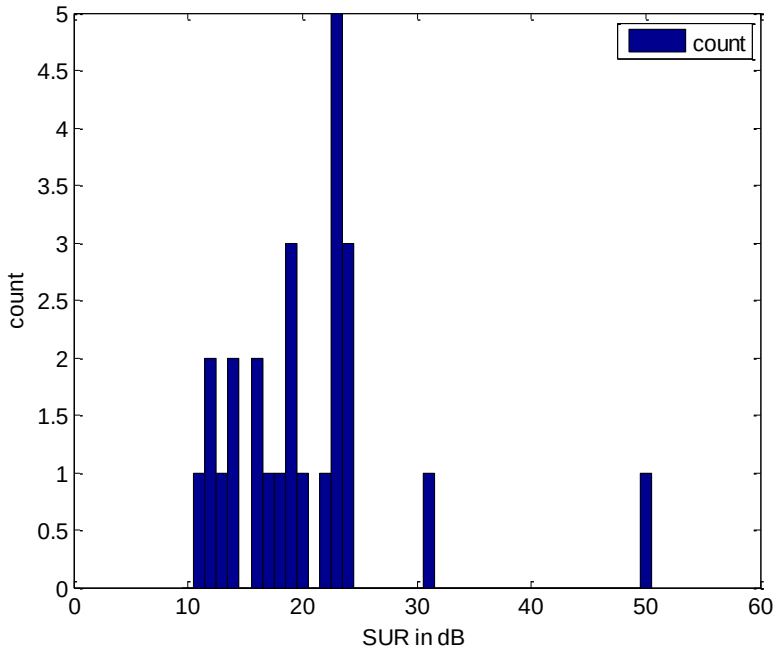

(c)

Fig. 3.20. Results for antenna 2 for lateral motion only when using complex-value evaluation. Histogram of SUR distribution at: (a) 3 GHz; (b) 6 GHz; (c) 10 GHz.

Furthermore, the averaged SUR is calculated by averaging the SUR for every spatial sampling point over the scanned area:

$$\mathrm{SUR}_{\mathrm{av}} = \sum_{i=0,\,j=0}^{n} \mathrm{SUR}^{ij} \Big/ n^2 \qquad (3.10)$$

where n = 4 in this case. The SUR average is shown in Table 3.3 for both antennas.

Table 3.3. SUR average for both antennas

	SUR_{av}	
Frequency	**Antenna 1**	**Antenna 2**
3 GHz	34.4 dB	25.9 dB
6 GHz	31.3 dB	24.8 dB
10 GHz	21.7 dB	20.5 dB

Alternative evaluation method:

The measurement data are also evaluated using magnitude data only by using formula (3.7). The plots generated from magnitude only evaluation show comparable signal levels but lowered uncertainty levels. This leads to significantly higher SUR values which can be seen from the SUR histogram shown in Fig. 3.21 and Fig. 3.22 as well as SUR average shown in Table 3.4.

Table 3.4. SUR average for both antennas calculated using magnitude only

	SUR_{av}	
Frequency	**Antenna 1**	**Antenna 2**
3 GHz	38.6 dB	37.5 dB
6 GHz	40.2 dB	35.5 dB
10 GHz	34.0 dB	31.6 dB

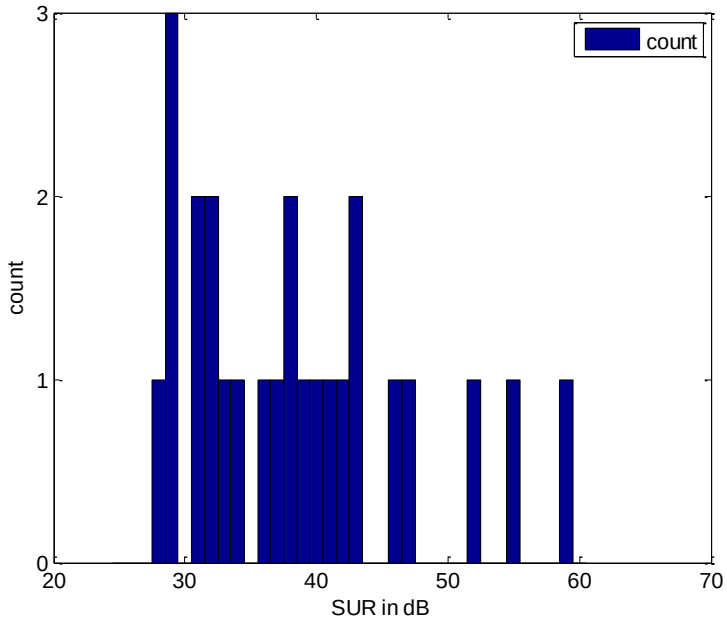
count
count
SUR in dB
0
1
2
3
20
30
40
50
60
70

(a)

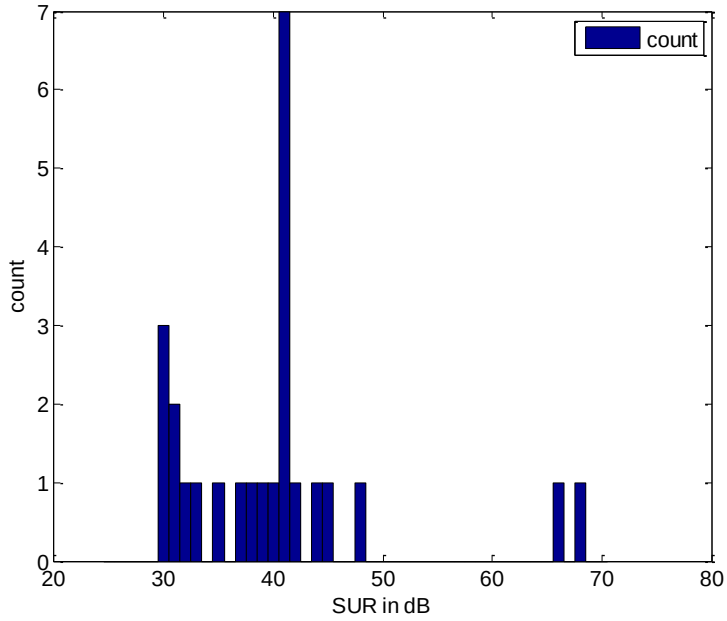
count
count
SUR in dB
0
1
2
3
4
5
6
7
20
30
40
50
60
70
80

(b)

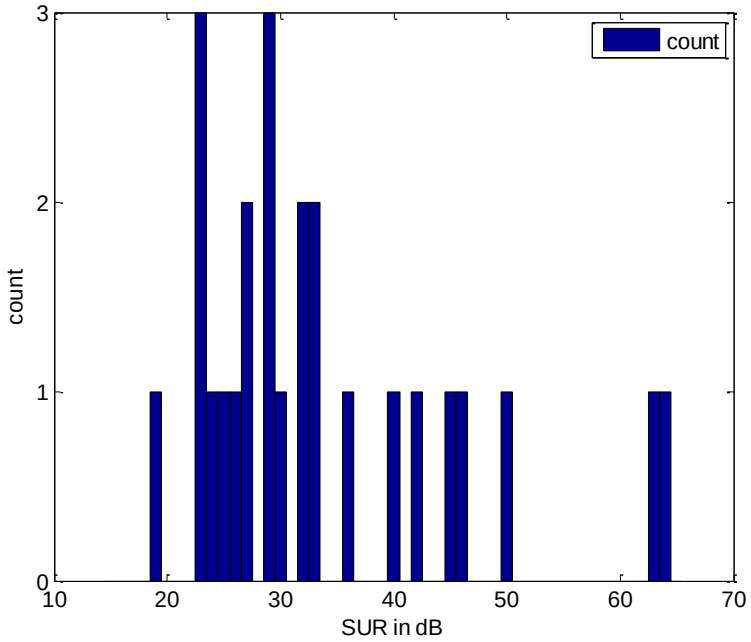

(c)

Fig. 3.21. Histogram showing the distribution of SUR for measurements with antenna 1 when using magnitude only at: (a) 3 GHz; (b) 6 GHz; (c) 10 GHz.

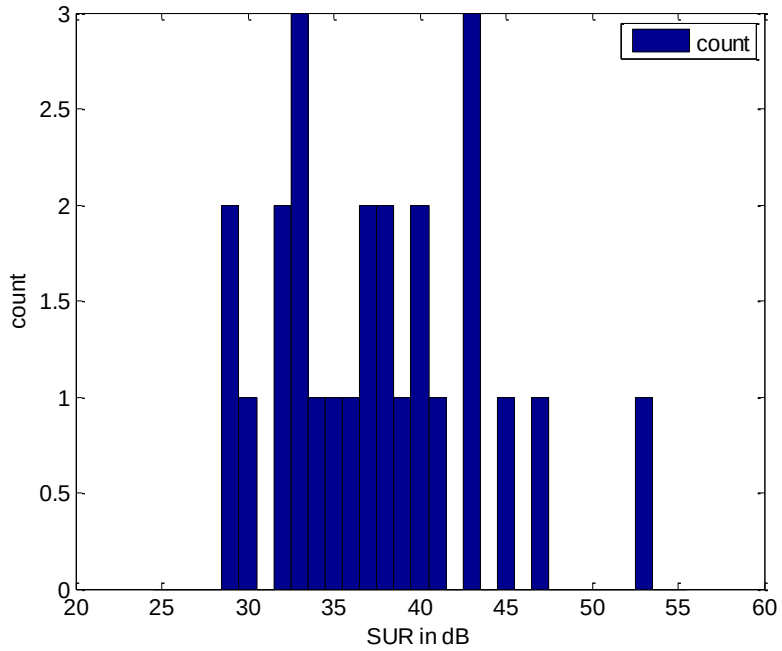

(a)

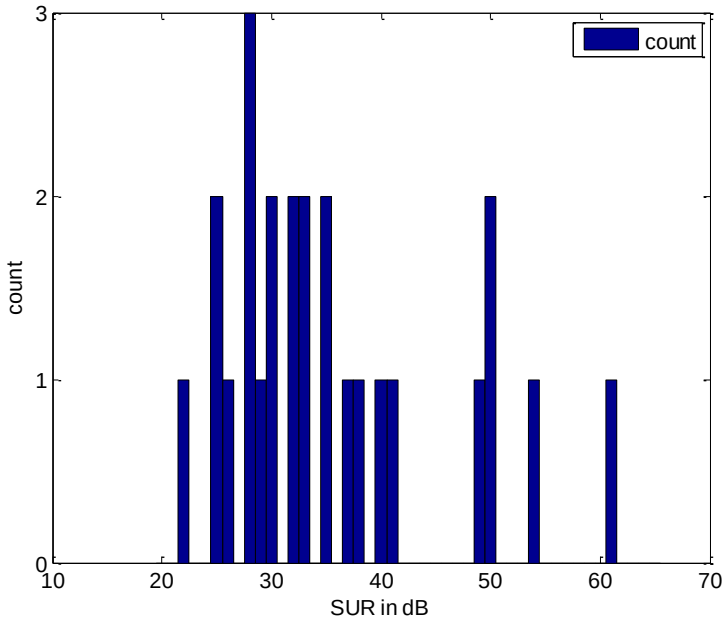

(b)

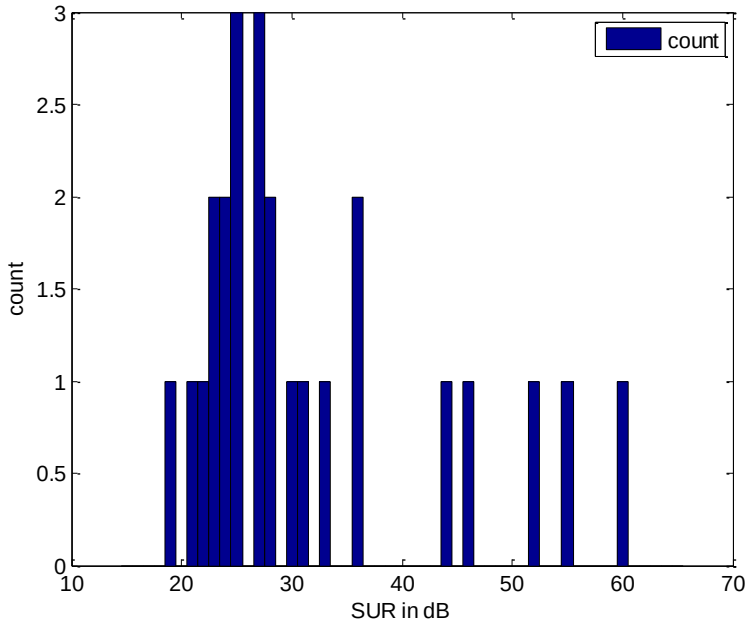

(c)

Fig. 3.22. Histogram showing the distribution of SUR for measurements with antenna 2 when using magnitude only at: (a) 3 GHz; (b) 6 GHz; (c) 10 GHz.

The fact that with magnitude information only, higher SUR is obtained indicates that the phase information contains big errors. To conclude, the measurement results in this section have demonstrated that the uncertainties introduced by the lateral motion of the scanning table have big impact on the measured phase information. However, the measured signals are significantly stronger than the uncertainty levels, indicating that the system is robust against uncertainty introduced by the lateral motion.

3.4. Measurement Uncertainties of a 2-antenna Circuit

The last component in the system which is a source of uncertainties is the antenna sensor itself. In the previous sections (e.g., 3.3.1), results have shown that the antenna fabrication can be a source of uncertainties depending on the quality of the soldering and the connections. However, it is hard to distinguish the uncertainties introduced by the antennas alone from other source of uncertainties. Thus, in this section, the uncertainties of the overall system (2-antenna circuits) are studied using both sets of antennas. These demonstrate the real uncertainty levels encountered in practical planar raster-scanning measurements.

Complete 2-D raster scan measurements of a target phantom are performed using two sets of antennas over a 9 cm by 9 cm area which is centered at the center of the phantom. The target phantom is 18 cm by 18 cm wide and 4.5 cm thick with tumor simulant embedded in the middle. The dielectric properties of the phantom are listed in Appendix C. The results are interpreted using three

different evaluation methods, complex-value evaluation, magnitude-only evaluation and phase-only evaluation.

3.4.1. Complex Value Evaluation

The complex-value evaluation uses the same formulas as in section 3.3.2, i.e., formula (3.2), (3.4) and (3.5). The data at three frequency points (3 GHz, 6 GHz and 10 GHz) are plotted. The results from the measurement with antenna 1 are shown in Fig. 3.23 and Fig. 3.24. The results for the measurement with antenna 2 are shown in Fig. 3.25 and Fig. 3.26.

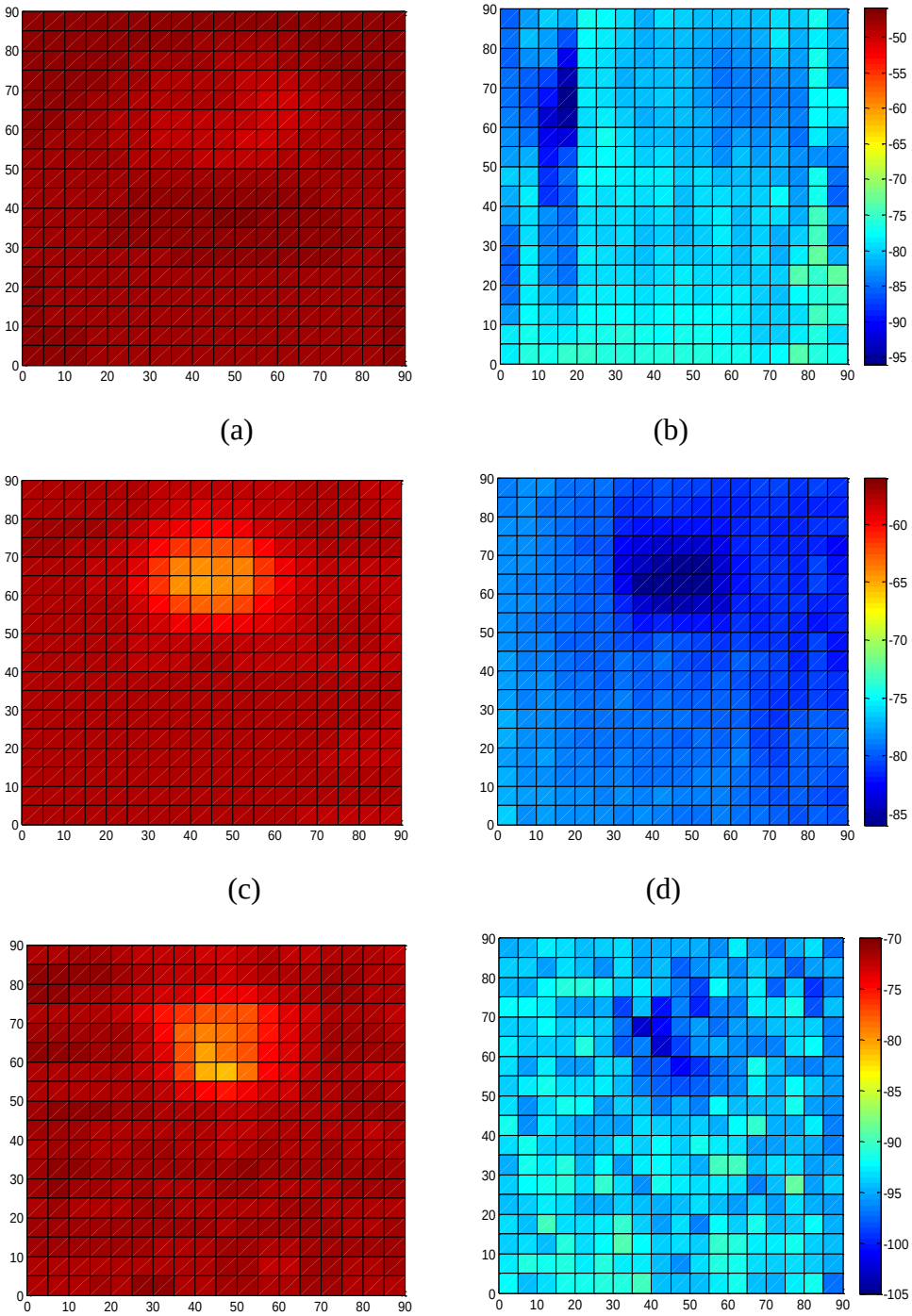

Fig. 3.23. Results of the 2-D scan using antenna 1 interpreted using complex-value evaluation. 2-D plot of averaged signal in dB at: (a) 3 GHz; (c) 6 GHz; (e) 10 GHz. 2-D plot of averaged uncertainty in dB at: (b) 3 GHz; (d) 6 GHz; (f) 10 GHz.

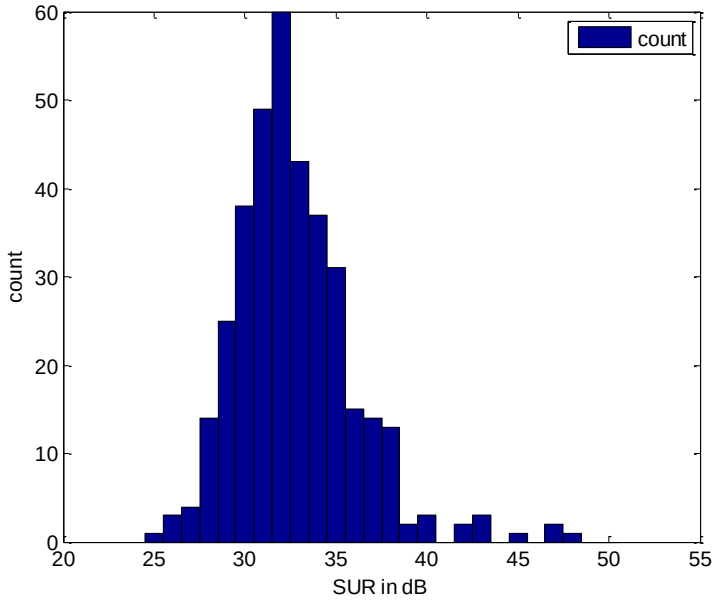
count
count
SUR in dB
0
10
20
30
40
50
60
20
25
30
35
40
45
50
55

(a)

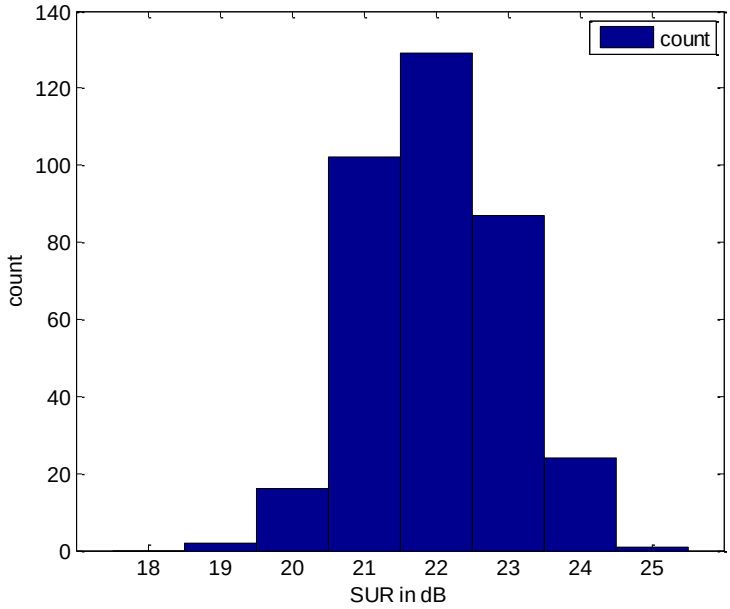
count
count
SUR in dB
0
20
40
60
80
100
120
140
18
19
20
21
22
23
24
25

(b)

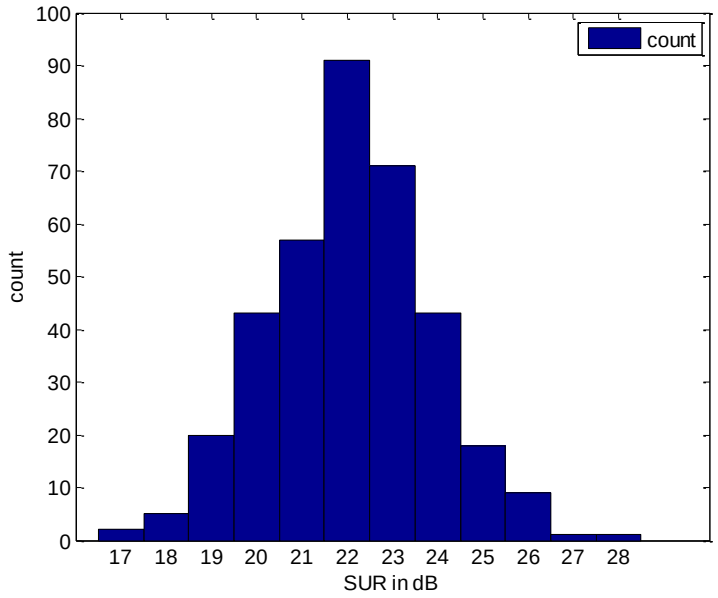

(c)

Fig. 3.24. Results of 2-D scan using antenna 1 interpreted using complex-value evaluation. Histogram of SUR distribution at: (a) 3 GHz; (b) 6 GHz; (c) 10 GHz.

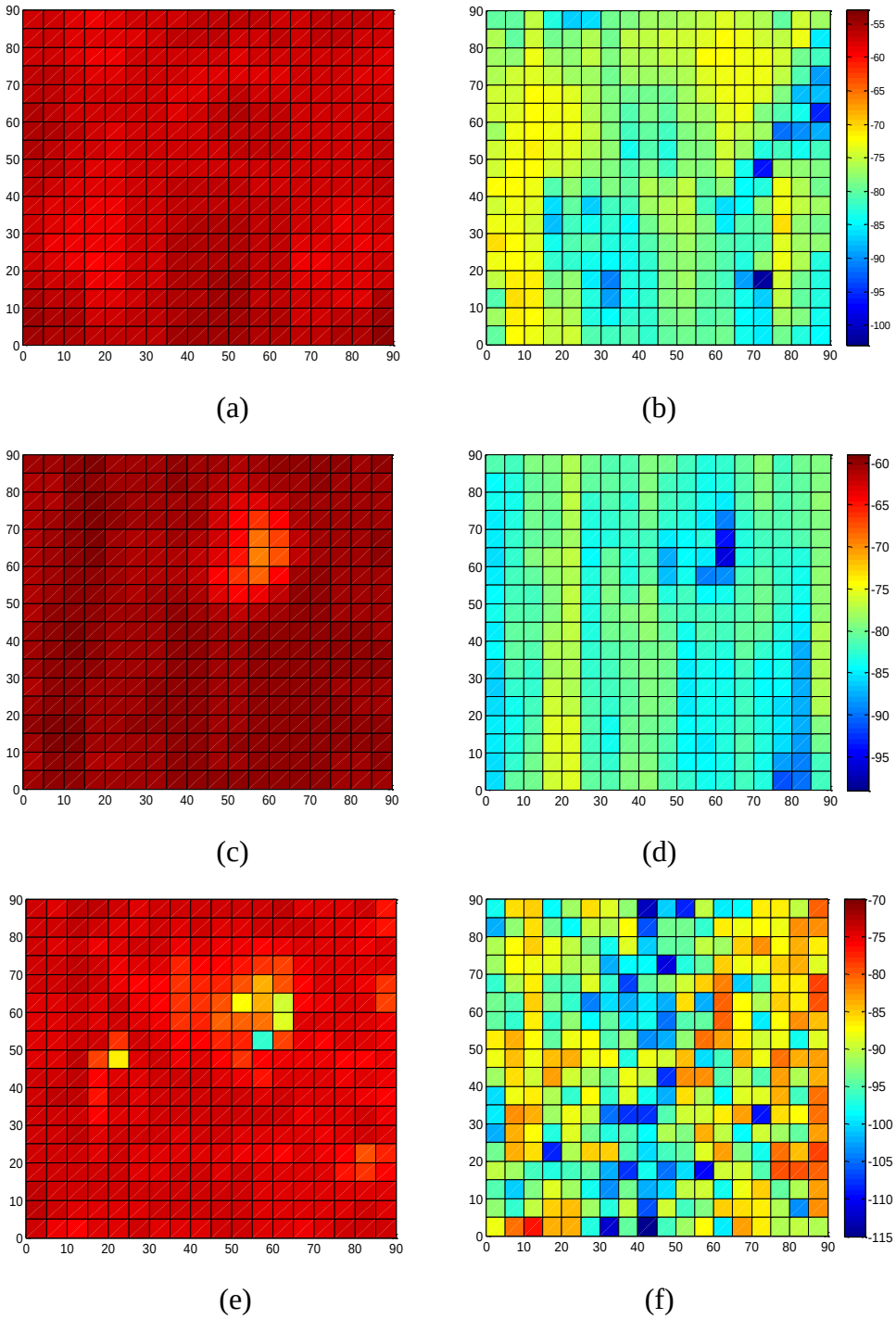

Fig. 3.25. Results of the 2-D scan using antenna 2 interpreted using complex-value evaluation. 2-D plot of averaged signal in dB at: (a) 3 GHz; (c) 6 GHz; (e) 10 GHz. 2-D plot of averaged uncertainty in dB at: (b) 3 GHz; (d) 6 GHz; (f) 10 GHz.

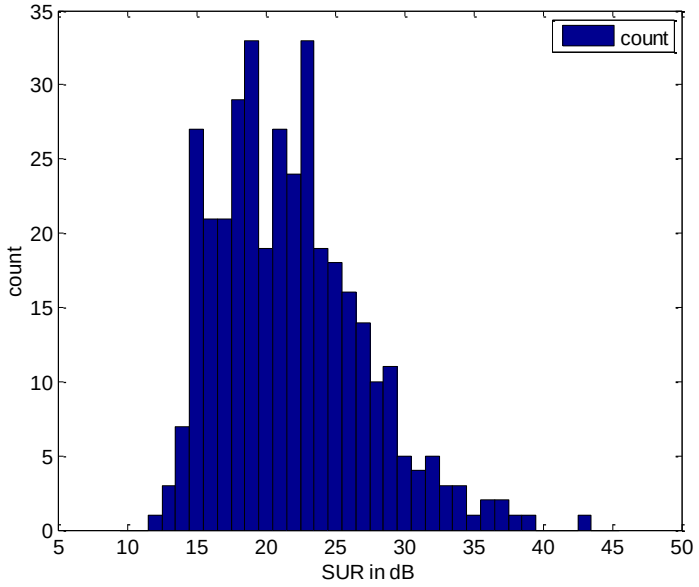
count
count
SUR in dB
0
5
10
15
20
25
30
35
5
10
15
20
25
30
35
40
45
50

(a)

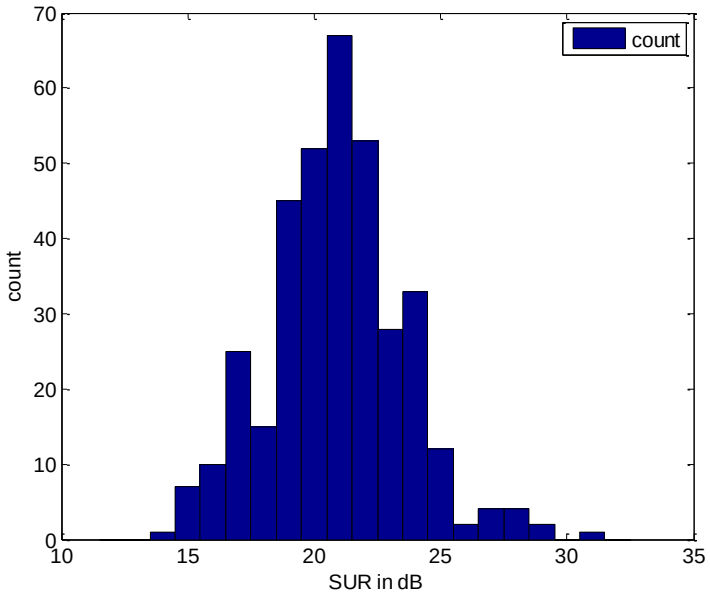
count
count
SUR in dB
0
10
20
30
40
50
60
70
10
15
20
25
30
35

(b)

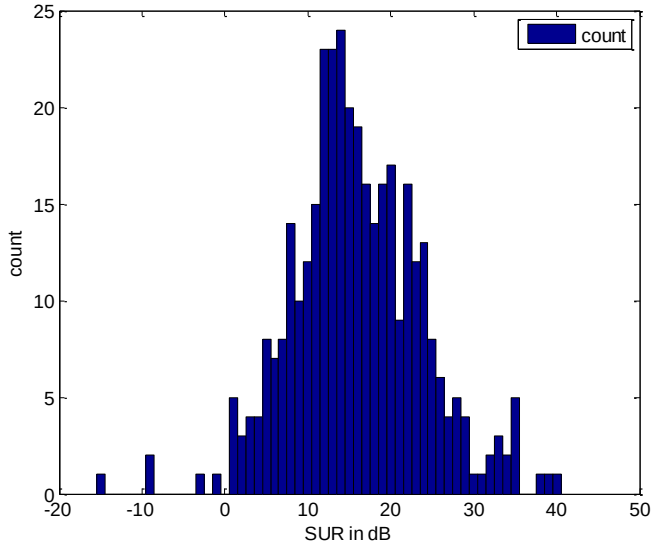

(c)

Fig. 3.26. Results of 2-D scan using antenna 2 interpreted using complex-value evaluation. Histogram of SUR distribution at: (a) 3 GHz; (b) 6 GHz; (c) 10 GHz.

The SUR average of all spatial sampling points over the scanned area is also calculated using formula (3.10) and the results are shown in Table 3.5.

Table 3.5. SUR average for both antennas for a 9×9 cm^2 scan

	SUR_{av}	
Frequency	**Antenna 1**	**Antenna 2**
3 GHz	32.7 dB	21.8 dB
6 GHz	22.0 dB	21.0 dB
10 GHz	22.1 dB	16.1 dB

For measurement data with antenna 1, according to Fig. 3.23, the signal levels at all 3 frequencies are significantly stronger than the uncertainty levels. Due to the embedded tumor simulant, the signal level measured near the tumor's

position is lower than the background. However, the uncertainty levels at these positions are also lower as compared to the uncertainty levels of the background. The SUR plots exhibit a Gaussian-like distribution, with most points distributed close to the SUR averages shown in Table 3.5.

For measurement data with antenna 2, according to Fig. 3.25, the signal levels at 3 GHz and 6 GHz are also significantly stronger than the uncertainty levels. However, at 10 GHz, based on the SUR histogram plot, there are several points scattered below 0 dB. This indicates that at certain spatial sampling points, the signal levels are lower than the uncertainty levels.

In summary, the measurement with antenna 1 generates better SUR as compared to the measurement with antenna 2. Thus, it is necessary to evaluate the measurement data using magnitude information and phase information separately to find out the cause of the poor performance for antenna 2 at high frequency.

3.4.2. Magnitude Only Evaluation

The magnitude-only evaluation uses formulas (3.6), (3.7) and (3.5). The data at three frequency points (3 GHz, 6 GHz and 10 GHz) are plotted. The results from the measurements with antenna 1 are shown in Fig. 3.27 and Fig. 3.28. The results from measurements with antenna 2 are shown in Fig. 3.29 and Fig. 3.30. The SUR averages of all spatial sampling points over the 2-D plane are also calculated using formula (3.10) and the results are shown in Table 3.6.

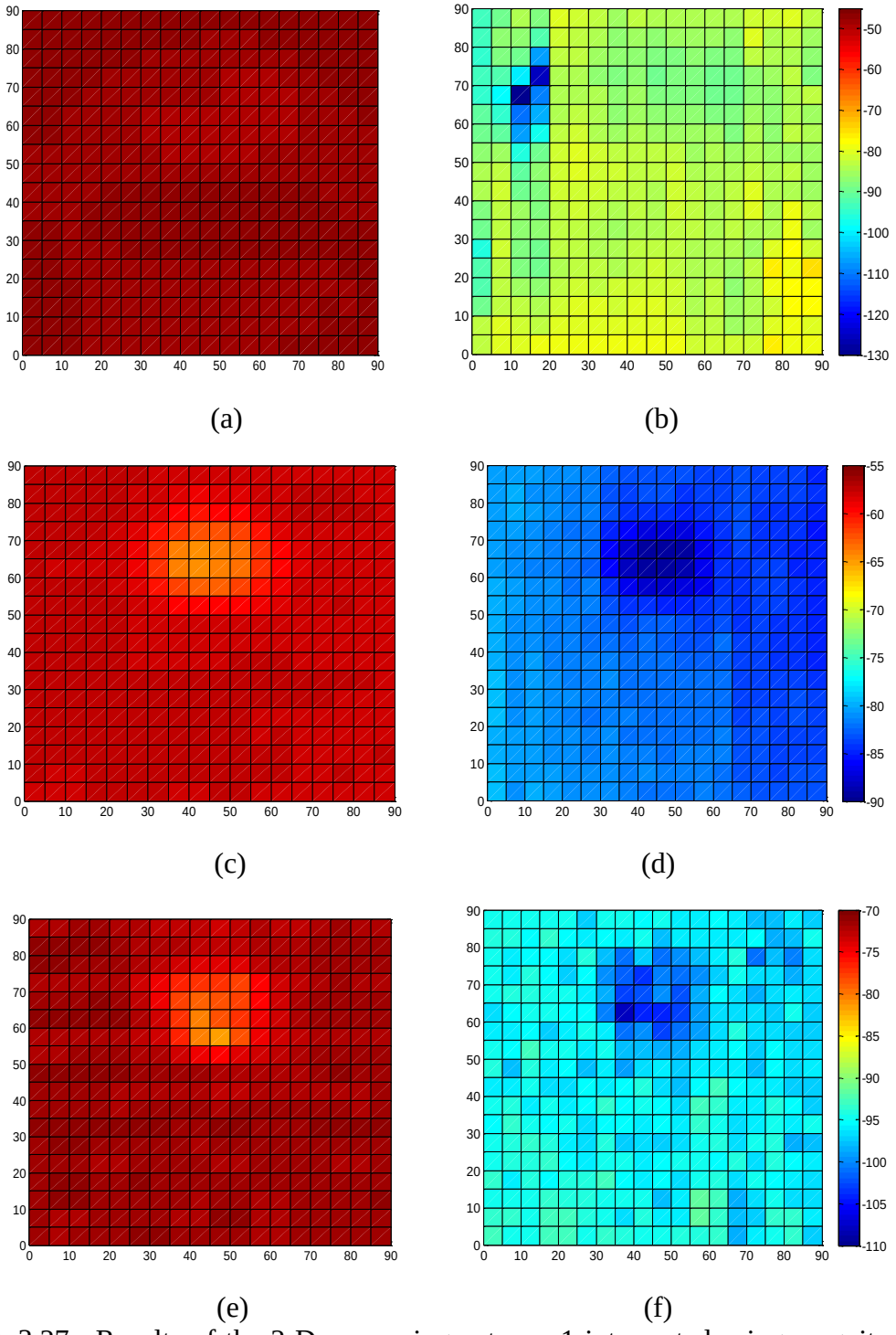

Fig. 3.27. Results of the 2-D scan using antenna 1 interpreted using magnitude-value evaluation. 2-D plot of averaged signal in dB at: (a) 3 GHz; (c) 6 GHz; (e) 10 GHz. 2-D plot of averaged uncertainty in dB at: (b) 3 GHz; (d) 6 GHz; (f) 10 GHz.

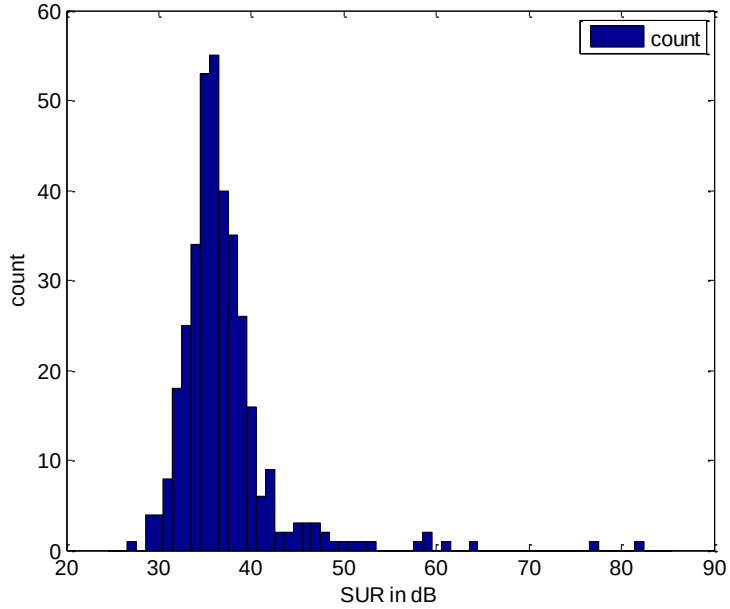
count
count
SUR in dB
0
10
20
30
40
50
60
20
30
40
50
60
70
80
90

(a)

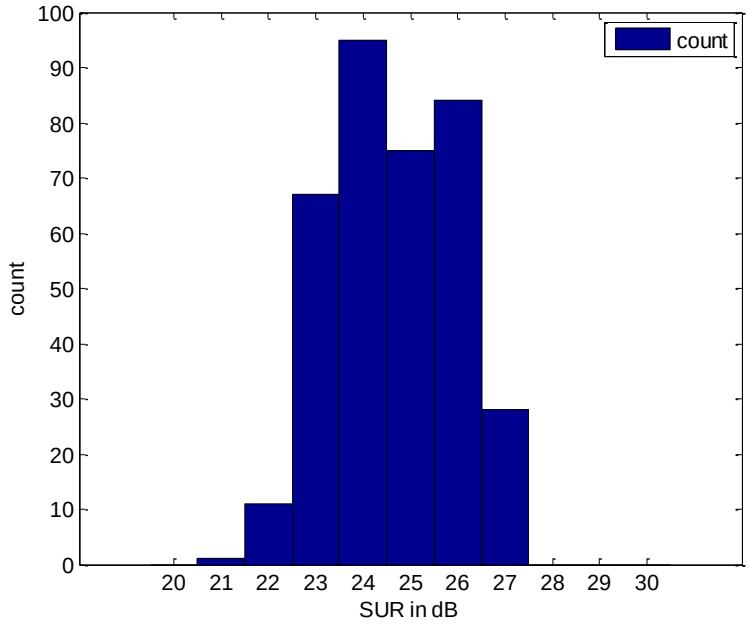
count
count
SUR in dB
0
10
20
30
40
50
60
70
80
90
100
20
21
22
23
24
25
26
27
28
29
30

(b)

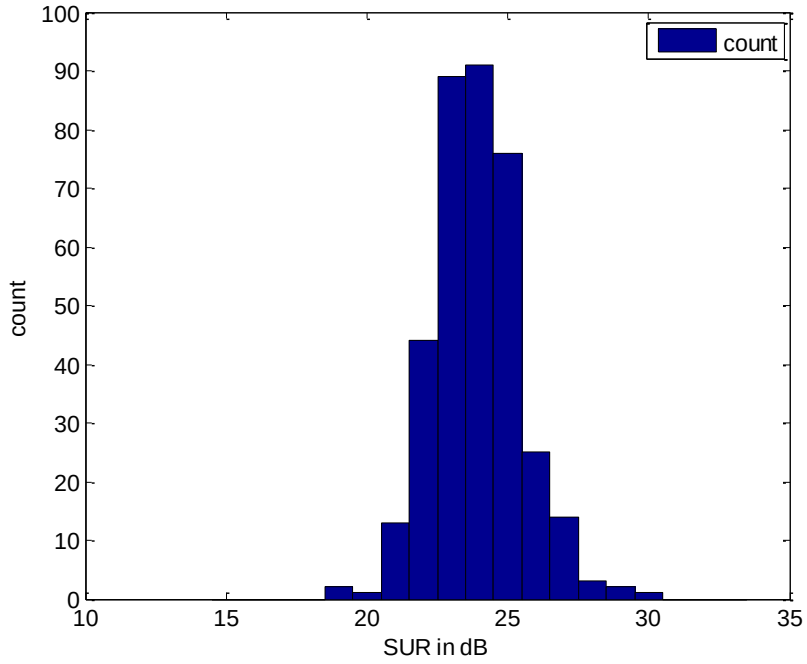

(c)

Fig. 3.28. Results of 2-D scan using antenna 1 interpreted using magnitude-value evaluation. Histogram of SUR distribution at: (a) 3 GHz; (b) 6 GHz; (c) 10 GHz.

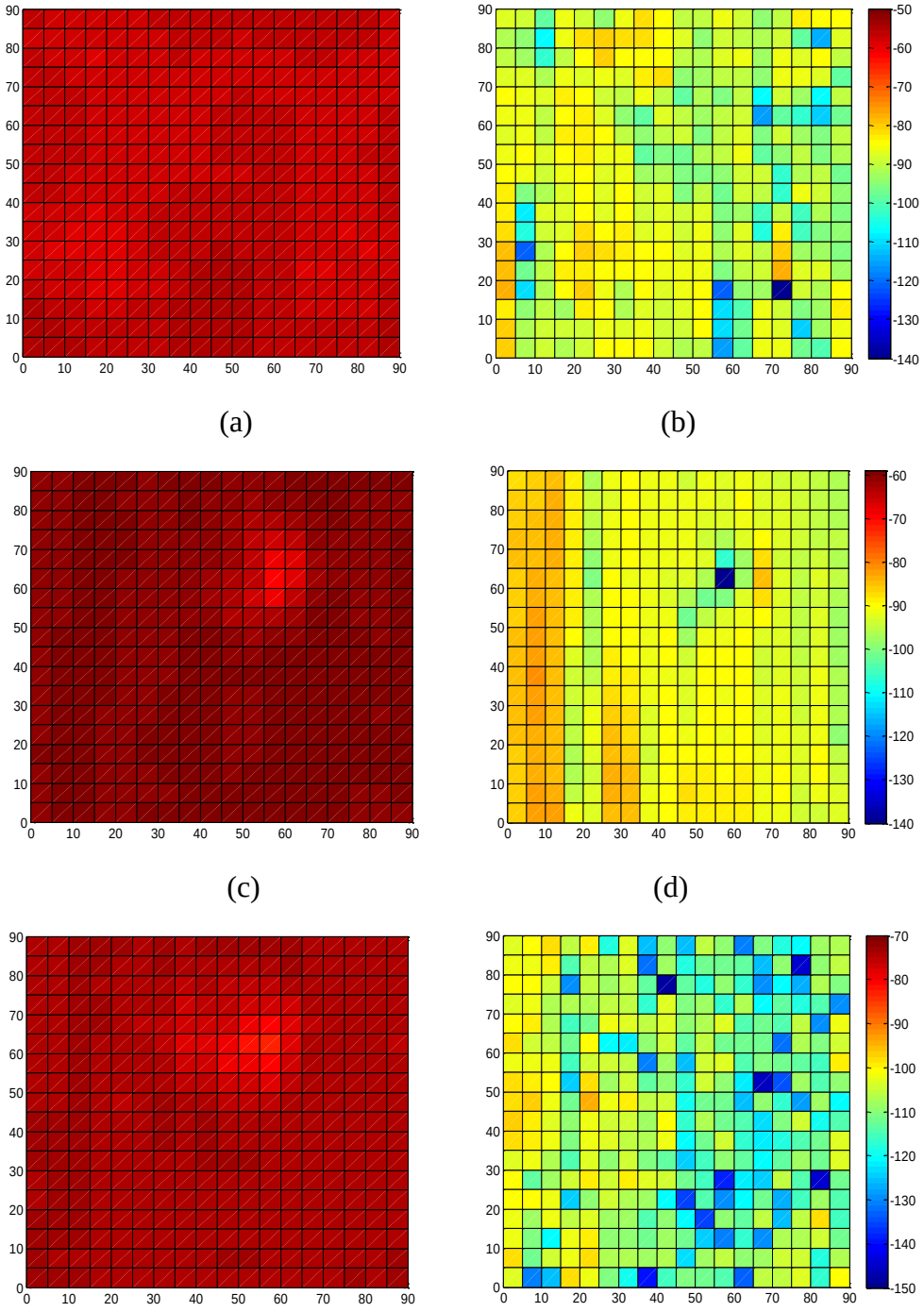

Fig. 3.29. Results of the 2-D scan using antenna 2 interpreted using magnitude-value evaluation. 2-D plot of averaged signal in dB at: (a) 3 GHz; (c) 6 GHz; (e) 10 GHz. 2-D plot of averaged uncertainty in dB at: (b) 3 GHz; (d) 6 GHz; (f) 10 GHz.

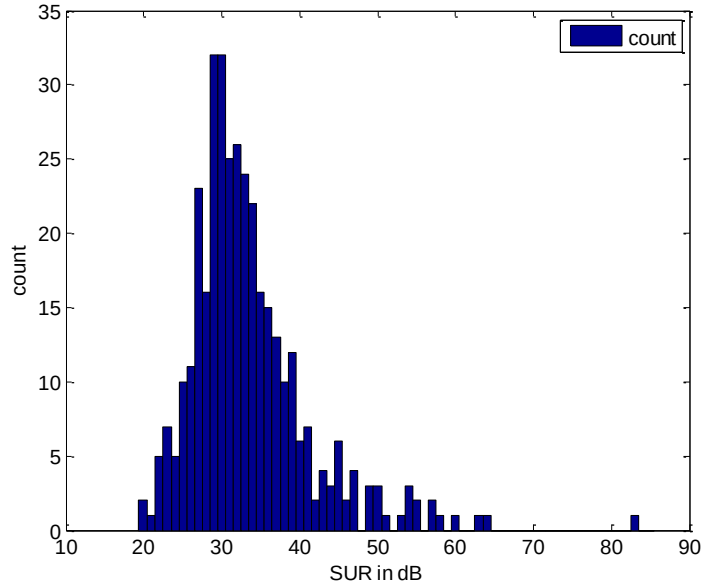
count
count
SUR in dB
0
5
10
15
20
25
30
35
10
20
30
40
50
60
70
80
90

(a)

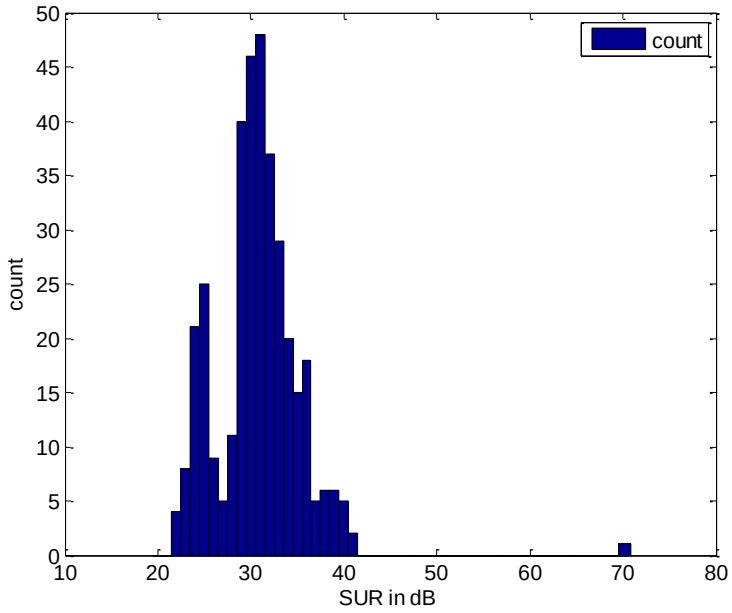
count
count
SUR in dB
0
5
10
15
20
25
30
35
40
45
50
10
20
30
40
50
60
70
80

(b)

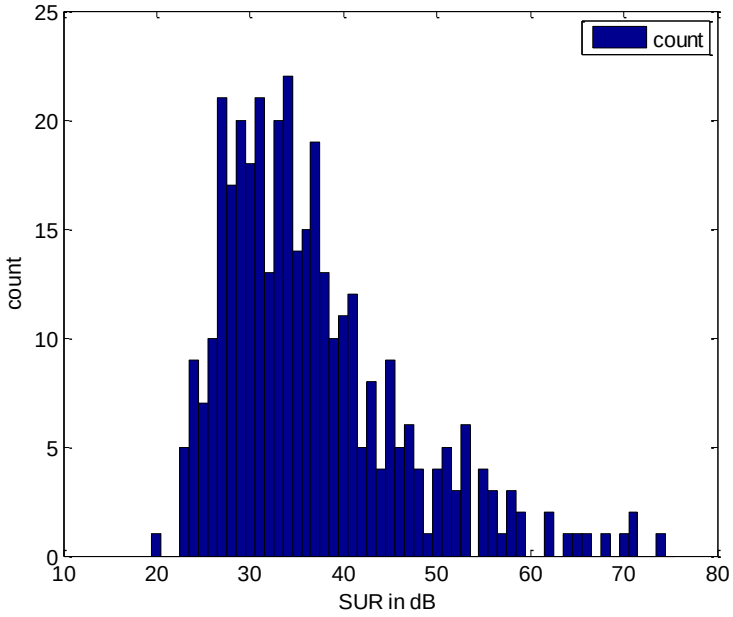

(c)

Fig. 3.30. Results of 2-D scan using antenna 2 interpreted using magnitude-value evaluation. Histogram of SUR distribution at: (a) 3 GHz; (b) 6 GHz; (c) 10 GHz.

Table 3.6. SUR average for both antennas for a 9×9 cm^2 scan calculated using magnitude information only

	SUR_{av}	
Frequency	**Antenna 1**	**Antenna 2**
3 GHz	37.1 dB	33.5 dB
6 GHz	24.6 dB	30.7 dB
10 GHz	23.9 dB	36.6 dB

The results for antenna 1 according to Fig. 3.27 and Fig. 3.28 are very close to the results obtained using complex-value evaluation. This is confirmed by the

slightly improved SUR average in Table 3.6. This is an indication that the phase information of antenna 1 is not "noisy".

On the other hand, according to Fig. 3.29, the results for antenna 2 show significant improvement in the uncertainty levels at all 3 sampling frequencies. This leads to higher SUR which can be seen by comparing the SUR histograms in Fig. 3.30 with the SUR histograms in Fig. 3.28. The SUR averages also show big improvements. In fact, based on magnitude information alone, the measurements with antenna 2 give much better SUR than the measurement with antenna 1. This indicates big uncertainty level in the phase information for the measurements with antenna 2.

3.4.3. Phase Only Evaluation

The phase only evaluation uses formulas (3.8) and (3.9). The data at three frequency points (3 GHz, 6 GHz and 10 GHz) are plotted. The results from the measurements with antenna 1 are shown in Fig. 3.31, and results from the measurements with antenna 2 are shown in Fig. 3.32.

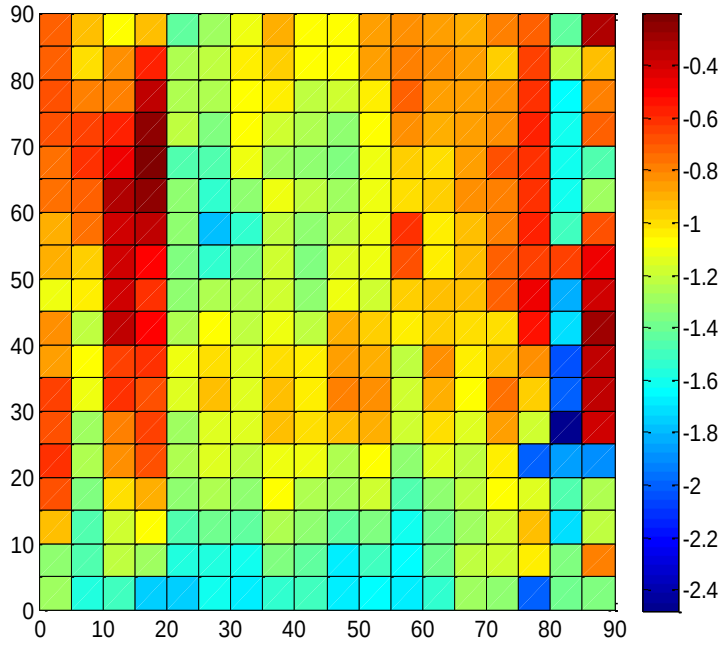
90
80
70
60
50
40
30
20
10
0
0 10 20 30 40 50 60 70 80 90
-0.4
-0.6
-0.8
-1
-1.2
-1.4
-1.6
-1.8
-2
-2.2
-2.4

(a)

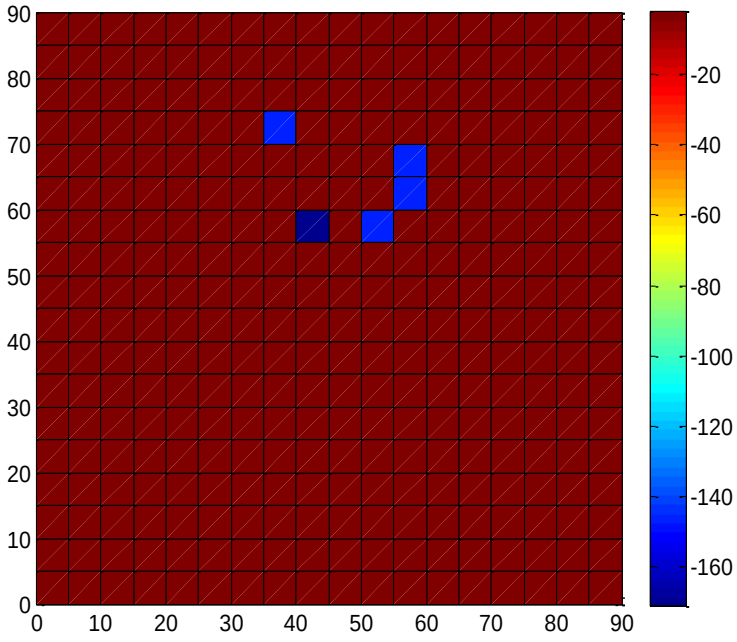
90
80
70
60
50
40
30
20
10
0
0 10 20 30 40 50 60 70 80 90
-20
-40
-60
-80
-100
-120
-140
-160

(b)

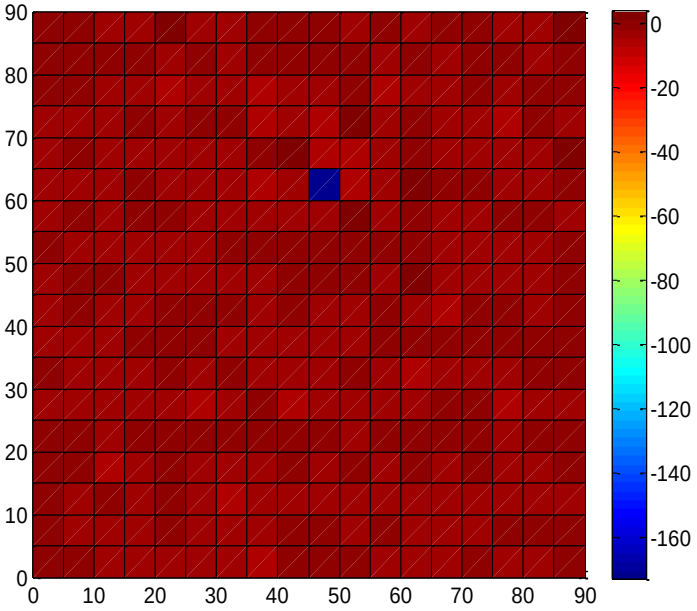

(c)

Fig. 3.31. Results of 2-D scan using antenna 1 interpreted using phase-only. 2-D plot of averaged phase uncertainty in degrees at: (a) 3 GHz; (b) 6 GHz; (c) 10 GHz.

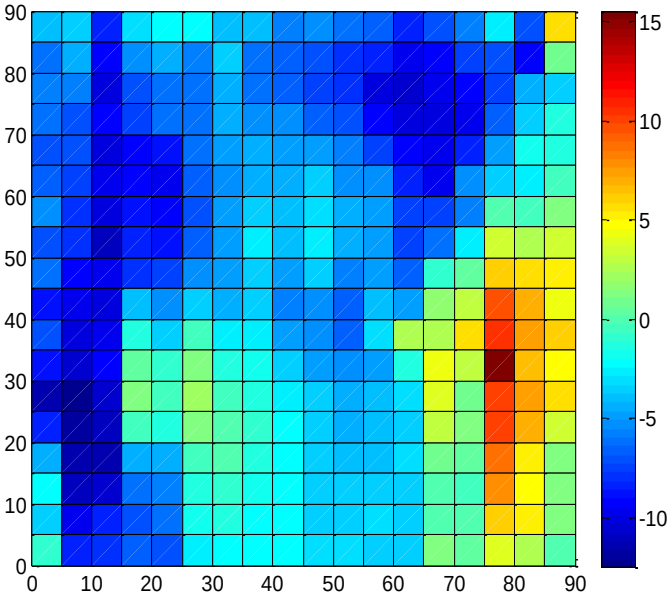

(a)

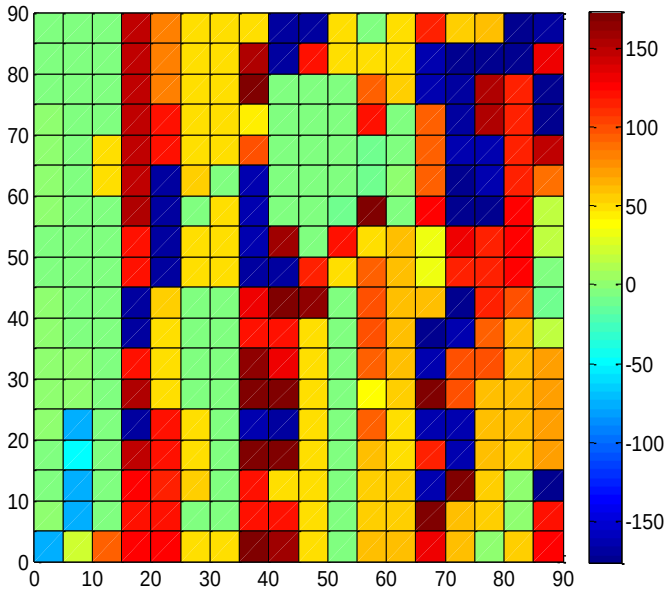

(b)

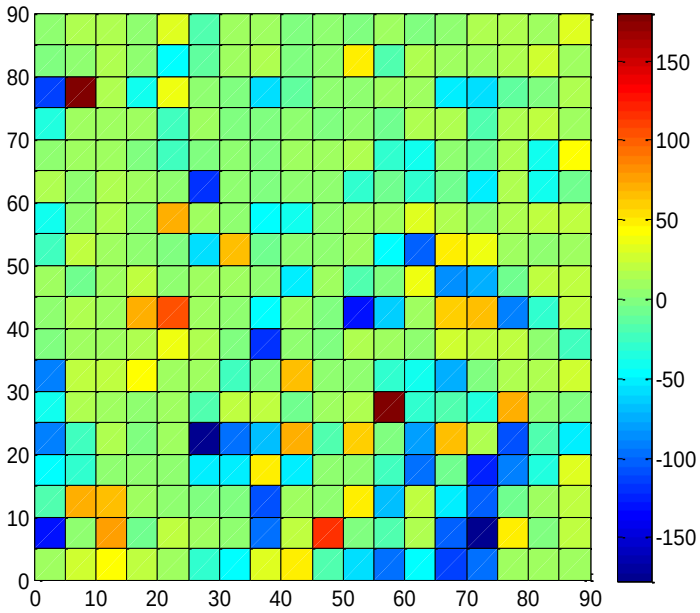

(c)

Fig. 3.32. Results of 2-D scan using antenna 2 interpreted using phase-only. 2-D plot of averaged phase uncertainty in degrees at: (a) 3 GHz; (b) 6 GHz; (c) 10 GHz.

Based on Fig. 3.31, the phase uncertainty of the measurement data with antenna 1 is small. There are several points showing large uncertainty levels in the plots at 6 GHz and 10 GHz, which are regarded as outliers.

In the measurement data with antenna 2, the phase uncertainties are significant, especially in the 6 GHz and 10 GHz plots. These are the cause of the poor SUR values when evaluating with complex value method.

In summary, this section presents a study of the overall uncertainty level of the developed imaging system. The obtained measurement data incorporate all effects from each source of uncertainties. The measurement data with antenna 1 show high SUR value in all three sampling frequencies, which means better performance as compared to antenna 2. The poorer performance of antenna 2 is a result of big phase uncertainty, which is also observed while studying the uncertainties associated with vertical motion (section 3.3.1).

3.5. Effects of Repeated Measurements

After the studies on different evaluation methods above, it is also interesting to know the effects of the repeated measurements on the signal to uncertainty ratio of the imaging system. To study the effect, we use one example. The data are taken from measurement scenario described in section 3.4. Based on these 10 sets of measurement data, we calculated and recorded the SUR_{av} for different number of sets of measurement, i.e., from 2 sets of measurement to 10 sets of measurement. The results are plotted in Fig. 3.33. Based on the plot, the SUR_{av} variations are small, and the results for all 3 sampling frequencies tend to

converge to certain number, but in order to obtain this number, more than 10 sets of measurements are needed.

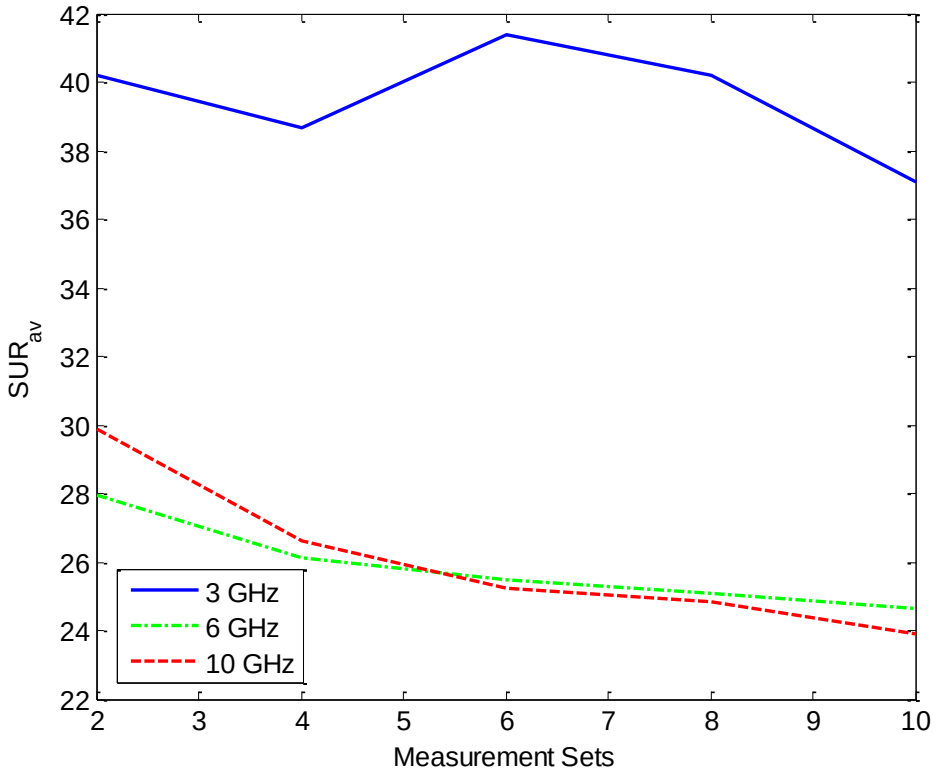

Fig. 3.33. Effects of repeated measurements on SUR. Measurements on target phantom with antenna 1 using magnitude information only.

3.6. Conclusion

This chapter is a comprehensive study of the dynamic range of the developed raster-scanning imaging system. Each source of uncertainties is identified and studied. Based on the measurement data, the planar raster-scanning imaging system (when connected with antenna 1) is robust against noise and the data collected are reliable. The thickest phantom used in the measurements for this chapter is 4.5 cm. For such phantoms, the signal levels are much higher than the uncertainty levels. For future experiments, when the phantoms are thicker or lossier, signal levels may fall below the uncertainty level of the system. In these cases, LNAs should be used to improve the performance of the system. Further work is also needed to reduce the uncertainties in the measurements associated with the vertical and lateral motions of the scanning table.

References

[1] *Advantest: R3860A/3770R3768 Operation Manual,* Manual FOE-8440128F01, Advantest Corporation, Aug. 2003.

[2] M. Hiebel, *Fundamentals of Vector Network Analysi.* Munchen, Germany: Rohde & Schwarz, 2005, pp. 84-85.

[3] D. Pozar, *Microwave Engineering.* 2nd ed., Canada: John Wiley & Sons, 1998, pp. 555-559.

[4] H.A. Haus *et al*., "Description of the Noise Performance of Amplifiers and Receiving Systems," Sponsored by IRE subcommittee 7.9 on Noise, *Proc. of the IEEE,* vol. 51, no. 3, pp. 436-442, March,1963.

[5] *Agilent: Fundamentals of RF and microwave noise figure measurements,* Application Note 57-1, Agilent Technologies, [Online]. http://cp.literature.agilent.com/litweb/pdf/5952-8255E.pdf

CHAPTER 4

PERFORMANCE AND LIMITATIONS OF THE TWO-ANTENNA SCANNING SETUP

Introduction

Many measurements were performed using both two sets of antennas on the developed raster-scanning imaging system since it was built. This chapter focuses on presenting some of the results obtained with the imaging system which showcase its performance as well as its limitations.

4.1 Antenna Performance

There are two sets of imaging antennas available to use with the raster-scanning setup. They are shown in Fig. 4.1.

With all other components the same, the performance of the raster-scanning system is determined by the performance of the antennas used. It is instructive to study the performance of both antennas and compare it with the simulation results.

Fig. 4.1. Photo of the two imaging antennas used in the raster-scanning setup.

4.1.1 S_{11} Measurement

The first scenario measures the return loss, or S_{11}, for each type of the antennas. With each antenna measurement, two antennas of the same type are connected to port 1 and port 2 of the VNA, respectively. The apertures of the antennas are in touch with the plexiglass plate. The VNA sweeps from 3 GHz to 10 GHz with 201 sampling points and the S_{11} magnitude in dB are recorded. These data are then plotted using Matlab [1] along with the simulation results obtained from HFSS [2]. For both types of antennas, two sets of simulations are done. Simulation 1 represents the scenario when two antennas are aligned along each other's boresight with their apertures touching. Simulation 2 represents the excitation of a standalone antenna in air.

Fig. 4.2 shows the S_{11} plot of antenna 1 for both measured and simulated results. All three results show good impedance match over the ultra-wide band. The measured data even demonstrate better performance at mid frequency, i.e., from 5 GHz to 7 GHz.

Fig. 4.3 shows the S_{11} plot of antenna 2 for both measured and simulated results. According to the results, antenna 2 has better performance when the loading is air.

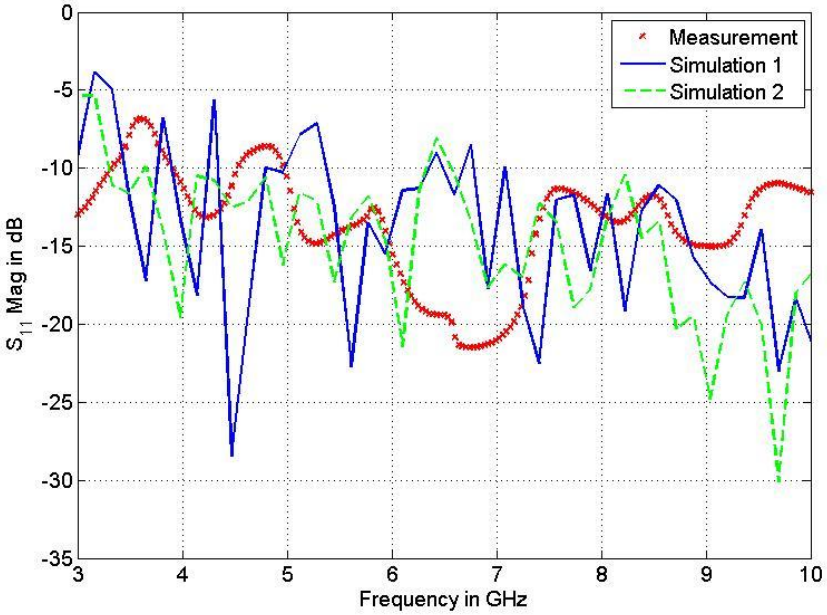

Fig. 4.2. Measured and simulated S_{11} magnitude from 3 GHz to 10 GHz for antenna 1.

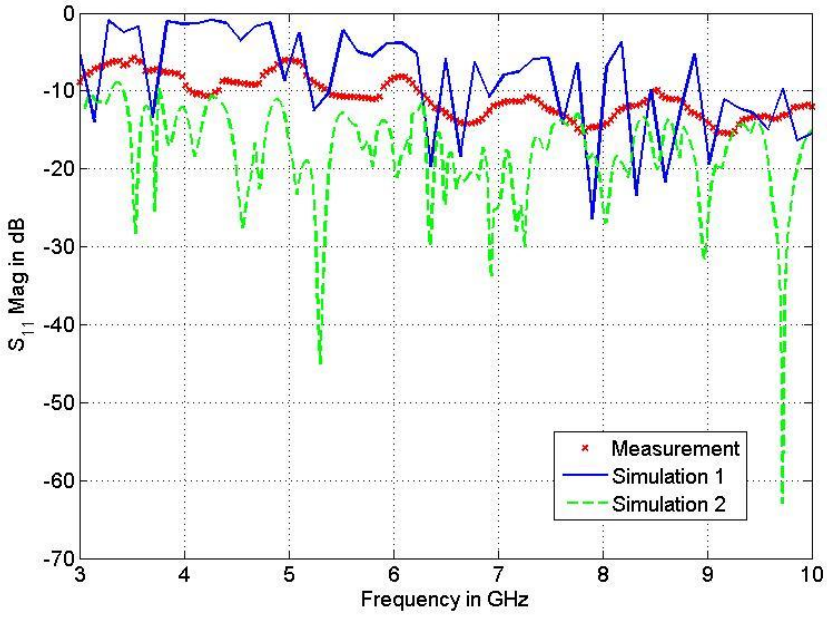

Fig. 4.3. Measured and simulated S_{11} magnitude from 3 GHz to 10 GHz for antenna 2.

4.1.2 S_{21} Measurement

Insertion loss, or S_{21}, is a measure of the coupling efficiency between the two antennas. In this measurement, two antennas are connected to port 1 and port 2 of the VNA, respectively. They are then aligned along each other's boresight with their apertures touching. Copper tape is then used to shield off the gap between the two antennas. In this configuration, maximum coupling efficiency between the two antennas is measured. Fig. 4.4 shows the configuration with antenna 1 and Fig. 4.5 shows the configuration with antenna 2. The VNA is set to sweep from 3 GHz to 10 GHz with 201 frequency sampling points. The S_{21} magnitude is recorded. Simulations of this scenario are performed for both sets of antennas and compared with the measurement.

Fig. 4.6 shows both simulation and the measurement results for antenna 1. We observe that the measured S_{21} is slightly lower than the simulation results in the low-mid frequency, i.e., from 3 GHz to 8 GHz. The measured S_{21} shows a big drop in signal strength beyond 8 GHz.

Fig. 4.7 shows the simulated and measured results for antenna 2. The measured data are much weaker than the simulation results. The greater measured loss in antenna 2 as compared to its simulated loss may be due to poor contacts inside the horn. In the measured data, antenna 1 shows better coupling efficiency.

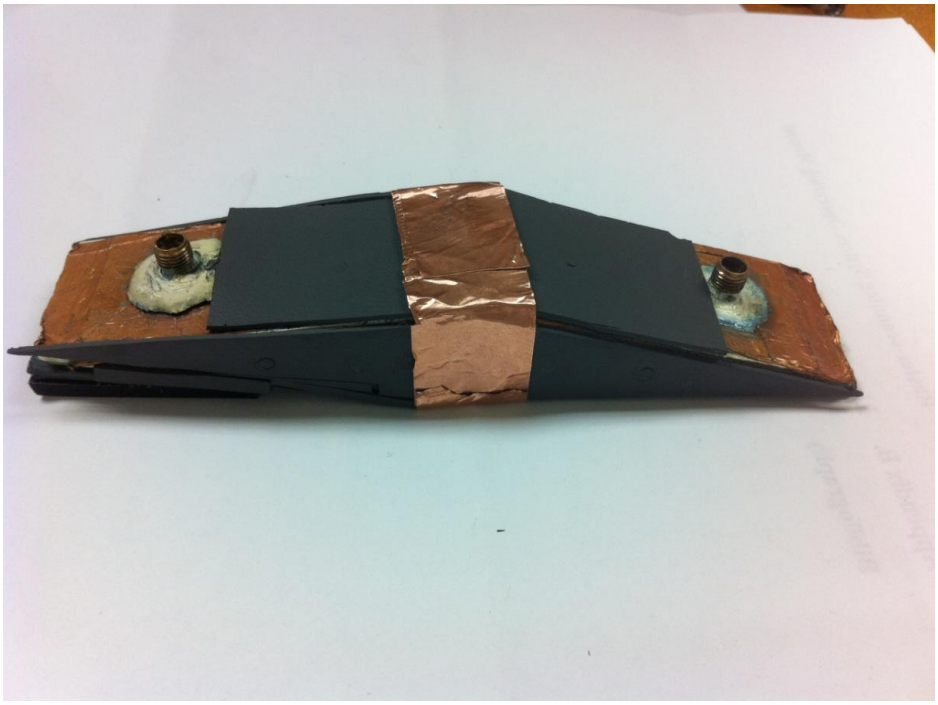

Fig. 4.4. Configuration with antenna 1 for measuring the maximum coupling efficiency.

Fig. 4.5. Configuration with antenna 2 for measuring the maximum coupling efficiency.

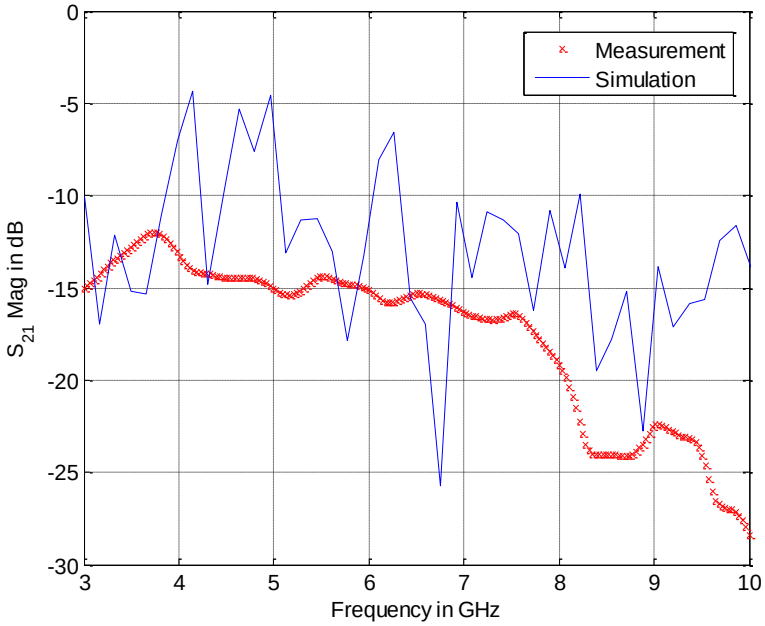

Fig. 4.6. Measured and simulated S_{21} magnitude from 3 GHz to 10 GHz for antenna 1.

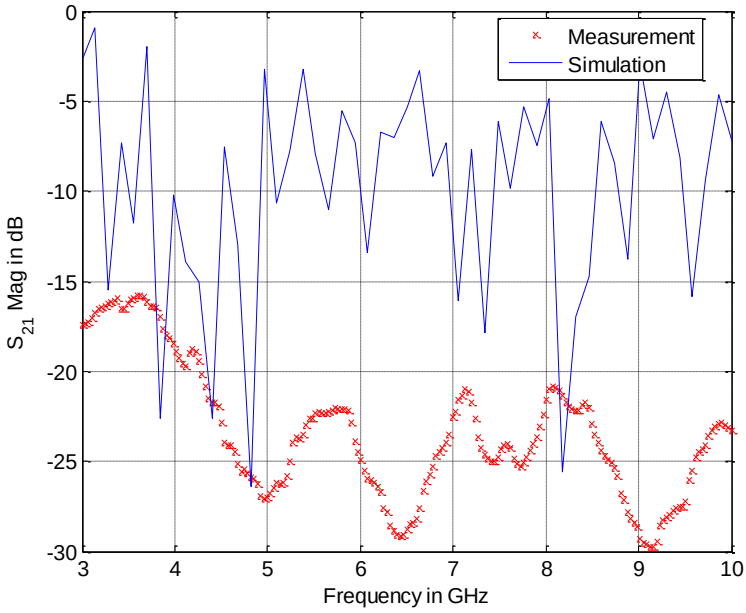

Fig. 4.7. Measured and simulated S_{21} magnitude from 3 GHz to 10 GHz for antenna 2.

4.2 Results of Typical Imaging Measurements

In this section, results of phantom measurements are presented. The first set of measurements is the raster scan of a target phantom, i.e., phantom with embedded tumor simulant, with both two sets of antennas. The acquired data (S_{21}) are then evaluated using three different methods: complex-value evaluation, magnitude-only evaluation and phase-only evaluation. For the second set, raster scans are done on two background phantoms, i.e., phantoms without a tumor simulant. The same three sets of evaluation methods are applied to the acquired data.

4.2.1. Imaging of a Target Phantom

The target phantom is a phantom with homogeneous background but with a tumor simulant embedded in the centre. Due to the contrast in the dielectric properties between the phantom background and the tumor simulant, the signature of the embedded tumor should be picked up from the data acquired by the raster scan.

The target phantom used in this scenario is 18 cm by 18 cm wide and 4.5 cm thick. The phantom background is low-water-content (low-loss) and the tumor simulant exhibits significant contrast (more than 3 times in permittivity and conductivity). The dielectric properties of the phantom are attached in Appendix C.

The raster scan is performed with two antennas over a 9 cm by 9 cm area which is centered at the centre of the phantom. 10 scans are performed and averaged data are used for evaluations.

1) Complex Value Evaluation

Complex-value evaluation uses the measured S_{21} in complex form. These are formulas (3.2), (3.4) and (3.5) in Chapter 3. Three sampling frequencies, 3 GHz, 6 GHz and 10 GHz are chosen for the pseudocolor plot of the averaged S_{21} magnitude and the SUR.

Antenna 1

Figs. 4.8 to 4.10 show the 2-D plot of the averaged S_{21} and the SUR when two prototypes of antenna 1 are used to scan a 9 cm by 9 cm square on the target phantom at 3 GHz, 6 GHz and 10 GHz.

At 6 GHz and 10 GHz, the tumor signature is very obvious. At 3 GHz, the tumor can be vaguely identified. This is due to the fact that the difference between the tumor signature and the background is only 2 to 3 dB. On the other hand, at 6 GHz, the tumor signature exhibits about 7 dB difference to the background. At 10 GHz, the difference is around 10 dB. Also, the plots show that the position of the tumor has drifted from the centre. This might due to the drift of the tumor simulant in the phantom during fabrication.

These results are expected since low-frequency microwaves have better penetration depth. At low frequencies, the received signal is strong and the SUR is high. But the microwaves do not travel along simple straight paths and it is hard

to identify the tumor signature. At mid-high frequencies on the other hand, the SUR is lower, but the sensors are more sensitive, thus picking up obvious tumor signature in the S_{21} plots.

Antenna 2

Figs. 4.11 to 4.13 show the 2-D plot of the averaged S_{21} and the SUR when two prototypes of antenna 2 are used to scan a 9 cm by 9 cm square on the target phantom at 3 GHz, 6 GHz and 10 GHz. The calculation uses complex values.

At 3 GHz, the SUR is high but the S_{21} exhibits no sign of tumor signature. At 6 GHz, the tumor signature is obvious and it exhibits about 8 dB difference to the background. At 10 GHz, the tumor signature is obvious, but there are also some artifacts in the plot. Additionally, the SUR at the position of the tumor simulant is below 0, indicating that the signal strength is too weak. Note that the position of the tumor on these plots has also drifted from the centre. This is in good agreement with the results obtained using antennas 1.

Based on these results, antenna 1 has better performance over antenna 2 in picking up tumor signatures. Also, both antennas seem to be most sensitive in the frequency range around 6 GHz to 7 GHz.

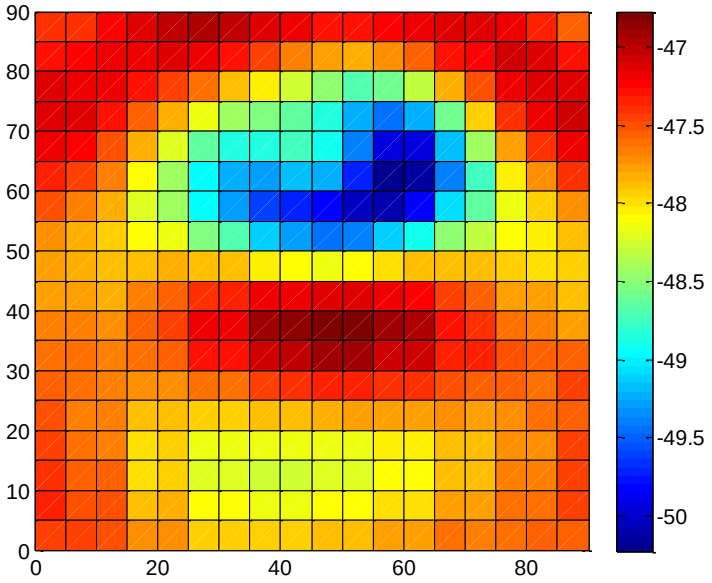

(a)

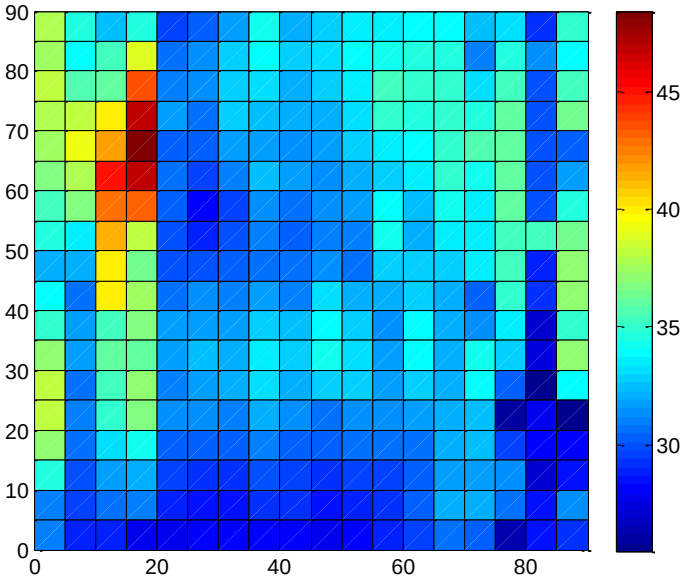

(b)

Fig. 4.8. 2-D plot of scan results with antennas of type 1 over a 9 cm by 9 cm square on the target phantom at 3 GHz calculated using complex values: (a) magnitude of the averaged S_{21} and (b) SUR.

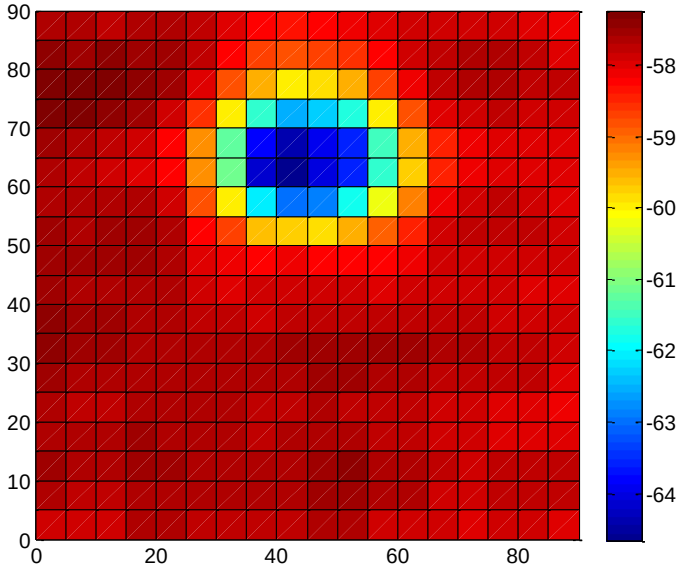

(a)

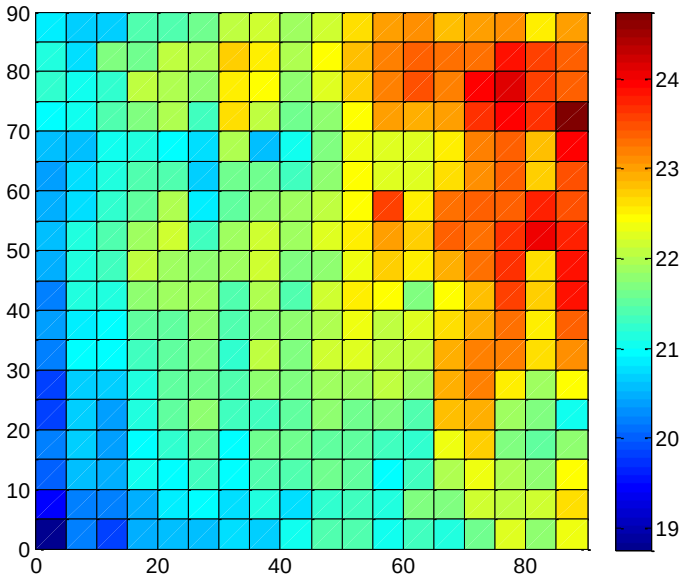

(b)

Fig. 4.9. 2-D plot of scan results with antennas of type 1 over a 9 cm by 9 cm square on the target phantom at 6 GHz calculated using complex values: (a) magnitude of the averaged S_{21} and (b) SUR.

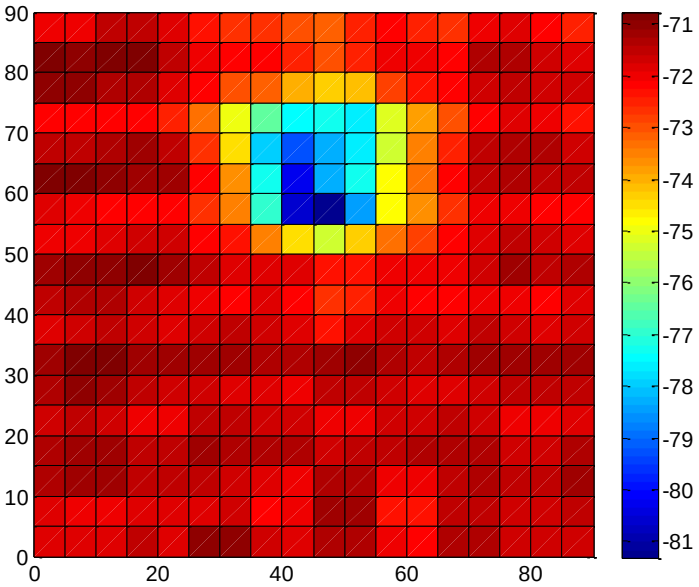

(a)

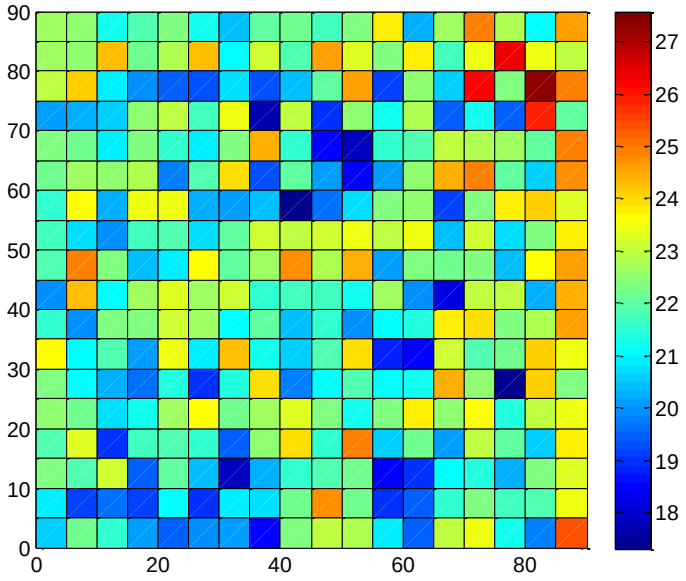

(b)

Fig. 4.10. 2-D plot of scan results with antennas of type 1 over a 9 cm by 9 cm square on the target phantom at 10 GHz calculated using complex values: (a) magnitude of the averaged S_{21} and (b) SUR.

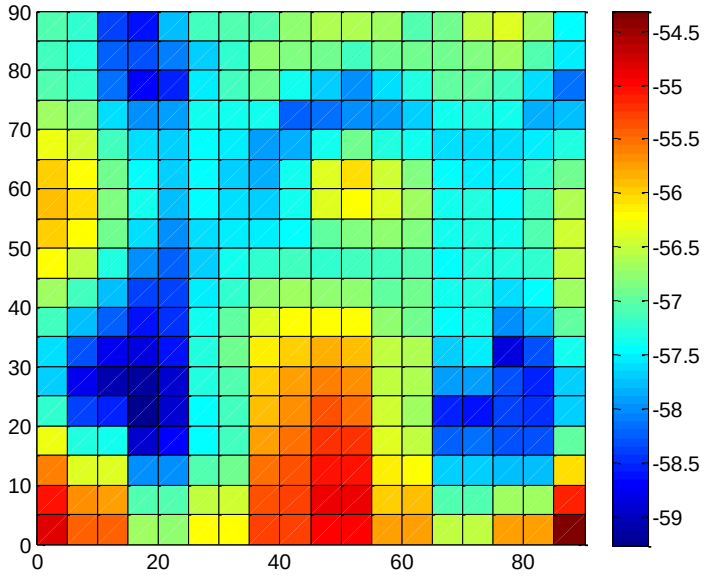

(a)

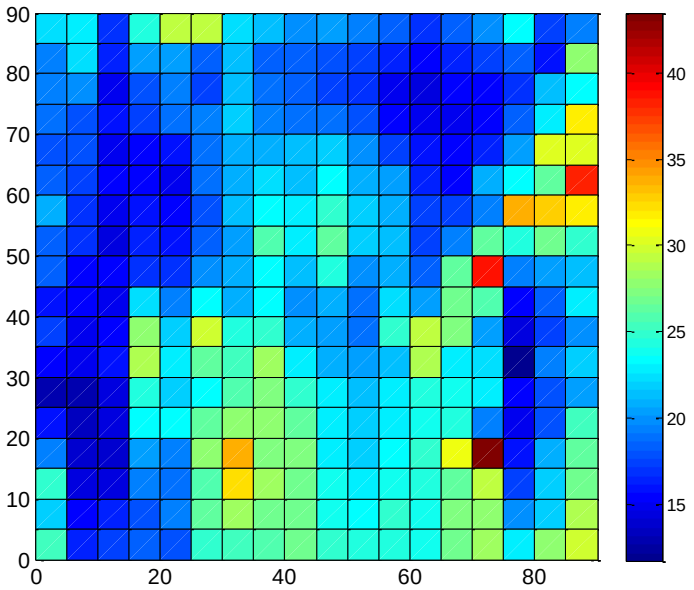

(b)

Fig. 4.11. 2-D plot of scan results with antennas of type 2 over a 9 cm by 9 cm square on the target phantom at 3 GHz calculated using complex values: (a) magnitude of the averaged S_{21} and (b) SUR.

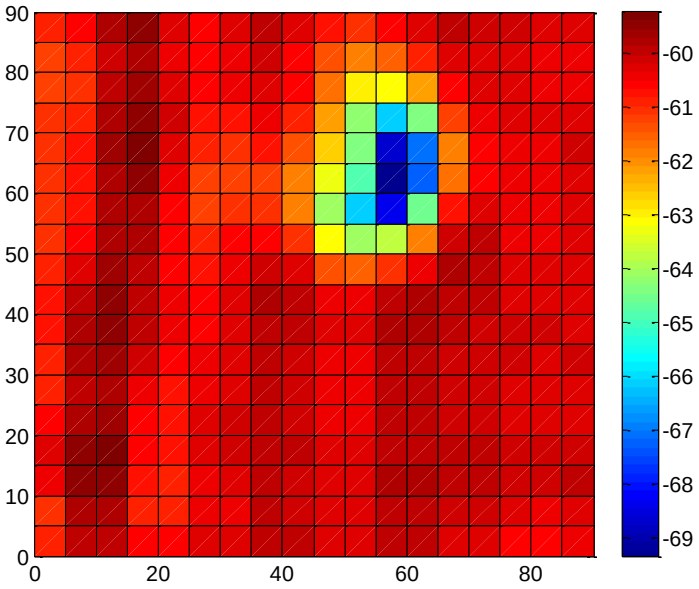

(a)

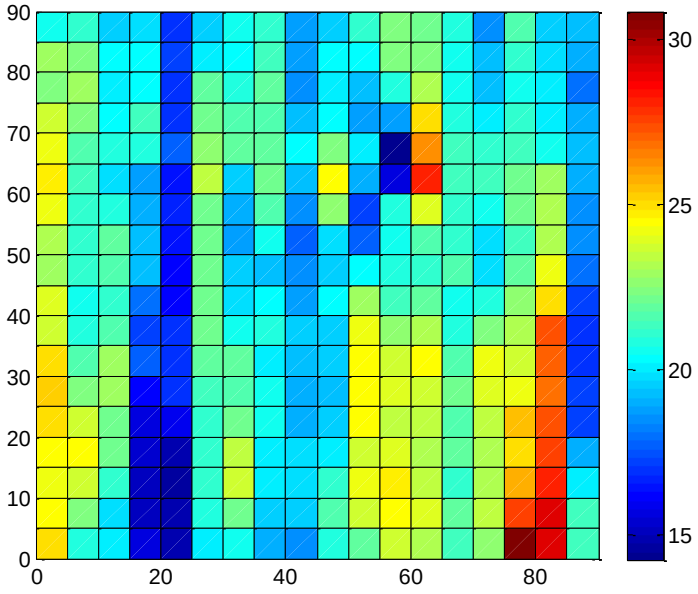

(b)

Fig. 4.12. 2-D plot of scan results with antennas of type 2 over a 9 cm by 9 cm square on the target phantom at 6 GHz calculated using complex values: (a) magnitude of the averaged S_{21} and (b) SUR.

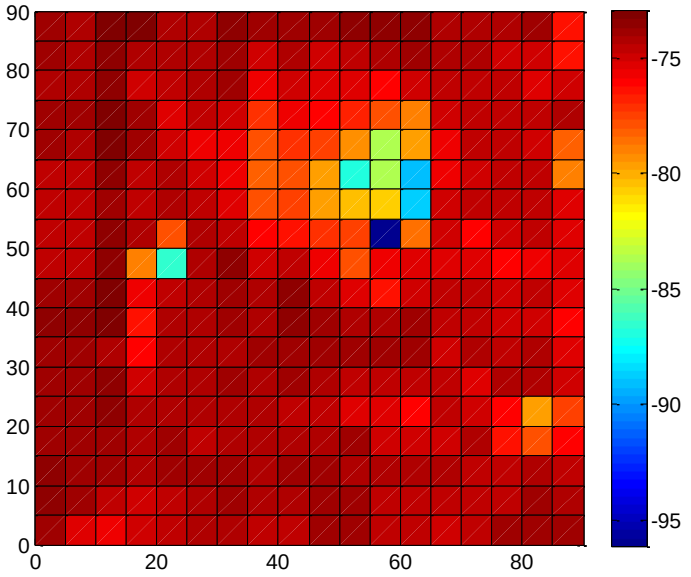

(a)

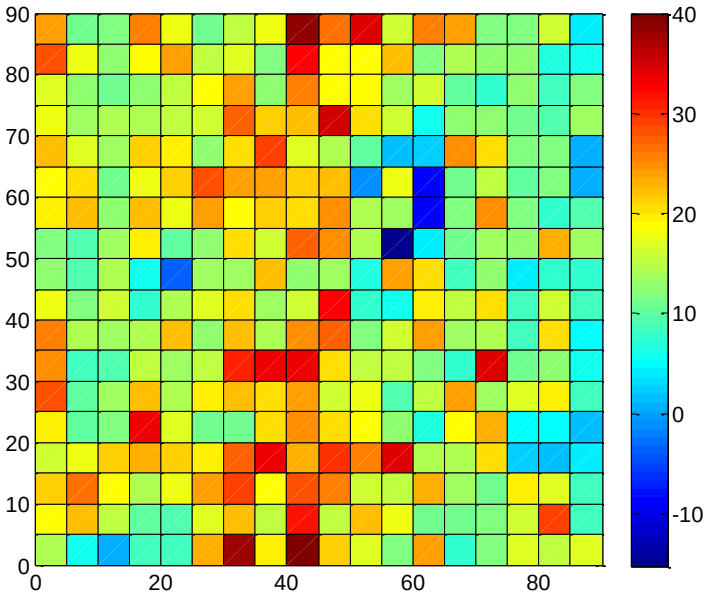

(b)

Fig. 4.13. 2-D plot of scan results with antennas of type 2 over a 9 cm by 9 cm square on the target phantom at 10 GHz calculated using complex values: (a) magnitude of the averaged S_{21} and (b) SUR.

2) Magnitude Only Evaluation

Magnitude-only evaluation uses the measured S_{21} magnitude only. These are formulas (3.6), (3.7) and (3.5) in Chapter 3. Three sampling frequencies, 3 GHz, 6 GHz and 10 GHz are chosen for the pseudocolor plot of the averaged S_{21} magnitude and the SUR.

Antenna 1

Figs. 4.14 to 4.16 show the 2-D plot of averaged S_{21} and the SUR when antennas 1 are used to scan a 9 cm by 9 cm square on the target phantom at 3 GHz, 6 GHz and 10 GHz. The averaged S_{21} signal plots in all 3 frequencies are visually very similar to the plots generated using complex values. The SUR on the other hand is slightly better.

Antenna 2

Figs. 4.17 to 4.19 show the same results when antennas 2 are used as sensors. The averaged S_{21} signal plots of 3 GHz and 6 GHz are similar to the plots generated using complex values. The plot at 10 GHz is better and is free of artifacts. All three SUR plots also show better values. Furthermore, the SUR plot at 10 GHz shows no negative value. This improvement indicates the presence of phase error in the measured data with antennas 2.

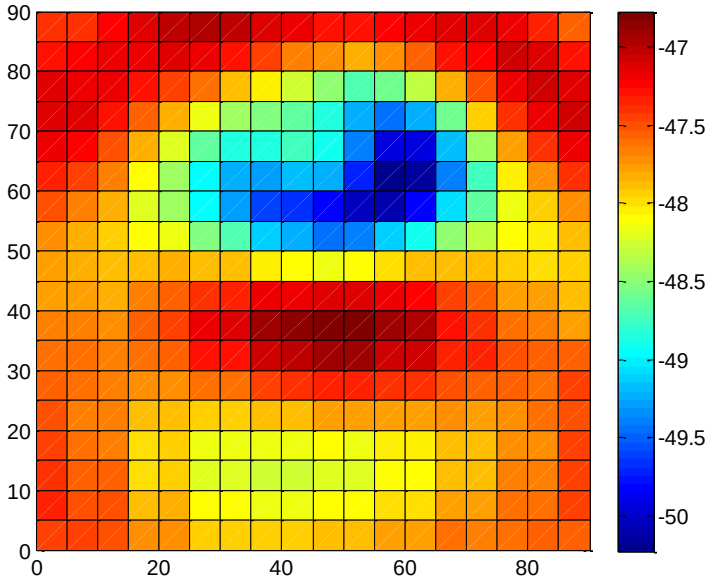

(a)

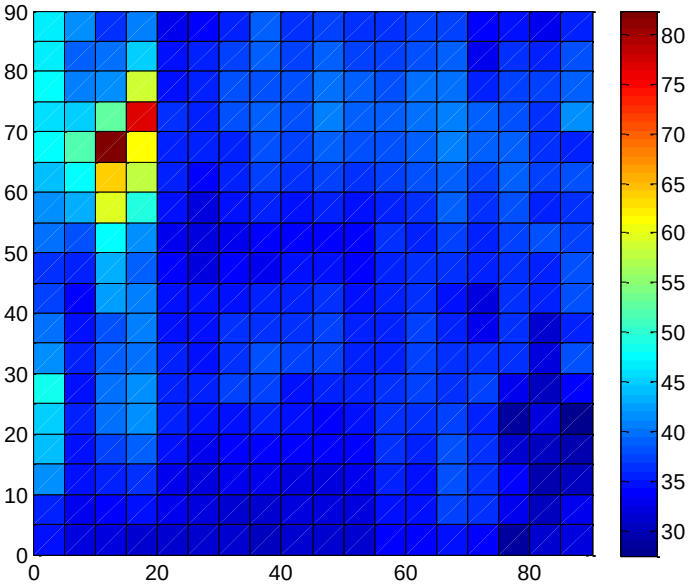

(b)

Fig. 4.14. 2-D plot of scan results with antennas of type 1 over a 9 cm by 9 cm square on the target phantom at 3 GHz calculated using magnitude only: (a) magnitude of the averaged S_{21} and (b) SUR.

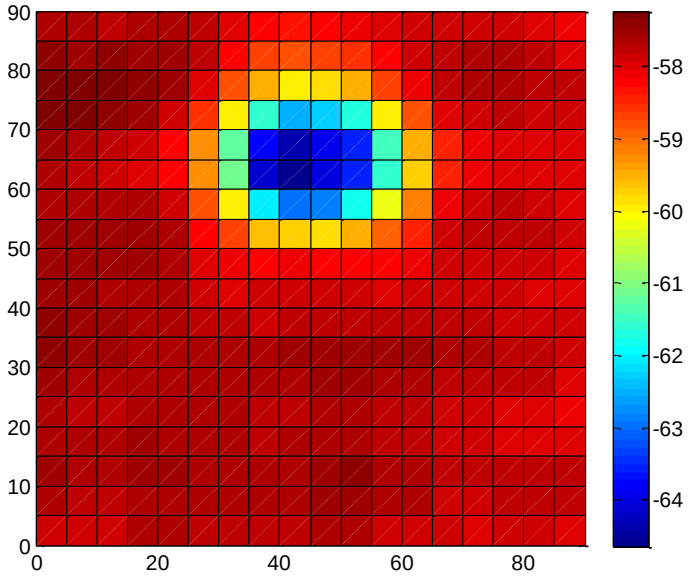

(a)

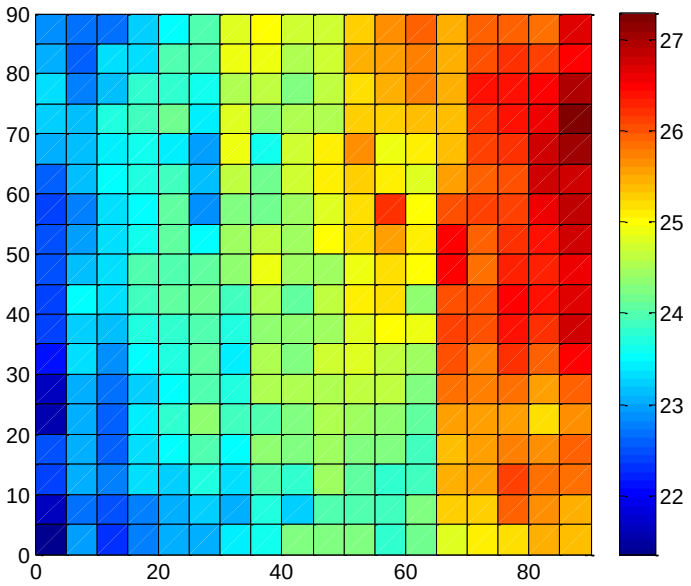

(b)

Fig. 4.15. 2-D plot of scan results with antennas of type 1 over a 9 cm by 9 cm square on the target phantom at 6 GHz calculated using magnitude only: (a) magnitude of the averaged S_{21} and (b) SUR.

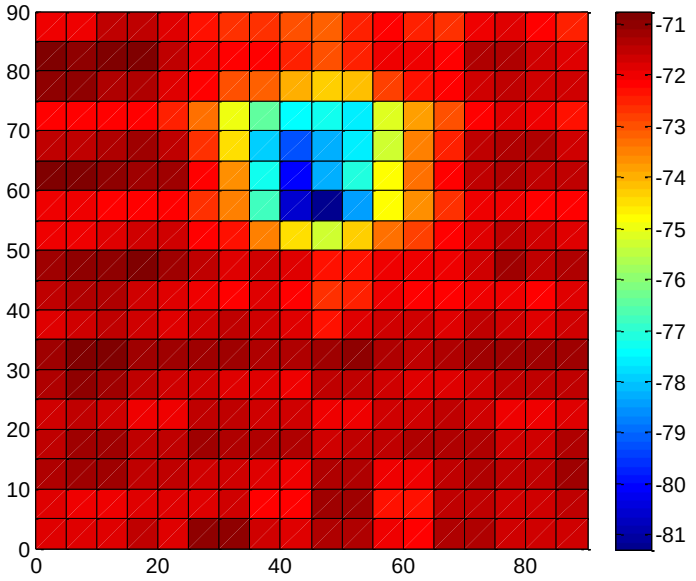

(a)

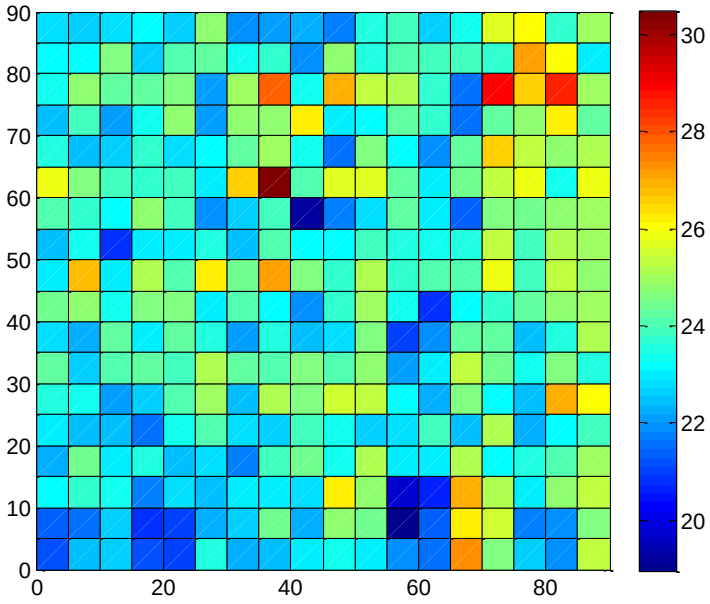

(b)

Fig. 4.16. 2-D plot of scan results with antennas of type 1 over a 9 cm by 9 cm square on the target phantom at 10 GHz calculated using magnitude only: (a) magnitude of the averaged S_{21} and (b) SUR.

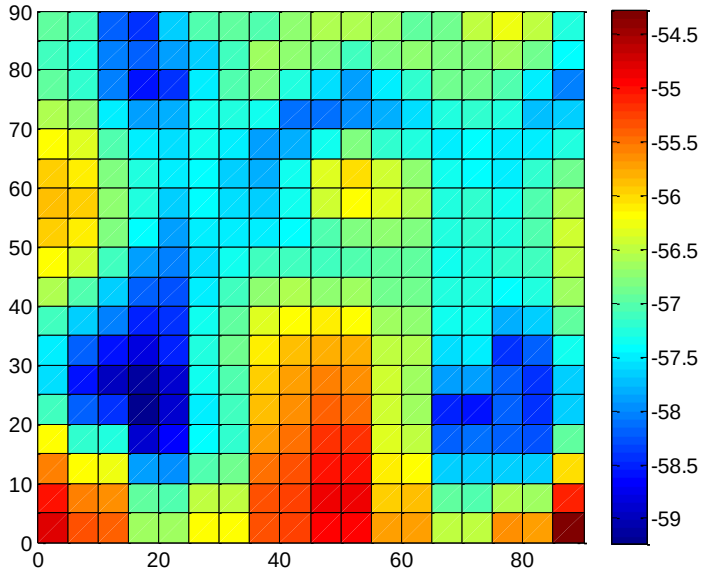

(a)

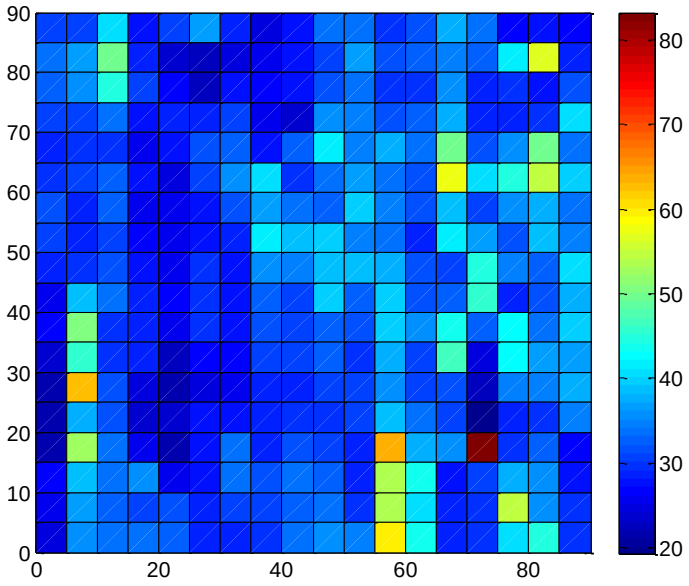

(b)

Fig. 4.17. 2-D plot of scan results with antennas of type 2 over a 9 cm by 9 cm square on the target phantom at 3 GHz calculated using magnitude only: (a) magnitude of the averaged S_{21} and (b) SUR.

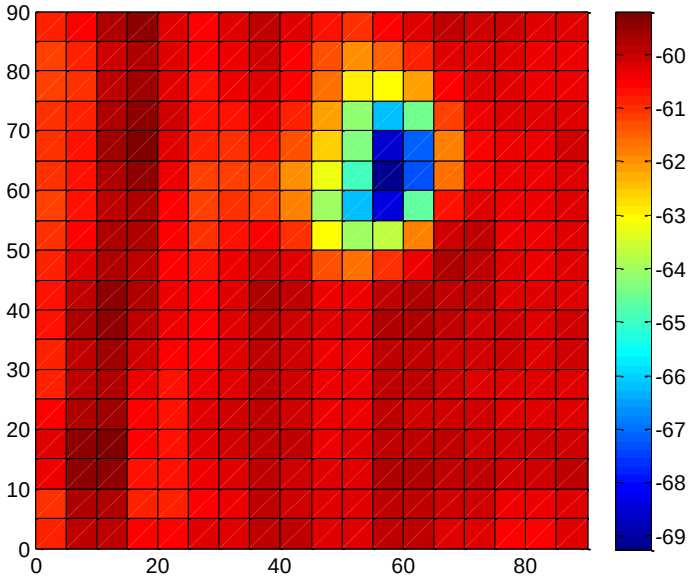

(a)

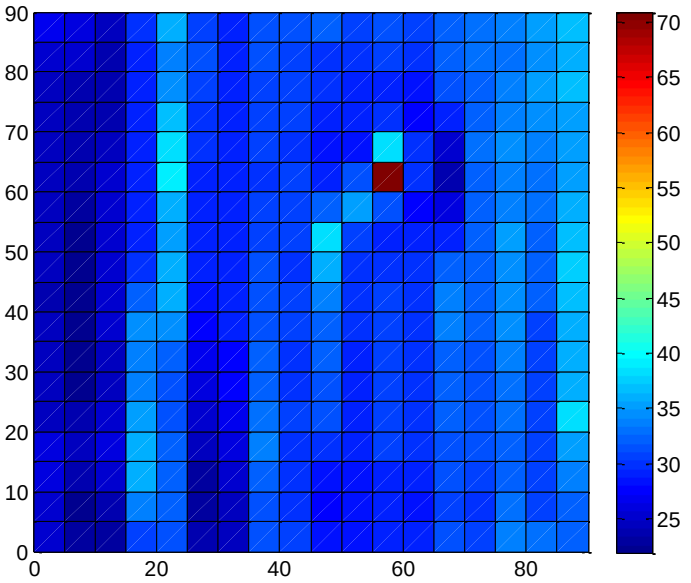

(b)

Fig. 4.18. 2-D plot of scan results with antennas of type 2 over a 9 cm by 9 cm square on the target phantom at 6 GHz calculated using magnitude only: (a) magnitude of the averaged S_{21} and (b) SUR.

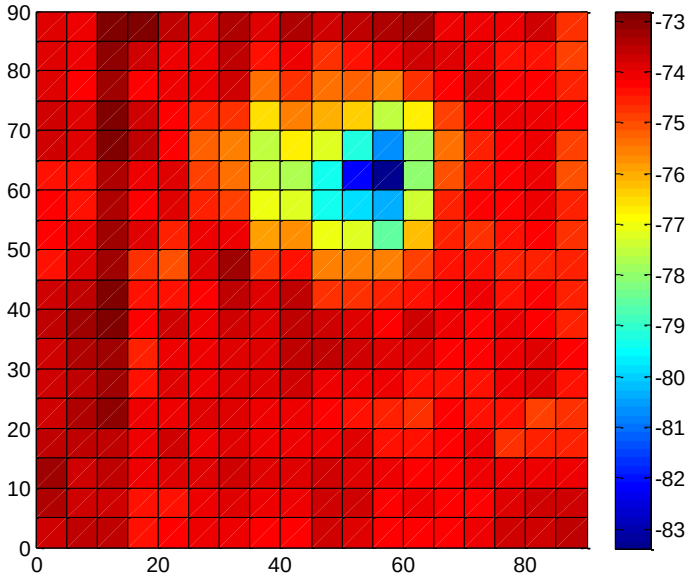

(a)

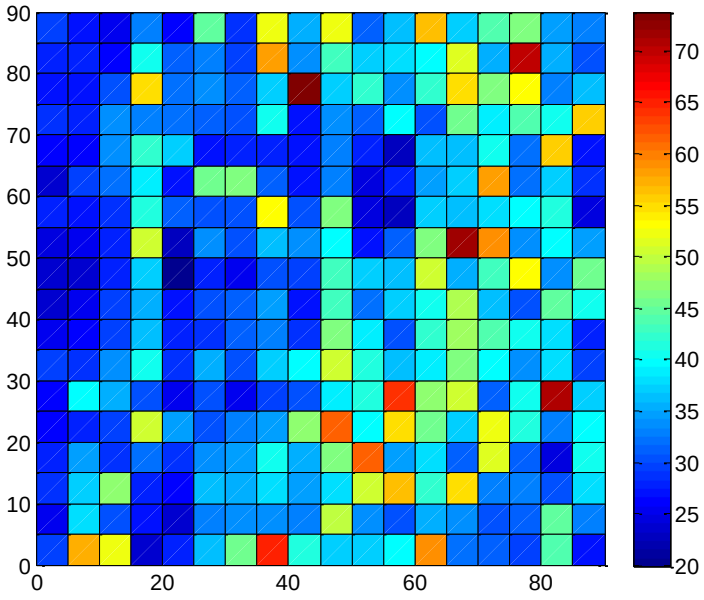

(b)

Fig. 4.19. 2-D plot of scan results with antennas of type 2 over a 9 cm by 9 cm square on the target phantom at 10 GHz calculated using magnitude only: (a) magnitude of the averaged S_{21} and (b) SUR.

3) Phase Only Evaluation

The phase-only evaluation uses the measured S_{21} phase. The averaged S_{21} phase is calculated as

$$\angle S_{21\_Average\ \text{phase}} = \sum_{i=1}^{n} \angle S_{21}^{i} \Big/ n \qquad (4.1)$$

where n is the number of repeated measurements (n = 10). Three sampling frequencies, 3 GHz, 6 GHz and 10 GHz are chosen for the pseudocolor plot of the averaged S_{21} phase in degrees.

Antenna 1

Fig. 4.20 shows the averaged S_{21} phases in degrees for the scan which uses prototypes of antenna 1 at all three frequencies. The phase plot presents good tumor signatures. Generally, phase information is regarded to be much more sensitive to changes in the complex permittivity than the magnitude. It is also more prone to noise. But these results show that the system is capable of preserving accurate phase information.

Antenna 2

Fig. 4.21 shows the same results but when prototypes of antenna 2 are used. At 3 GHz and 6 GHz, the tumor signature is barely recoverable. At 10 GHz, the phase information is completely distorted and there is no sign of the tumor signature at all.

This result indicates that the errors embedded in the phase information for antenna 2 is large. Similar conclusion has also been drawn in Chapter 3, section 3.3.

Based on all three sets of results, we can conclude that overall, antenna 1 has better performance. Antenna 2 suffers from the errors embedded in its phase information, especially at high frequency.

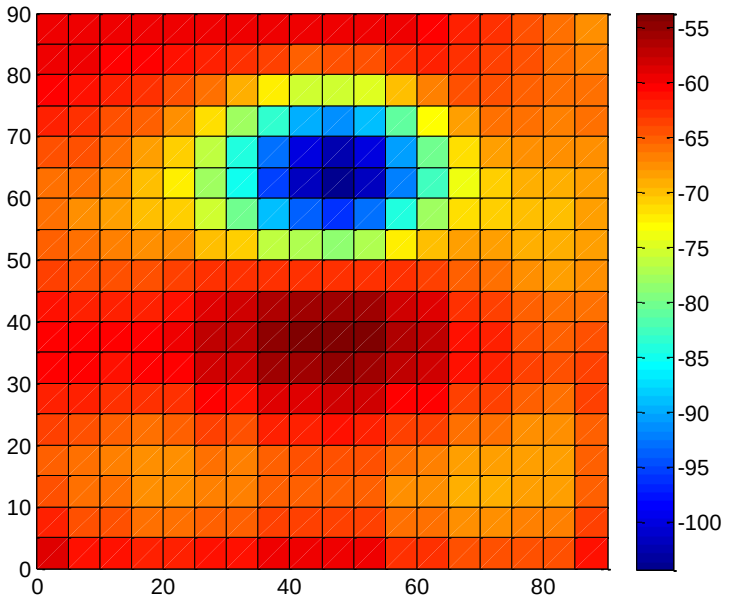
90
80
70
60
50
40
30
20
10
0
0
20
40
60
80
-55
-60
-65
-70
-75
-80
-85
-90
-95
-100

(a)

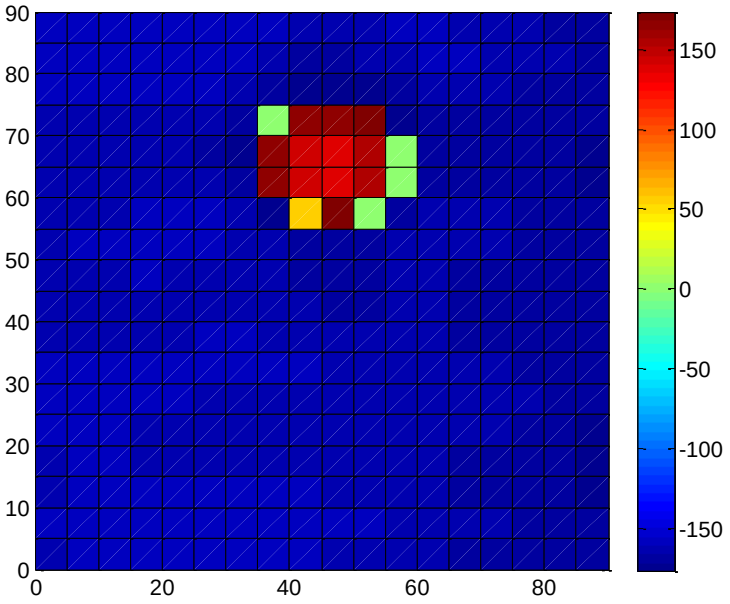
90
80
70
60
50
40
30
20
10
0
0
20
40
60
80
150
100
50
0
-50
-100
-150

(b)

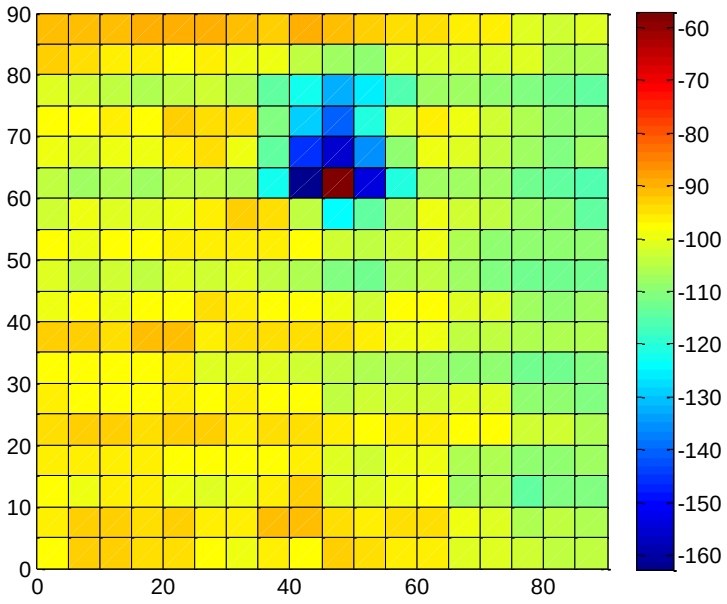

(c)

Fig. 4.20. 2-D plot of averaged phases in degrees for a scan using antennas of type 1 over a 9 cm by 9 cm square on the target phantom at: (a) 3 GHz, (b) 6 GHz, (c) 10 GHz.

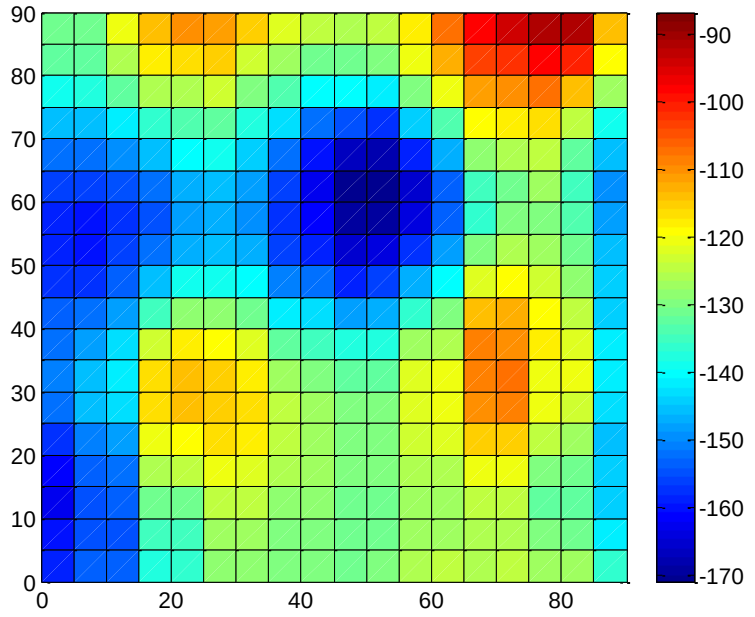
90
80
70
60
50
40
30
20
10
0
0
20
40
60
80
-90
-100
-110
-120
-130
-140
-150
-160
-170

(a)

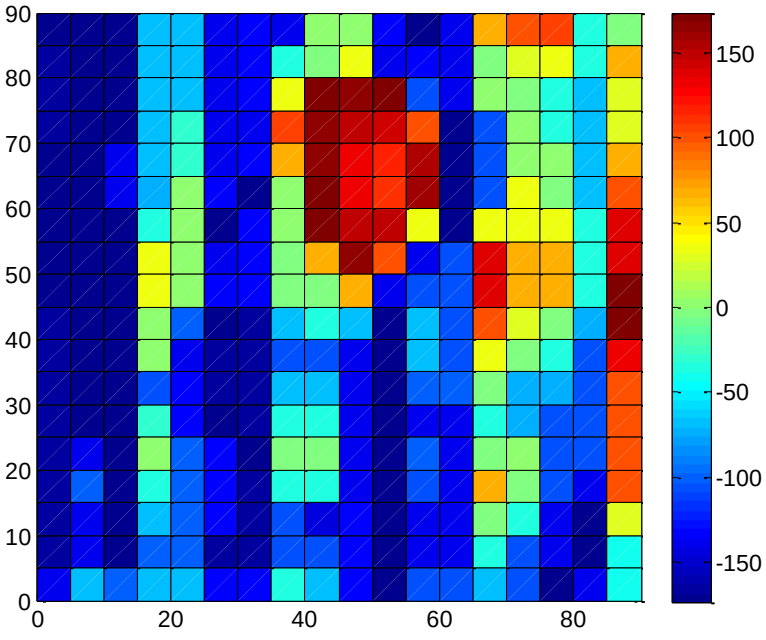
90
80
70
60
50
40
30
20
10
0
0
20
40
60
80
150
100
50
0
-50
-100
-150

(b)

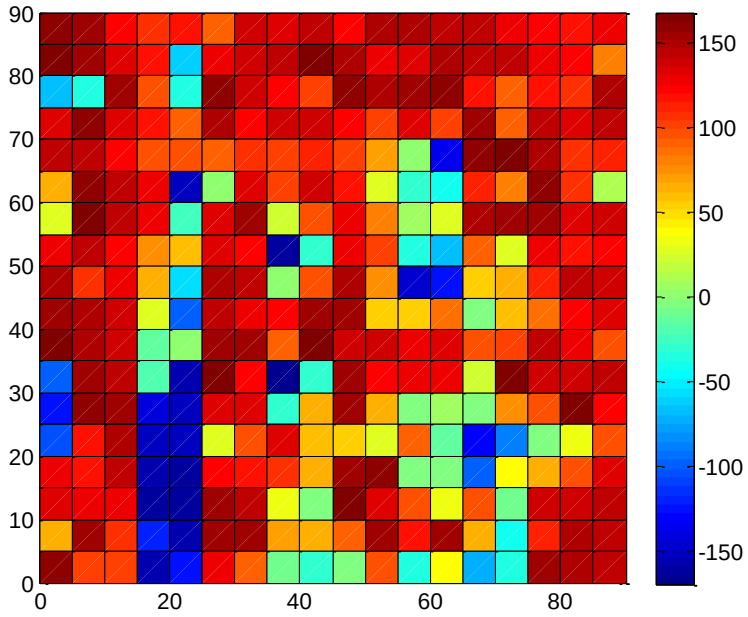

(c)

Fig. 4.21. 2-D plot of averaged phases in degrees for a scan using antennas of type 2 over a 9 cm by 9 cm square on the target phantom at: (a) 3 GHz, (b) 6 GHz, (c) 10 GHz.

4.2.2. Imaging of a Low-loss Background Phantom

A background phantom is a homogeneous phantom with no embedded tumor simulant. Ideally, the homogeneity of the phantom leads to a flat response level when imaged. However, due to the persistence of noise/uncertainty, the imaging results are not likely to be flat and some variances in the signal levels are expected.

This section presents the results of imaging of a low-loss background phantom using antennas of type 2. The phantom is 18 cm by 18 cm wide and 3.5 cm thick. The dielectric properties of the phantom are given in Appendix C. As discussed in the previous section, antenna 2 suffers from errors in its phase component, especially in the high frequency range, but for the sake of complete analysis, the data obtained are still evaluated using all three methods.

1) Complex Value Evaluation

The complex-value evaluation uses the measured S_{21} in complex form. These are formulas (3.2), (3.4) and (3.5) in Chapter 3. Again, 3 sampling frequencies, 3 GHz, 6 GHz and 10 GHz are chosen for the pseudocolor plot of the average S_{21} magnitude and the SUR.

Figs. 4.22 to 4.24 show the 2-D plot of average S_{21} and the SUR when antennas of type 2 scan the phantom described above. All three figures show a tilted signal level, i.e., the signal is stronger in the top left corner and it decreases as going towards the right bottom corner. This may be due to differences in the phantom thickness or permittivity distribution.

The SUR for the plot at 10 GHz shows negative values.

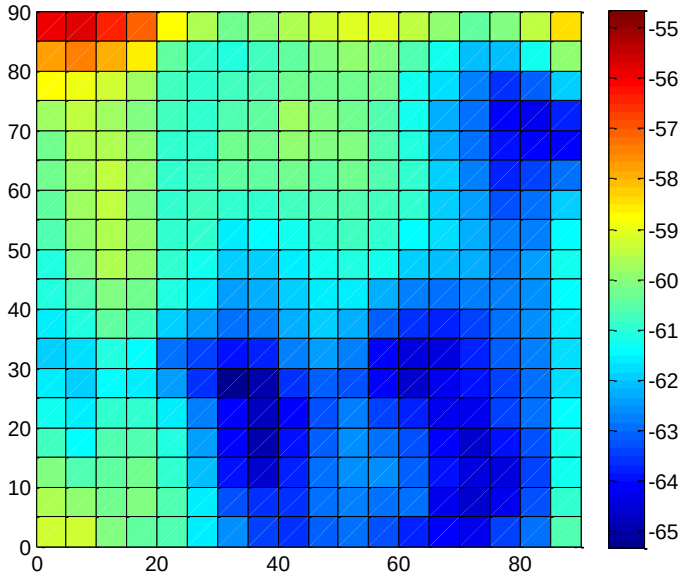

(a)

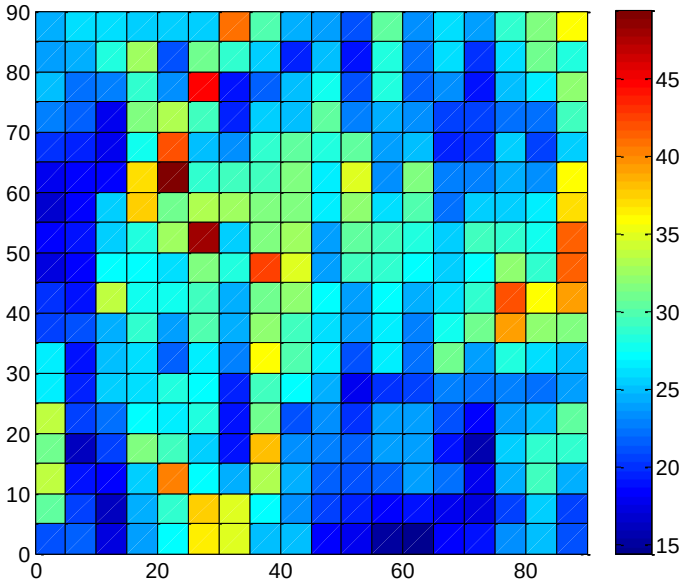

(b)

Fig. 4.22. 2-D plot of scan results with antennas of type 2 over a 9 cm by 9 cm square on the low-loss background phantom at 3 GHz calculated using complex values: (a) magnitude of the averaged S_{21} and (b) SUR.

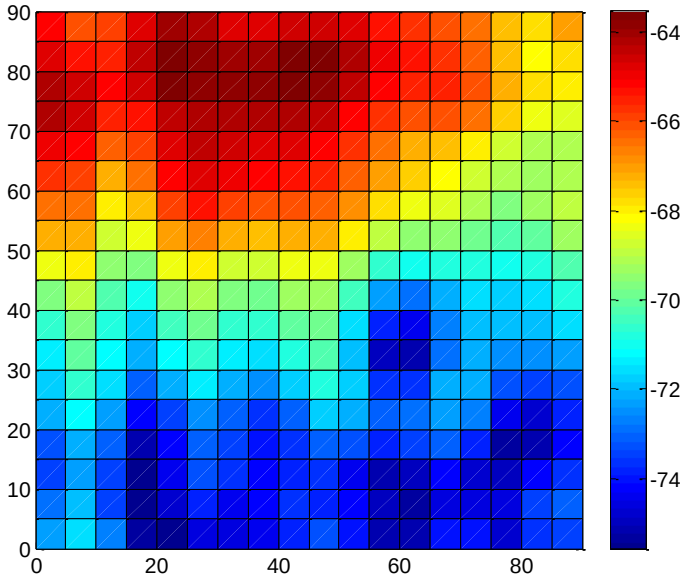

(a)

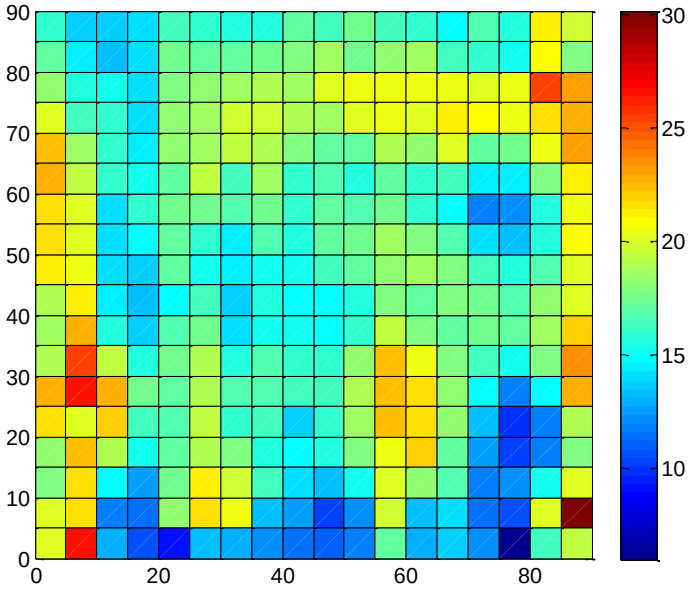

(b)

Fig. 4.23. 2-D plot of scan results with antennas of type 2 over a 9 cm by 9 cm square on the low-loss background phantom at 6 GHz calculated using complex values: (a) magnitude of the averaged S_{21} and (b) SUR.

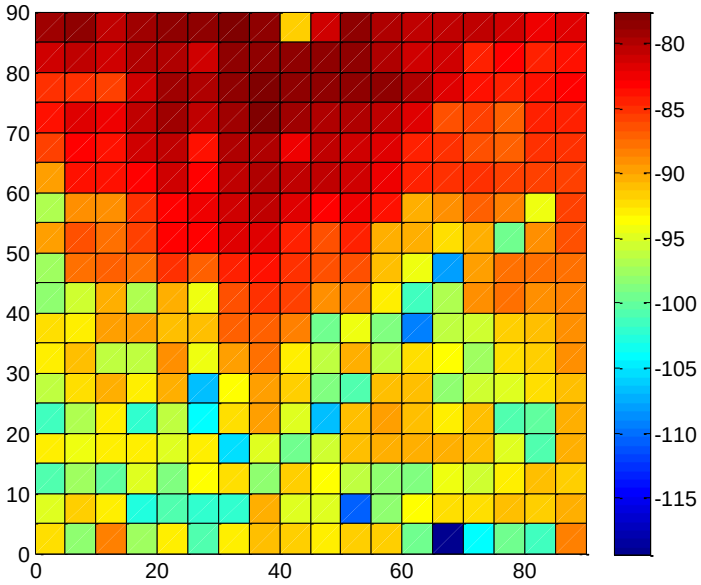

(a)

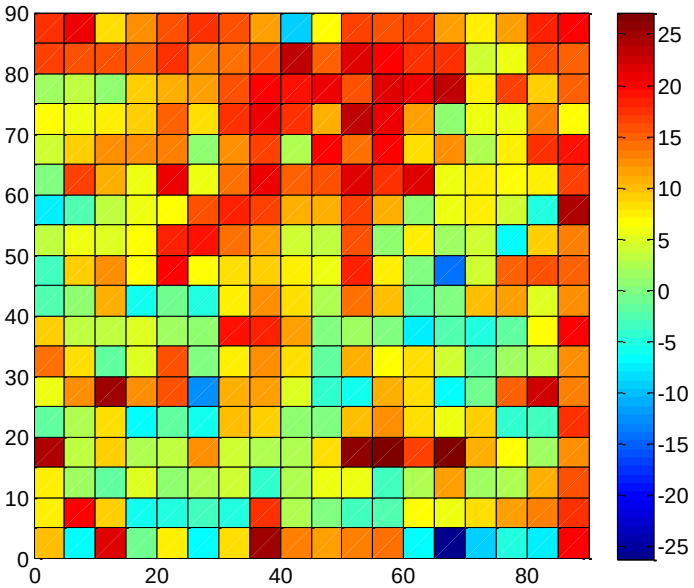

(b)

Fig. 4.24. 2-D plot of scan results with antennas of type 2 over a 9 cm by 9 cm square on the low-loss background phantom at 10 GHz calculated using complex values: (a) magnitude of the averaged S_{21} and (b) SUR.

2) Magnitude Only Evaluation

Magnitude-only value evaluation uses the measured S_{21} magnitude. These are formulas (3.7), (3.8) and (3.5) in Chapter 3. Three sampling frequencies, 3 GHz, 6 GHz and 10 GHz are used for the pseudocolor plot of averaged S_{21} magnitude and the SUR.

Figs. 4.25 to 4.27 show the 2-D plot of averaged S_{21} and the SUR for measurements with antennas of type 2 over a 9 cm by 9 cm square at the centre of the low-loss background phantom.

As expected, the S_{21} plots for all 3 frequencies are visually similar to the plots generated using complex values, and the SUR shows improvement. Particularly, at 10 GHz, the SUR calculated using magnitude only does not exhibit values below 0 dB. This again implies that there are errors in the phase information of antenna 2 at high frequency.

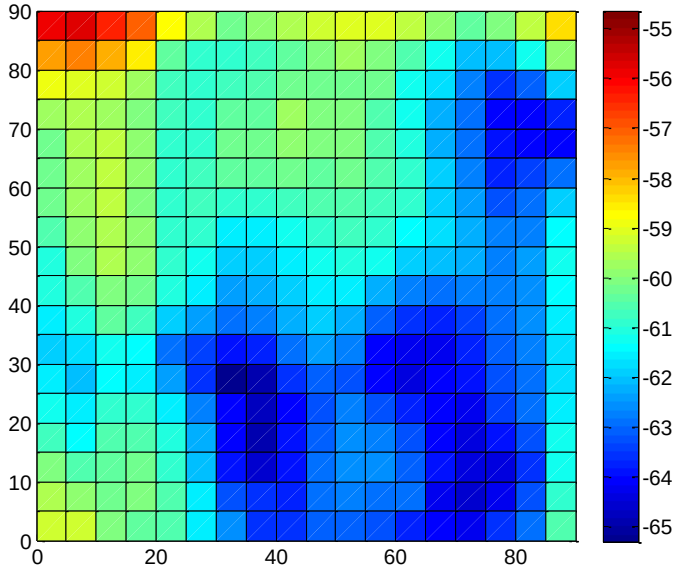

(a)

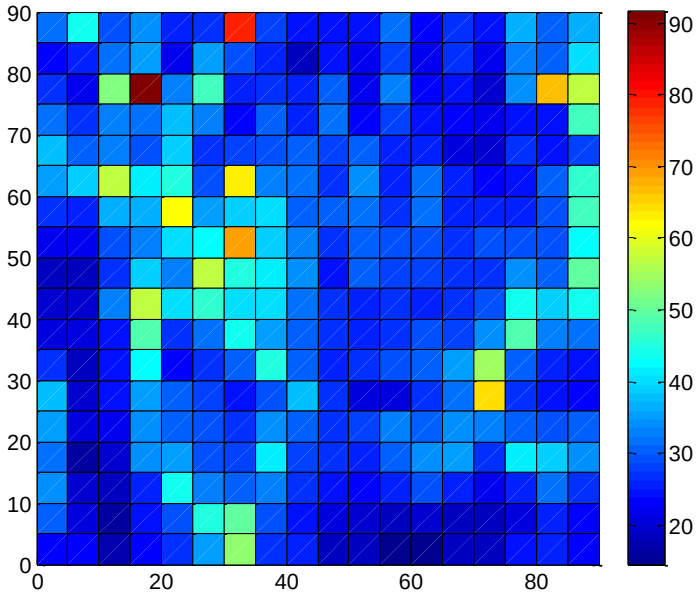

(b)

Fig. 4.25. 2-D plot of scan results with antennas of type 2 over a 9 cm by 9 cm square on the low-loss background phantom at 3 GHz calculated using magnitude only: (a) magnitude of the averaged S_{21} and (b) SUR.

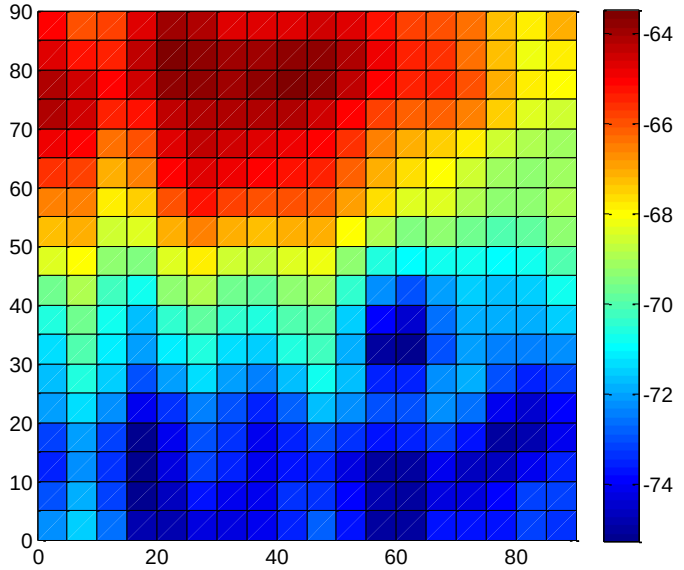

(a)

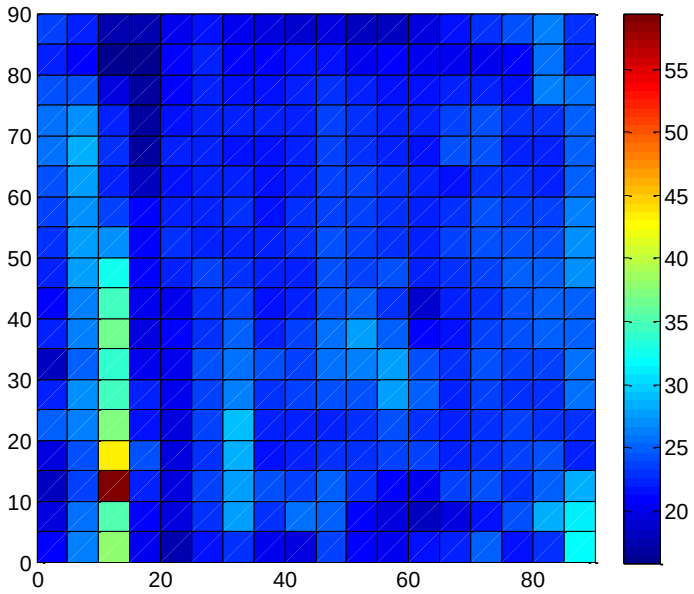

(b)

Fig. 4.26. 2-D plot of scan results with antennas of type 2 over a 9 cm by 9 cm square on the low-loss background phantom at 6 GHz calculated using magnitude only: (a) magnitude of the averaged S_{21} and (b) SUR.

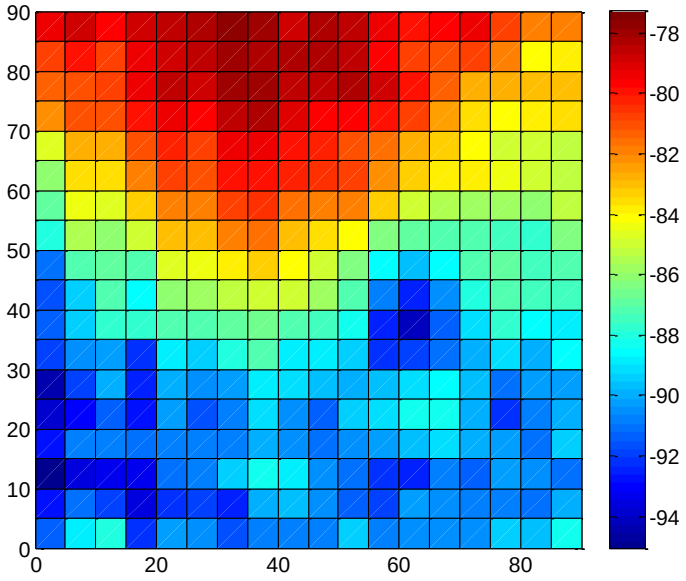

(a)

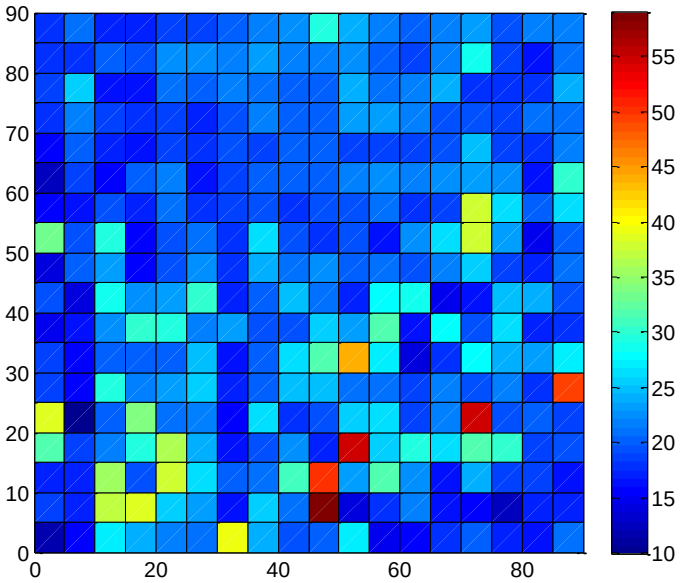

(b)

Fig. 4.27. 2-D plot of scan results with antennas of type 2 over a 9 cm by 9 cm square on the low-loss background phantom at 10 GHz calculated using magnitude only: (a) magnitude of the averaged S_{21} and (b) SUR.

3) Phase Only Evaluation

Phase-only evaluation uses formula (4.1) to calculate the averaged phase for every sampling point on the scanned area at each frequency point. Three sampling frequencies, 3 GHz, 6 GHz and 10 GHz are chosen for the pseudocolor plot of the average S_{21} phase in degrees.

Fig. 4.28 shows the 3 plots of the measured scan data at the 3 frequencies. The plots at the low and mid frequencies show similar trend of the signal level as compared to the plots generated using either complex value or magnitude. If the phase is restricted between -180 degree and +180 degree, the signal goes from high value at the top to low value at the bottom. The plot at 10 GHz is again distorted and no pattern can be recovered.

Based on the results generated using the three different methods above, we can conclude that with a background phantom, the measured S_{21} are not flat as we expected. In this particular case, the phantom is low-loss and is relatively thin (3.5 cm thick). The signal measured at the end of the scanned area has around 10 dB difference compared to the signal measured at the lower end at all 3 sampled frequencies. Since for every measurement, the overall height of the imaged object, which includes the height of the phantom plus the thickness of the two plexiglass plates is measured at different locations to make sure it is constant. The tilted signal level is more likely to be due to the constitutive properties of the phantom and its thickness before constraining it between the two plexiglass plates. For example, the phantom could be thicker on one side than the other, thus when

stabilizing the phantom in place, one side of the phantom is squeezed more than the other side.

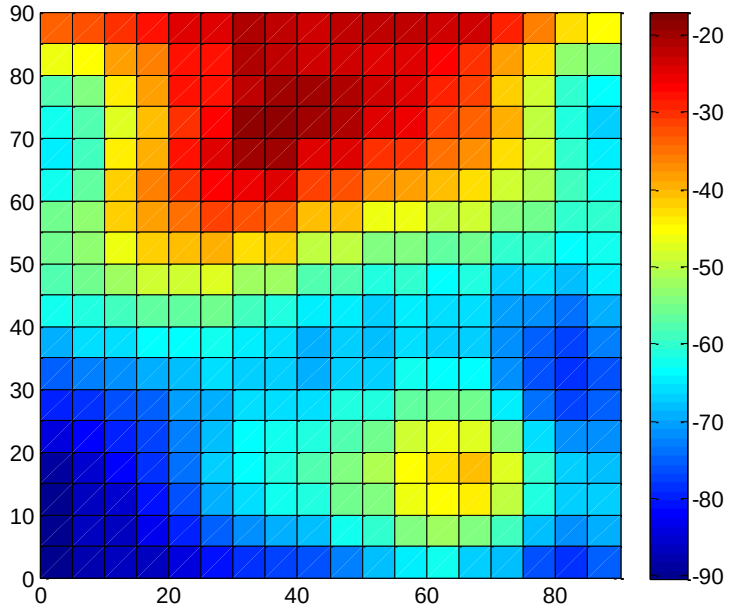
90
80
70
60
50
40
30
20
10
0
0
20
40
60
80
-20
-30
-40
-50
-60
-70
-80
-90

(a)

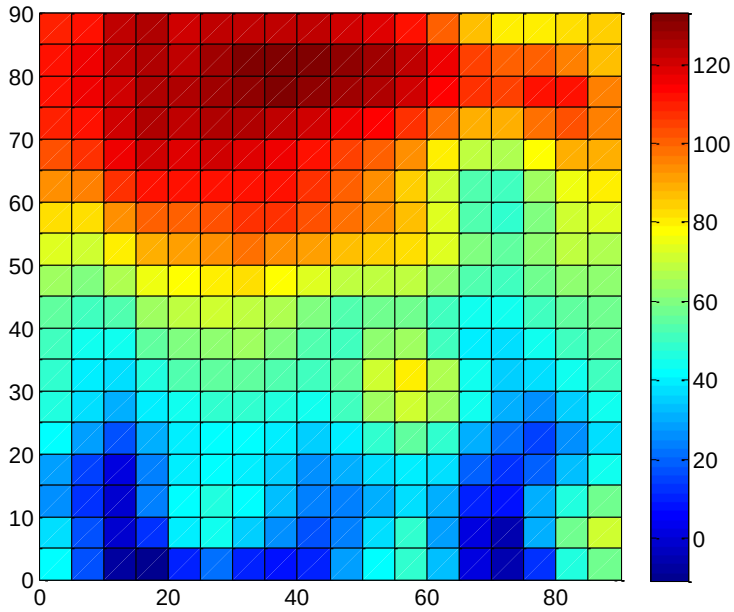
90
80
70
60
50
40
30
20
10
0
0
20
40
60
80
120
100
80
60
40
20
0

(b)

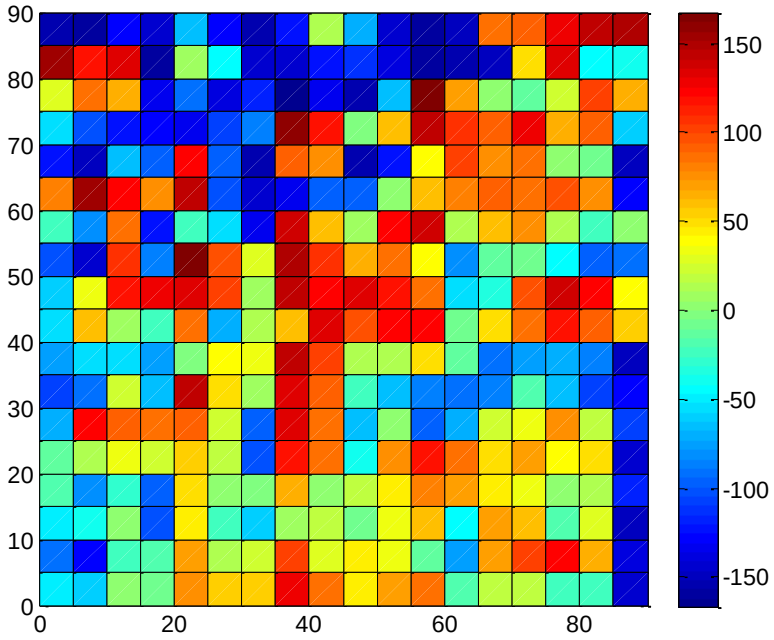

(c)

Fig. 4.28. 2-D plot of averaged phases in degrees for a scan using antennas of type 2 over a 9 cm by 9 cm square on the low-loss background phantom at: (a) 3 GHz, (b) 6 GHz, (c) 10 GHz.

4.2.3. Imaging of a High-loss Background Phantom

This section presents the results of imaging of a high-loss background phantom using antennas of type 1. The phantom is 14 cm by 14 cm wide and 3.5 cm thick. The dielectric properties of the phantom are given in Appendix C. The measured results are analyzed using three different methods.

1) Complex Value Evaluation

The complex-value evaluation uses the measured S_{21} in complex form. These are formulas (3.2), (3.4) and (3.5) in Chapter 3. Again, 3 sampling frequencies, 3 GHz, 6 GHz and 10 GHz are chosen for the pseudocolor plot of the average S_{21} magnitude and the SUR.

Figs. 4.29 to 4.31 show the 2-D plot of averaged S_{21} and SUR when antennas of type 2 scan the phantom described above. As all three figures have shown, the measured results do not present a uniformed S_{21} signal level. The difference between strongest signal level and lowest signal level at one frequency is about 20 dB. Also, at all 3 frequencies, the SUR plots show many points where values are negative.

This result implies that for measurement of high-loss phantoms, a boost in the signal level is needed to combat the noise.

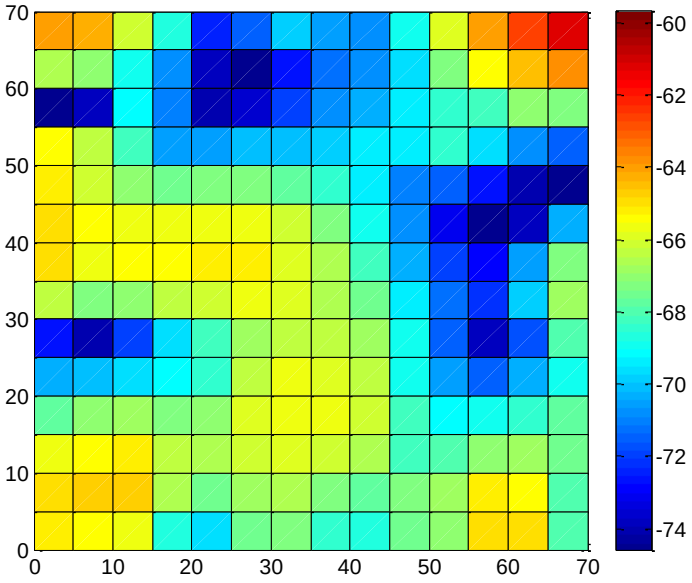

(a)

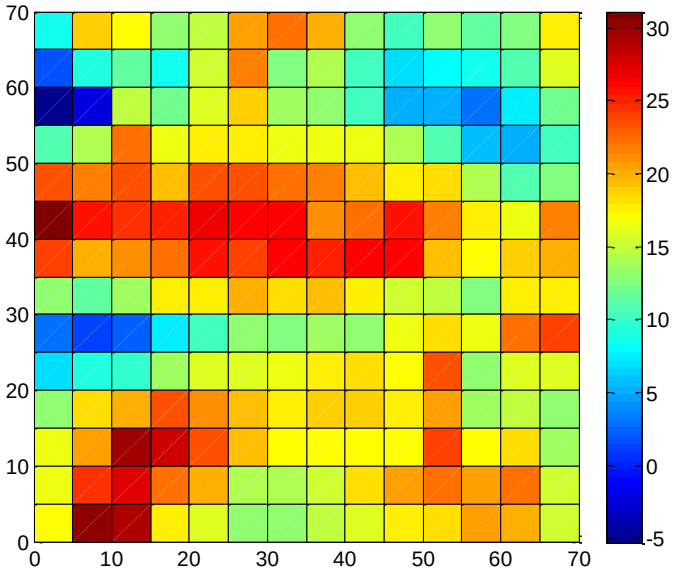

(b)

Fig. 4.29. 2-D plot of scan results with antennas of type 1 over a 7 cm by 7 cm square on the high-loss background phantom at 3 GHz calculated using complex values: (a) magnitude of the averaged S_{21} and (b) SUR.

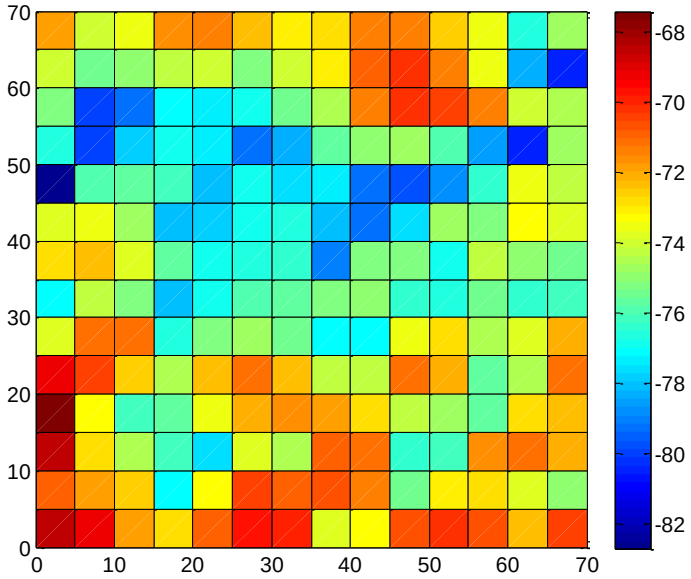

(a)

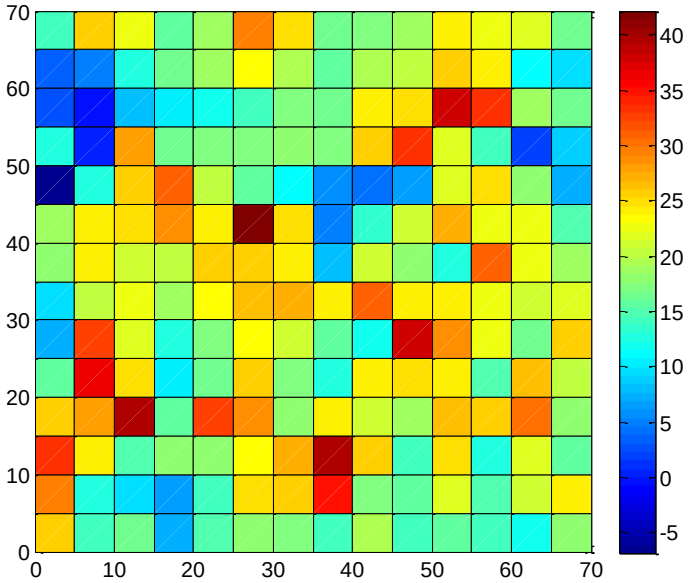

(b)

Fig. 4.30. 2-D plot of scan results with antennas of type 1 over a 7 cm by 7 cm square on the high-loss background phantom at 6 GHz calculated using complex values: (a) magnitude of the averaged S_{21} and (b) SUR.

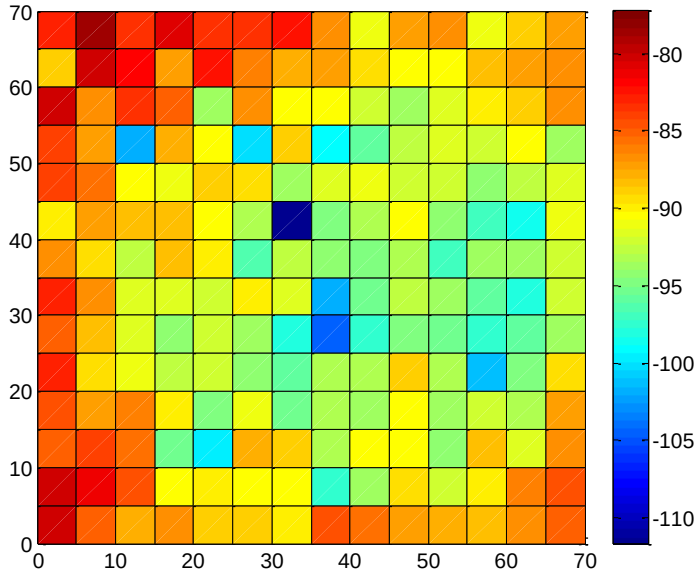

(a)

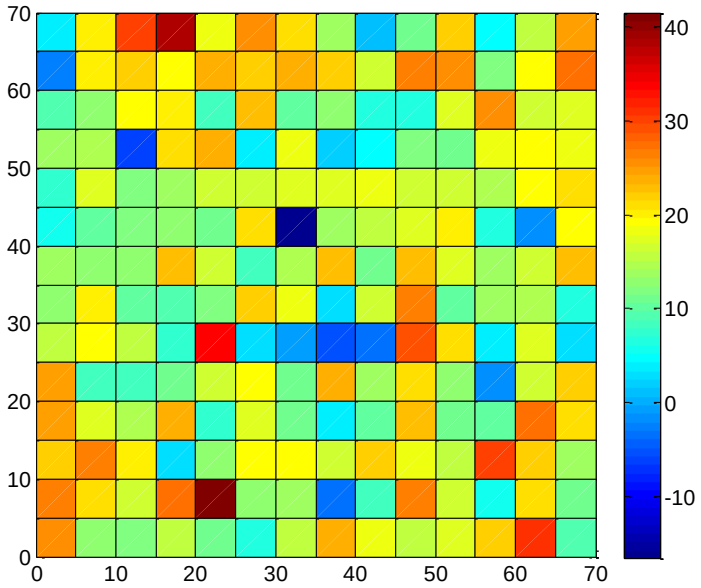

(b)

Fig. 4.31. 2-D plot of scan results with antennas of type 1 over a 7 cm by 7 cm square on the high-loss background phantom at 10 GHz calculated using complex values: (a) magnitude of the averaged S_{21} and (b) SUR.

2) Magnitude Only Evaluation

Magnitude-only value evaluation uses the measured S_{21} magnitude. These are formulas (3.7), (3.8) and (3.5) from Chapter 3. Three sampling frequencies, 3 GHz, 6 GHz and 10 GHz are chosen for the pseudocolor plot of average S_{21} magnitude and the SUR.

Figs. 4.32 to 4.34 show the 2-D plot of average S_{21} and SUR for antenna 1 over a 7 cm by 7 cm square on the high-loss background phantom.

The results from magnitude only evaluation show improvements in both S_{21} signal level and the SUR. However, the signal level is still not flat and the difference between strongest signal level and weakest signal level in either plot is around 15 dB.

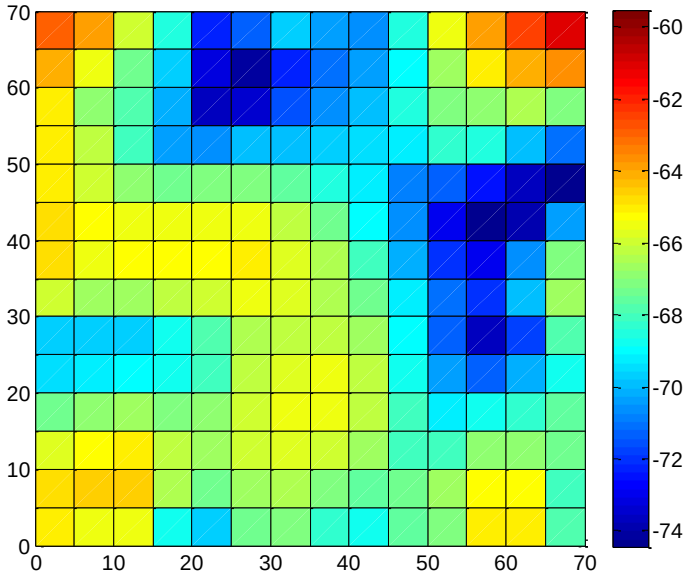

(a)

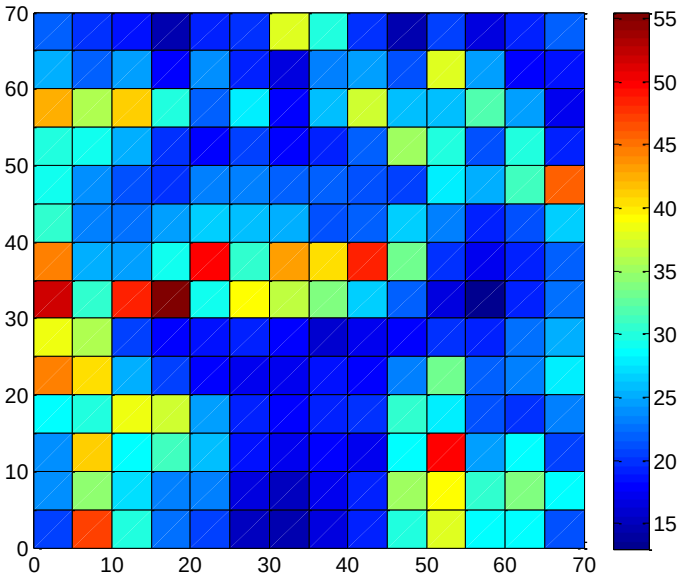

(b)

Fig. 4.32. 2-D plot of scan results with antennas of type 1 over a 7 cm by 7 cm square on the high-loss background phantom at 3 GHz calculated using magnitude only: (a) magnitude of the averaged S_{21} and (b) SUR.

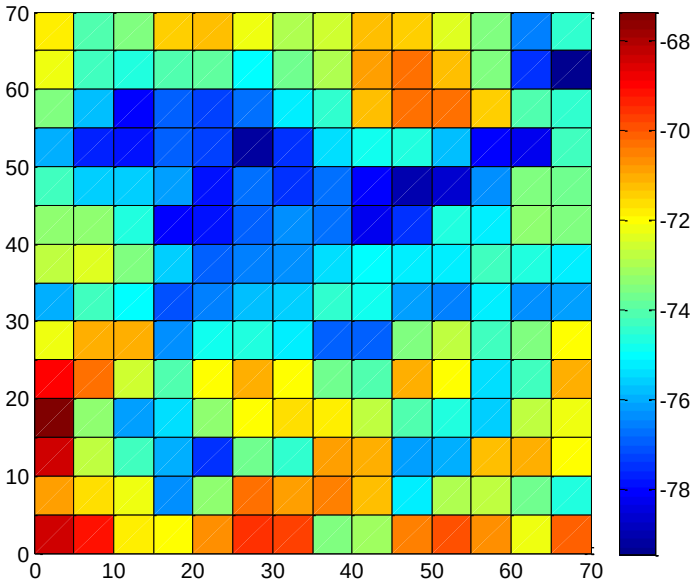

(a)

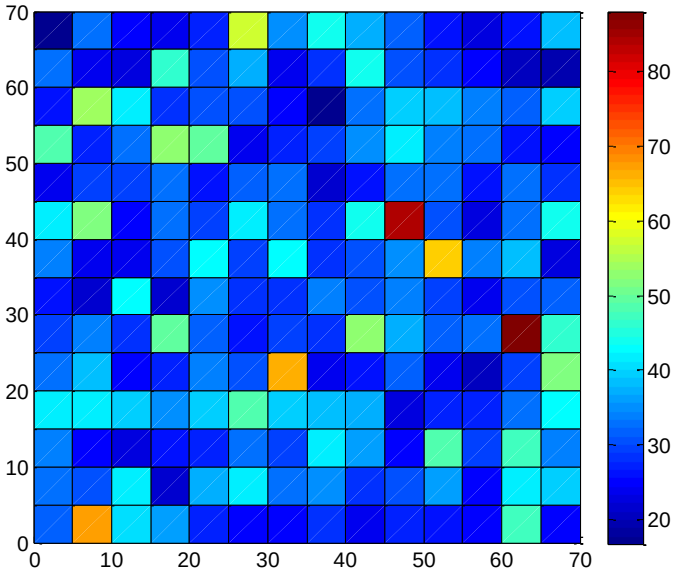

(b)

Fig. 4.33. 2-D plot of scan results with antennas of type 1 over a 7 cm by 7 cm square on the high-loss background phantom at 6 GHz calculated using magnitude only: (a) magnitude of the averaged S_{21} and (b) SUR.

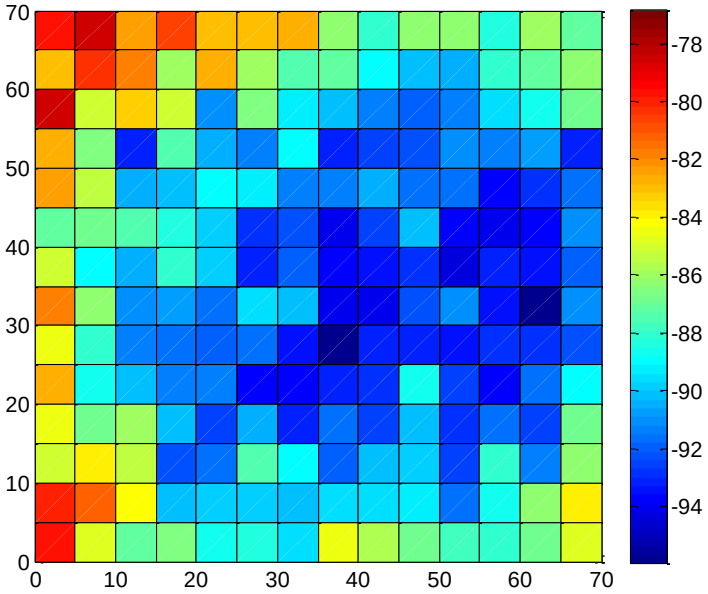

(a)

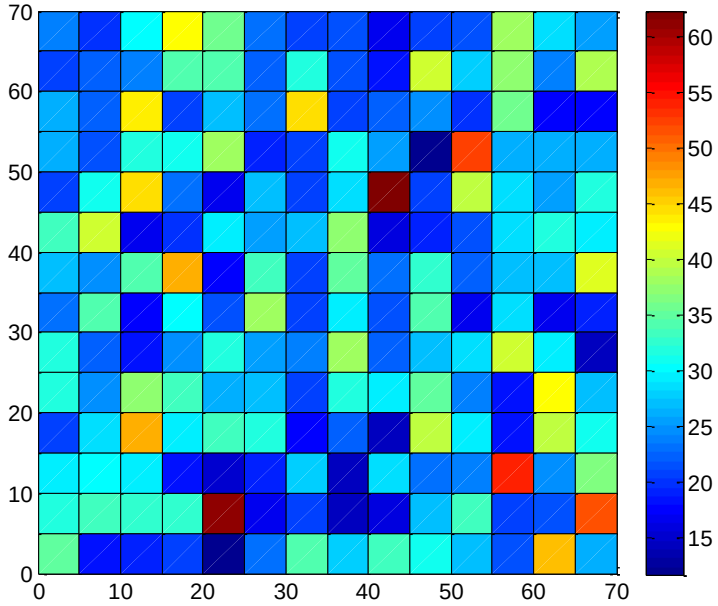

(b)

Fig. 4.34. 2-D plot of scan results with antennas of type 1 over a 7 cm by 7 cm square on the high-loss background phantom at 10 GHz calculated using magnitude only: (a) magnitude of the averaged S_{21} and (b) SUR.

3) Phase Only Evaluation

Phase-only evaluation uses formula (4.1) to calculate the averaged phase for every sampling point on the scanned area at each frequency point. Three sampling frequencies, 3 GHz, 6 GHz and 10 GHz are chosen for the pseudocolor plot the average S_{21} phase in degrees.

Fig. 4.35 shows the 3 plots of the measured scan data at the 3 frequencies. No pattern can be recovered in plots at all 3 frequencies.

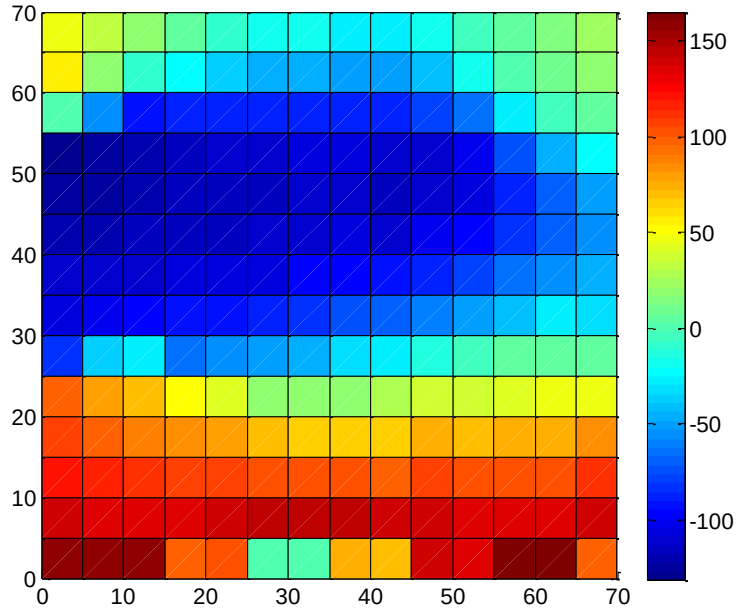
70
60
50
40
30
20
10
0
0 10 20 30 40 50 60 70
150
100
50
0
-50
-100

(a)

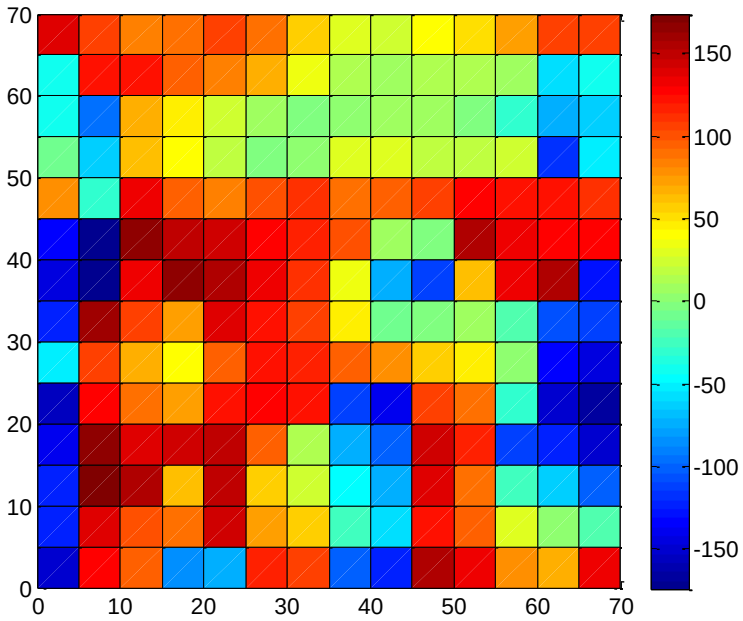
70
60
50
40
30
20
10
0
0 10 20 30 40 50 60 70
150
100
50
0
-50
-100
-150

(b)

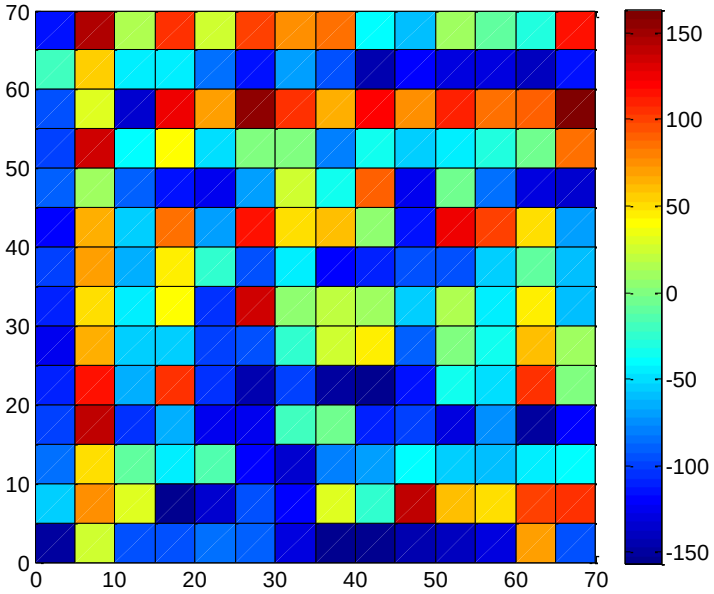

(c)

Fig. 4.35. 2-D plot of averaged phases in degrees for a scan using antennas of type 1 over a 7 cm by 7 cm square on the high-loss background phantom at: (a) 3 GHz, (b) 6 GHz, (c) 10 GHz.

4.3 Conclusion

In this chapter, several measurement results are presented to demonstrate the capabilities and the limitations of the implemented raster-scanning system. Based on these results, we can conclude that antenna 1 has better performance over antenna 2, which suffers from lower coupling efficiency, and distortion in the phase information at high frequencies. This could be due to the fabrication of the antenna 2 since its simulation results are actually very promising. Thus further experiments are needed with new sets of antenna 2. Furthermore, the results demonstrate that the imaging of a background phantom does not produce a flat signal level due to some intrinsic differences in the phantom properties. Lastly, the results have shown that the imaging of high-loss phantom does not produce good SUR. Thus, low-noise-amplifier might be needed if thicker or lossier phantoms are imaged.

References

[1] MATLAB™ 2010, The MathWorks Inc., 3 Apple Hill Drive, Natick, MA, 2010. [Online]. http://www.mathworks.com/.

[2] Ansoft HFSS ver. 12, Ansoft Corporation, 225 West Station Square Drive, Suite 200, Pittsburgh, PA 15219 USA, 2011. [Online]. http://www.ansoft.com.

CHAPTER 5

CONCLUSION AND SUGGESTIONS FOR FUTURE WORK

5.1 Conclusions

This thesis describes contributions which can aid research on microwave imaging for breast-cancer detection. The achievements are:

- The design, fabrication and improvement of a planar raster-scanning imaging system which enables the users to do fast, reliable scattering-

parameter acquisitions on a physical phantom. This is a big step because we can now acquire real phantom measurements data instead of relying only on simulators when verifying imaging and post-processing algorithms. The developed system uses a vector network analyzer (VNA) as its measuring instrument. The system structure is made of medium-density fiberboard (MDF board), 2×4 S-P-F lumber and plexiglass plates. Step motors along with timing belts, linear and rotary bearings are used to build the raster scanning mechanism. The whole system is integrated and controlled using Matlab [1] script, which consists of an easy to use graphic user interface (GUI). A complete list of parts used in building this raster-scanning setup is attached in Appendix A. For detailed operating instructions, an operating manual is written and is attached as Appendix B

- A comprehensive study of the dynamic range of the developed raster-scanning imaging system is carried out. This study aims at identifying and quantitatively characterizing the uncertainties of the system. The final results have shown that the system is robust against noise and the measured data are reliable, but highly dependent on the used microwave sensors. However, please note that the uncertainty level of the current setup is 30 dB above the intrinsic noise floor of the VNA. And the studies are carried out on low-water-content and medium-water-content phantoms which do not exhibit significant loss. The measurements have shown good signal to uncertainty ratio. But for measuring of a high loss phantom, the uncertainty

level of the current setup might be too high. Possible improvements are discussed later in this chapter.

- Typical imaging results on different types of physical phantoms are presented. They showcase the performance and the capabilities of the developed system along with its limitations. These results are important for further improvement of the system.

5.2 Suggestions for Future Work

This system is a prototype of the raster-scanning setup for the detection of breast cancer. As a prototype, this system enables the user to carry out numerous experiments and to develop and verify new imaging algorithms. However, the performance of the current setup is limited by its components and design. Based on the results presented in this thesis, the uncertainty level of the current system is about 30 dB above the intrinsic noise floor of the VNA. Thus, suggestions are made for future work toward the reduction of the uncertainty level of the imaging system.

- Matlab is a relatively easy approach to writing scripts for the control of the imaging system. However, Matlab is not a professional control software and its control tool box has limited capabilities. It is desirable to integrate the system using professional control software, such as LabView [2]. The development of the system control using LabView is under way.

- For better isolations of the system, it is important to wrap up all connectors with absorbing sheets to suppress RF leakage. Thus, further measurements need to be carried out to study the effect of absorbers
- The precision alignment of the antennas is a big challenge in the current setup. There are two factors affecting the precision of the antenna alignment. The vertical motion of the solenoid and the lateral motion of the step motors. Of these two factors, the first one is easier to improve. The vertical positioning of the antennas using solenoids and springs is not the best solution but is relatively simple and easy to control. Thus, to reduce the uncertainty level, it is important to design better antenna holders, which would provide stable and precise alignment of the antennas. To achieve this, we can extend the side plates of the current antenna holder upward so that the rotation of the antenna holder is constrained by the sides of the solenoids. For the antenna positioning inside the antenna holder however, we can attach a thin slab of plexiglass to the bottom of the antenna holder. Thus when adjusting the screw, we can easily tell that the aperture of the antenna is parallel to the phantom surface. These ideas are illustrated in Fig. 5.1.

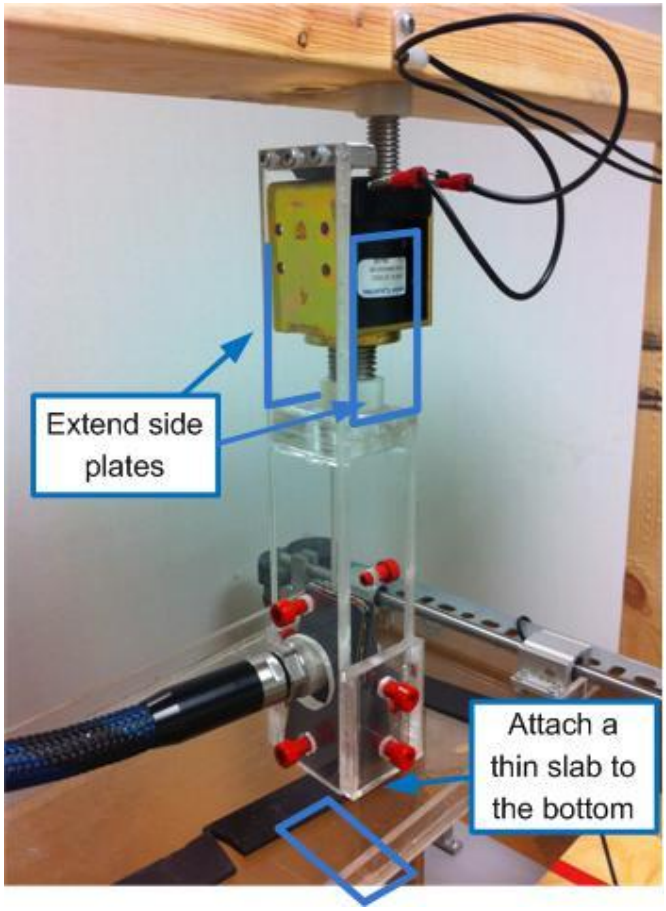

Fig. 5.1. The illustration of the improvements on antenna holders.

- For the lateral motion of the step motor, there is no easy way to monitor the actual position of the antenna, i.e., using laser pointer. So it is not practical at this stage to implement a closed-loop system. The accuracy of the positioning heavily relies on the precision of the step motors. The main concern now is that the big motor generates too much vibration while moving. This contributes to the uncertainties in lateral movements. Thus, it's desirable to replace the big motor if we can find a step motor with more

steps per revolution. This leads to smoother stepping which generates less vibration.

- Other than the hardware improvements described above, more robust and effective imaging algorithms can be developed to counter act noise and uncertainties.

References

[1] MATLAB 2010, The MathWorks Inc., 3 Apple Hill Drive, Natick, MA, 2010. [Online]. http://www.mathworks.com/.

[2] LabView ver. 8.5, National Instruments Corporation, 11500 N MoPac Expressway Austin, TX 78759-3504 USA, 2011. [Online]. http://www.ni.com.

APPENDIX A
LIST OF PARTS

Raster Scanner Physical Sturcutre

All dimensions shown are in centimeters.

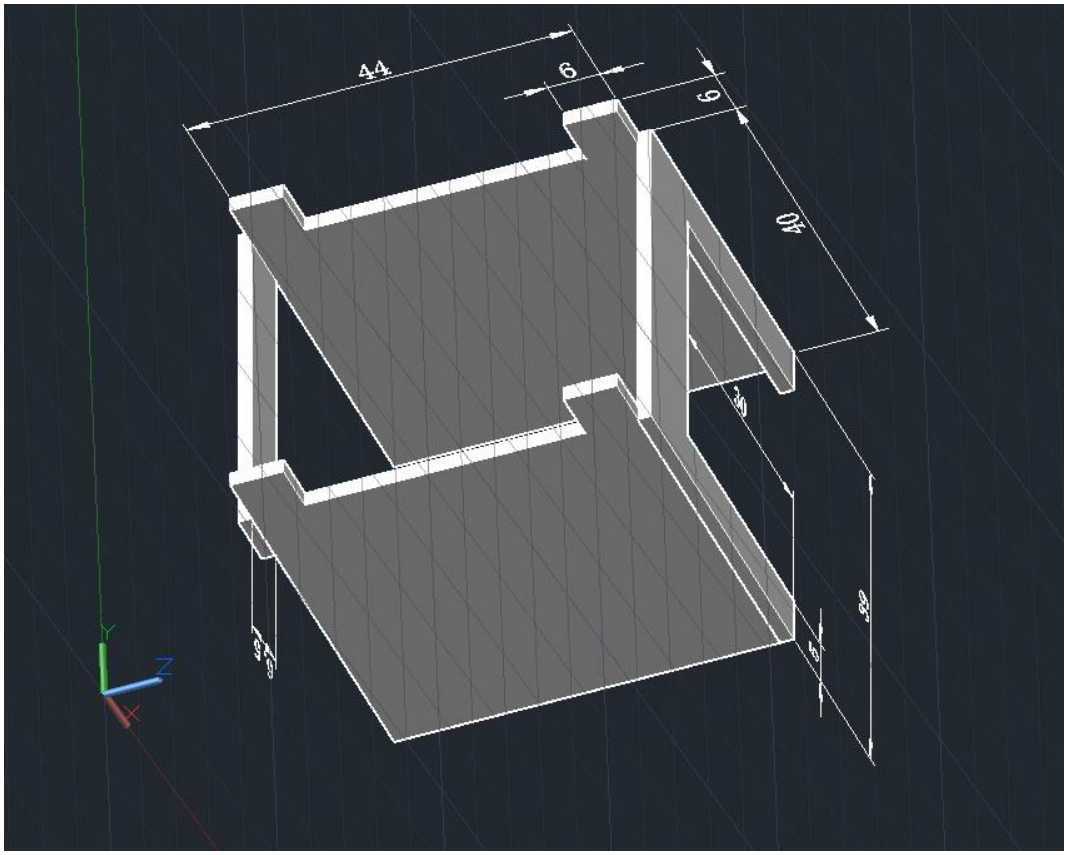

Fig. A.1. Dimensions of the scanning-table. The frame is made of medium-density fiberboard (MDF board).

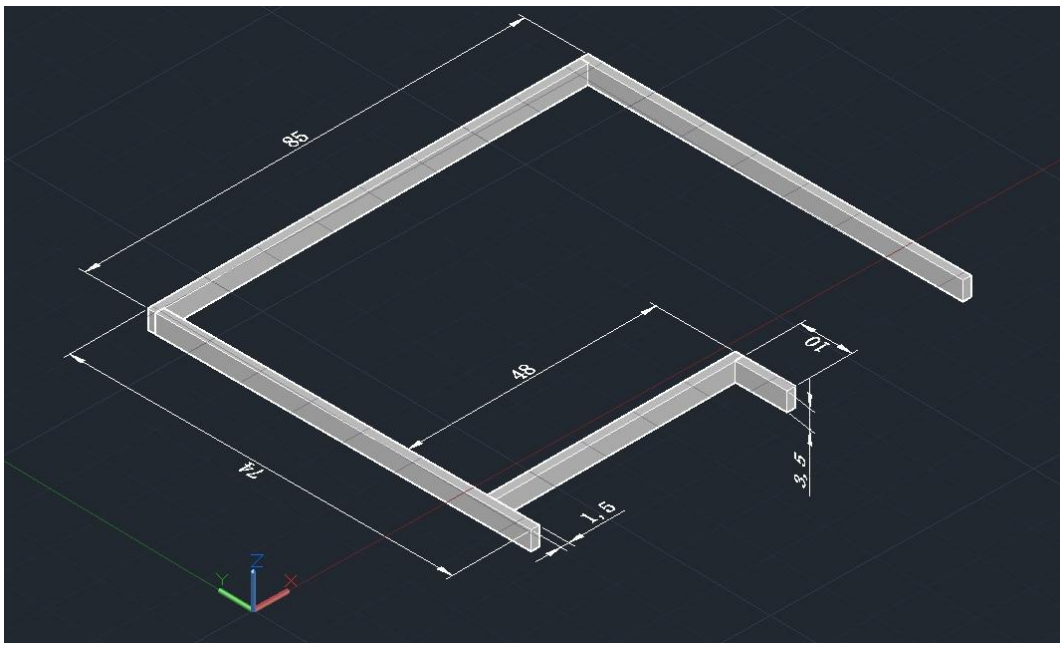

Fig. A.2. Dimensions of the antenna mount frame. The frame is made of 2″×4″ S-P-F lumber.

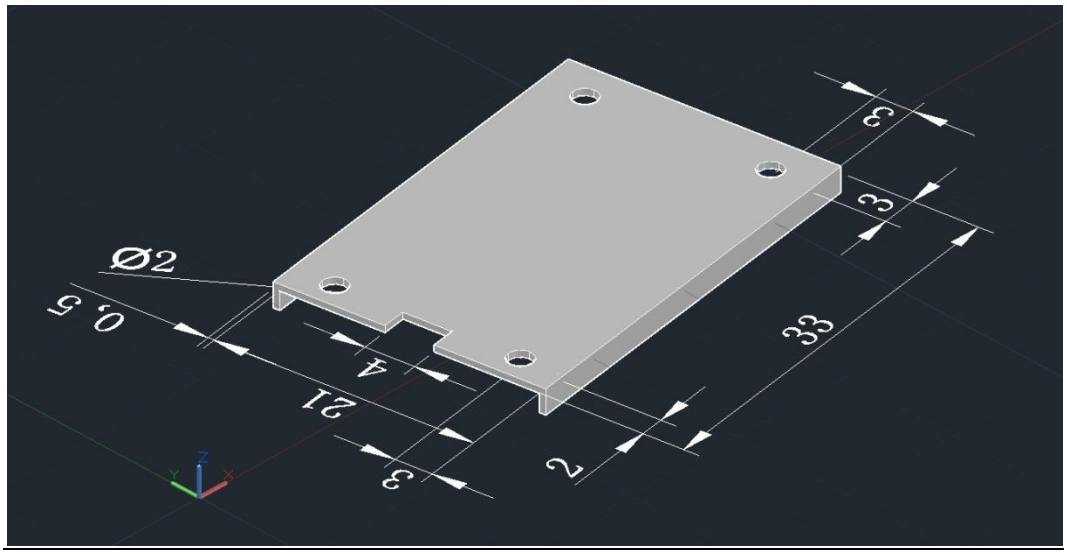

Fig. A.3. Dimensions of the top plate of phantom holder. The plate is made of plexiglass.

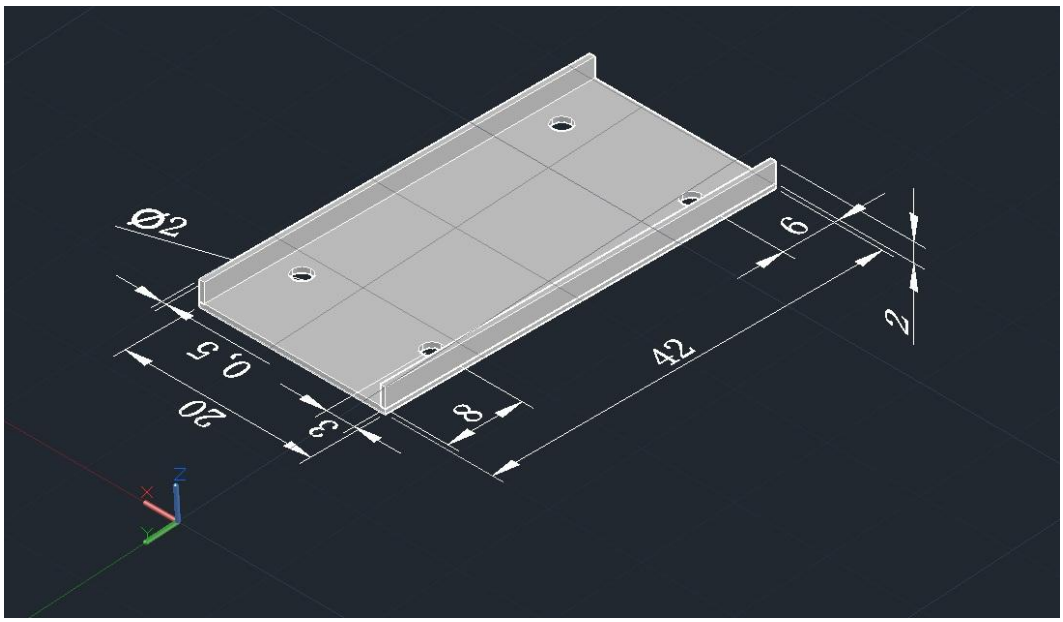

Fig. A.4. Dimensions of the bottom plate of phantom holder. The plate is made of plexiglass.

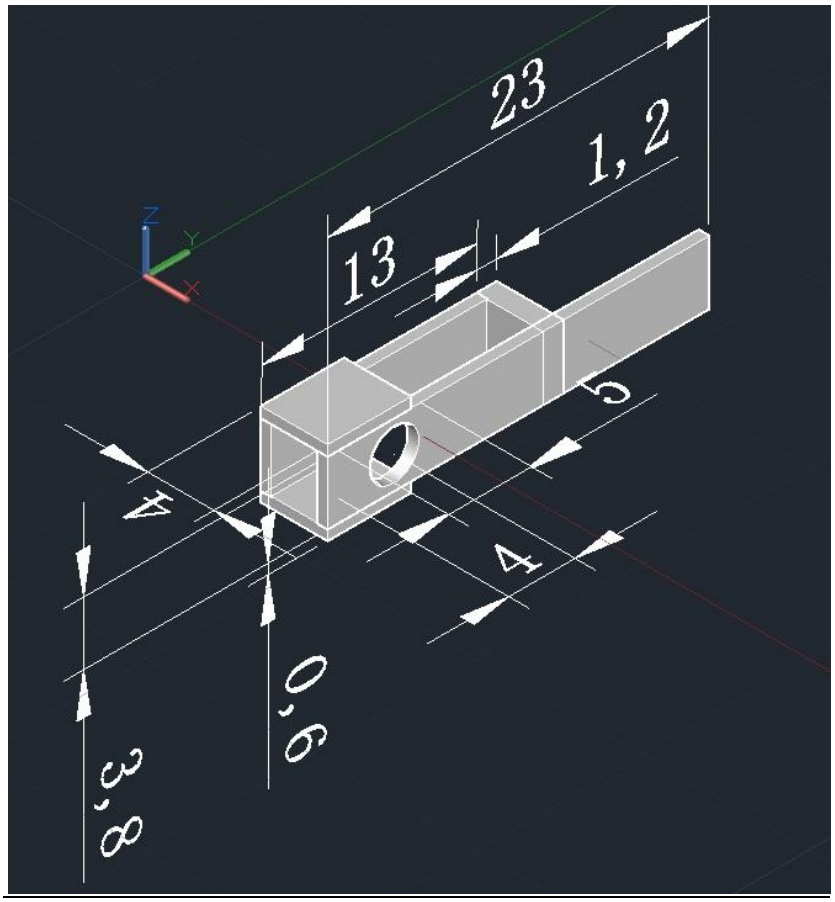

Fig. A.5. Dimensions of the antenna holder. The plate is made of plexiglass.

Big step motor:
Slo-Syn SS250-1005 Stepper Motor × 1
No data sheet available, available information are:
Nominal Voltage: 9.0 V
Steps per Revolution: 200
Current: 1.5 A
Direction: Reversible

Small motor:
HURST Series 49 mm (AS, ABS) Geared Stepping Motor × 2
Part Number: AS 3004-001
Data sheet available at:
http://www.hurst-motors.com/documents/AS_ABS_Step_Geared.pdf

Cables and adapters
8-pin male D-subminiature connectors ×2

Agilent E2078A/82350A GPIB adapter ×1
Data sheet available at:
http://cp.literature.agilent.com/litweb/pdf/5966-2720E.pdf

Standard 25-pin D shape parallel cable ×1

Diodes
1N5400 ×8
Data Sheet available at:
http://www.diodes.com/datasheets/ds28007.pdf

1N4003 ×3
Data sheet available at:
http://www.elfak.ni.ac.rs/phptest/new/html/Studije/predavanja-literatura/osnove/pdffiles/1N4001-D.pdf

Emergency switches:
Omron V-15G2-1C25-K switch ×4
Data sheet available at:
http://datasheet.octopart.com/V-15G2-1C25-K-Omron-datasheet-110008.pdf

Linear bearings, pillow blocks, shaft support and brushings
All parts from Bearing & Oil Seals Specialists Inc.

Class-L 1/2"×30 precision hardened / ground shaft ×2

3/8"×4" ground shaft ×1

3/8"×18" hardened and ground precision shaft ×2

P – 06 Teflon pillow block, 3/8" dia ×3

TWA-8UU linear pillow block ×4

1/2" ball bearing pillow block for timing belt ×2

WH8A shaft support ×4

WH6A shaft support ×4

3/8"×1/2"×1-1/2" bronze brushings ×2

Mosfets
IRF520 Power Mosfet ×10
Data sheet available at:
http://www.futurlec.com/Transistors/IRF520.shtml

Relay
TE DPDT T92S11D22-12 Industrial Relay ×1
Data sheet available at:
http://www.te.com/commerce/DocumentDelivery/DDEController?Action=showdoc&DocId=Data+Sheet%7F1308242_T92%7F0910%7Fpdf%7FEnglish%7FENG_DS_1308242_T92_0910.pdf%7F9-1393211-3

Resistors
100 ohm ×10

Solenoids
4HD-C-12 ×2
Part Number: A420-065432-00
Data sheet available at:
http://www.guardian-electric.com/pdf/4HDDCFrameSolenoids.pdf

Timing belts and pulleies
Flex-E-Grip timing belts (for small motor) ×1
Part Number: 8TB-518

Flex-E-Grip timing belt (for big motor) ×1
Part Number: 50TB-66

Flex-E-Grip series pulley ×2
Part Number: 8TP3-75

Data sheet available at:
http://datasheets.globalspec.com/ds/211/BergWM/599E4ECF-FD7C-461D-BB17-28BED83E0814

Miscellaneous

6/6 threaded nylon rod, 1/2″ in diameter, 30 cm long ×6

6/6 threaded metal rod, 1/2″ in diameter, 30 cm long ×2

6/6 threaded nylon nuts, 1/2″ in diameter ×20

Red screws for stabilizing antennas ×16
Part of Pomona Insulated banana jack 5935-2

APPENDIX B
PLANAR RASTER-SCANNING SYSTEM OPERATING MANUAL

The layout of the control GUI is shown below. The interface is divided into four categories which can be shown as the four rectangular panels. The upper left panel are for initial table positioning, it also contain the recover button for event when the table hit any of the four safety switches. The lower left panel is windows showing the status of the scanner. The upper right window is the main window used to control 1-D/2-D scan. The lower right window is for VNA setting.

In the first window, the movement type of the scanner can be displayed, possible types are:

1. **Calibration** (when doing positioning),
2. **X direction only scan** (when doing scan with X direction selected only),
3. **Y direction only scan** (when doing scan with Y direction selected only),
4. **Both directions** (when doing scan with both direction selected),
5. **Recovery** (when the system is trying to recover from emergency stop).

The second window shows the motions of scanner. Possible statuses are: **LEFT**, **RIGHT**, **UP**, **DOWN**.

The third window shows the progress of the scan or calibration. It shows **number in percentage form** while doing left/right positioning and scan, and it shows the text **moving** for up/down positioning.

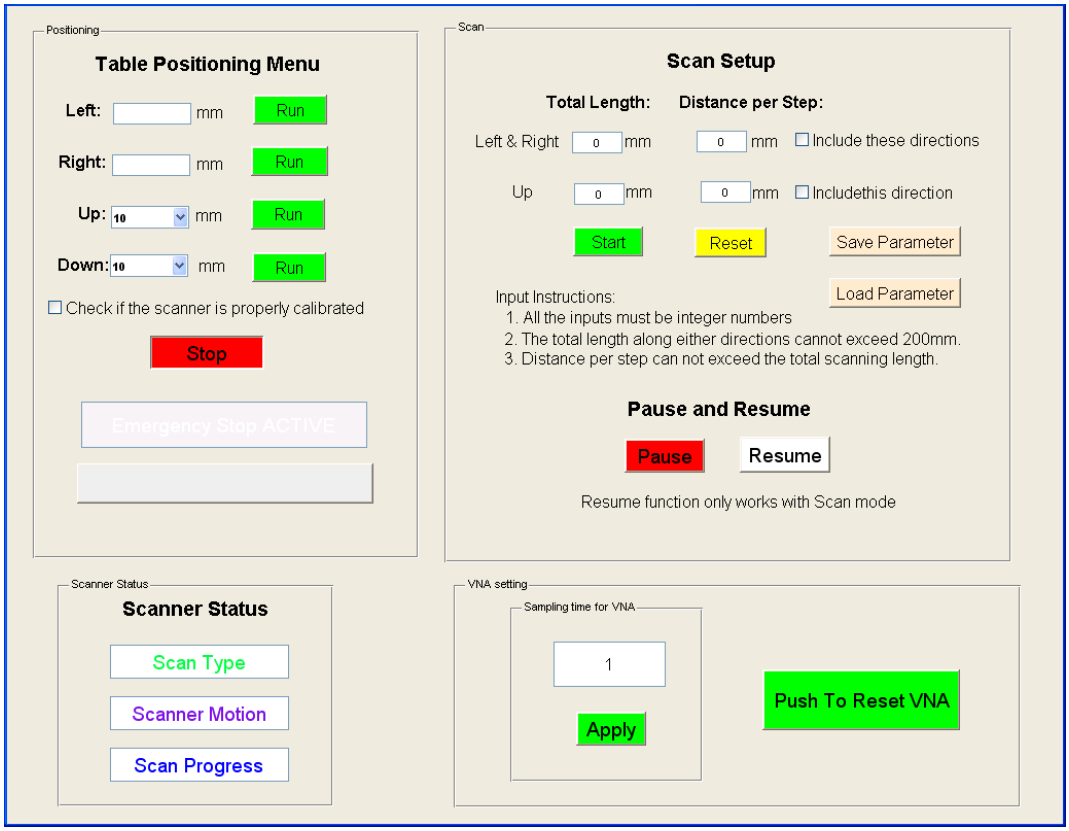

I. *For initial positioning of the table*

This section shows how to do initial positioning of the scanning table.

1. Open interface.m in Matlab and execute, the above window should appear. Turn on power supply.
2. Determine where the initial position of the table should be, and how much distance the table should move in any of the four directions (**Left, Right, Up, Down**).
   i. For **LEFT** and **RIGHT**, type in an integer number in the following windows and hit **Run**.

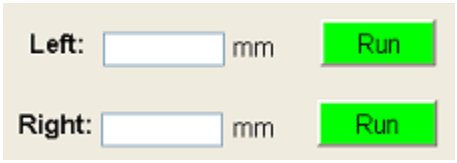

   ii. For **Up** and **Down**, select the distance from the **draw down window** and hit **Run**.

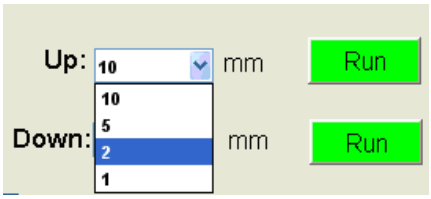

3. After initial positioning is done, check the **check box** shown below which will disable the **Run** buttons in this panel.

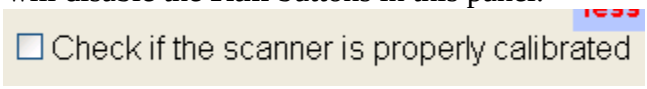

4. If you want to stop the movement of the scanner during the positioning process, hit the **Stop** button to abort the movement.

***** It is possible that the scanner would not move with the first button press because the relay has not been switched on. Simply press the button again so that the scanner starts moving.

II. *For table recovery from emergency stop*

When the table hits any of the four emergency switches, emergency stop is triggered cutting down the power supply. This section shows how to perform system recovery from such accident.

1. The inactive windows below the **Stop** button are used to indicate emergency stop status and perform system recovery. Normally, the window will be inactive as seen in the figure below.

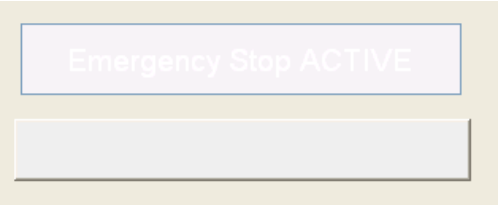

However, when emergency stop is triggered, the appearance of the windows changes to the figure below.

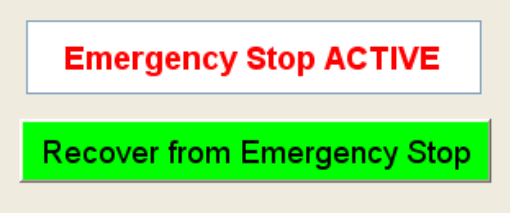

2. To perform system recovery, first check the **Scanner Status** panel. Make sure the scanner shows the status **Done** in the progress window before moving to the next step. You can also click **Stop** button to speed up the process.

3. Click the **Recover from Emergency Stop** button. The system automatically moves away from the pressed switch.
4. After the system is recovered, the windows indicating emergency stop status become inactive again.

In some rare situations, the **Recover from Emergency Stop** might not work as expected. In this case, one has to perform these alternative steps:

1. Shut down the power supply.
2. Pull the table away from the switch manually so that the switch is not pressed.
3. Reinitialize the software (close and reopen).
4. Turn on the power supply.

III. *For scanning*

This section shows how to perform a 1D/2D scan. For a 1D scan, the scanner moves along a line in either **Right** or **Up** direction. In a 2D scan, the scanner moves in a raster order. It first moves in **Right** direction, then **Up**, then **Left**, then **Up**, then **Right**, …, as shown in the illustration below. Since the movement is relative to the phantom, in reality the first point captured (origin) is the top right end of the phantom and the last point is the bottom left side of the phantom, as illustrated in the figure below.

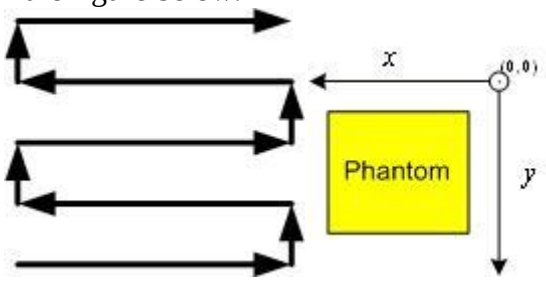

1. Before scan start, VNA should be set correctly. The VNA parameters can be specified in the Matlab file "vna_settings.m". After the m file is set, press **Push To Reset VNA** button to apply the settings to the VNA.

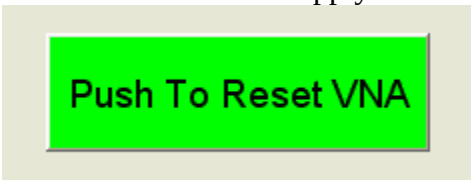

2. Also, depending on the VNA settings of resolution bandwidth (RBW) and the averaging numbers, the measuring time need to be set accordingly. Simply type in the time anticipated for measurement at a single point and press **Apply**. The unit is in seconds. **Please take special note that even if you don't need to change the time before two consecutive measurement, you need to press Apply once before the next measurement.**

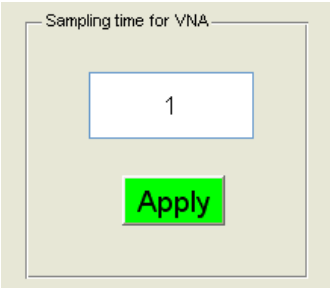

3. The two windows to the left under **Total length** show the maximum range the scanner will move in **Right** and **Up** directions. The two windows under **Distance per Step** show the distance the scanner will travel between two consecutive measurements. (The figure is on the next page).

4. Type in desirable numbers in these four windows (limitations are listed under input instructions), and select the scan directions you want to include in the scanning process by checking the check boxes. By selecting only one check box, the scanner will perform 1D scan. By selecting both check boxes, the scanner will perform 2D scan in the sequence described above.
5. Click **Start** to start the scan. The status of the scan can be viewed from the **Scanner Status** panel.

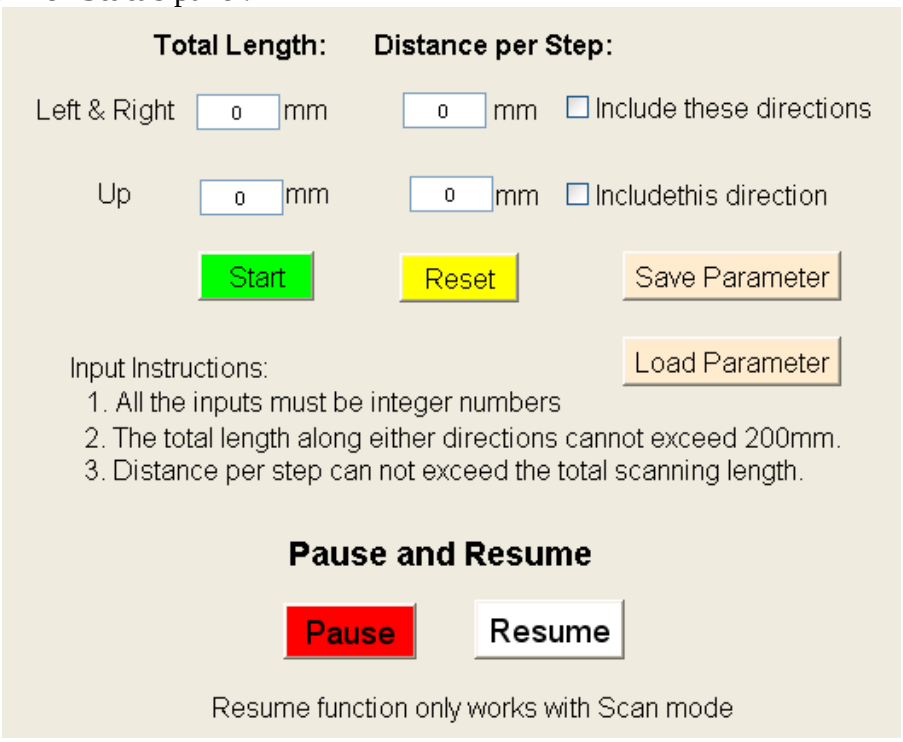

6. During the scan, you can always pause the scan by pressing the **Pause** button, after which, the Resume button becomes active. Click the **Resume** button resume the scan process.

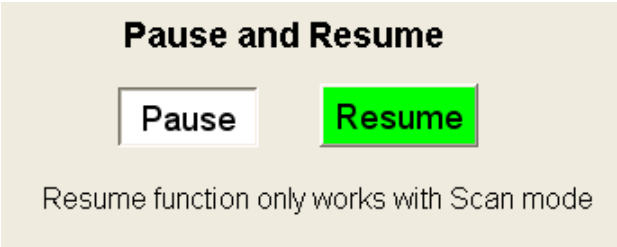

7. The measured data is saved in D://MyData folder in the VNA in csv format. **Please make special note to empty the folder every time for new data to be written in the next measurement.**

8. The **Save Parameter** and **Load Parameter** buttons just provide a simple way to save the parameters that are entered in the fields. A txt file named saved_parameter.txt is created under the execution directory containing the saved parameters.

APPENDIX C
DIELECTRIC PROPERTIES OF PHANTOM USED IN MEAUSREMENTS

C.I. Dielectric properties of low-loss target phantom used in section 3.4 and section 4.2.1

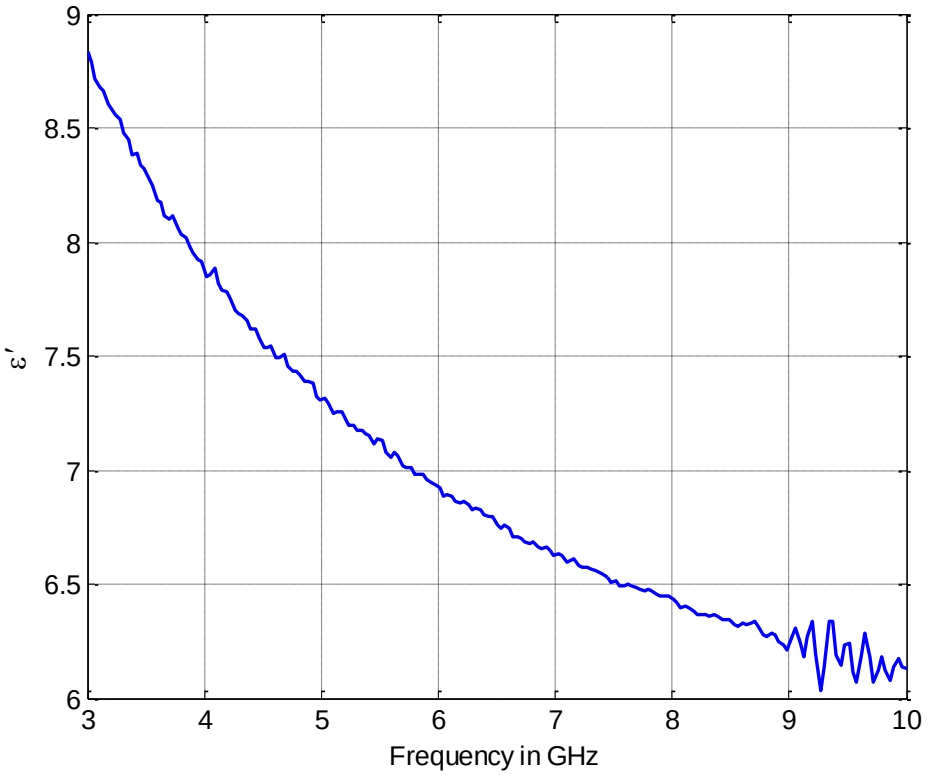

Fig. C.1. Relative permittivity of low-loss target phantom used in section 3.4 and section 4.2.1.

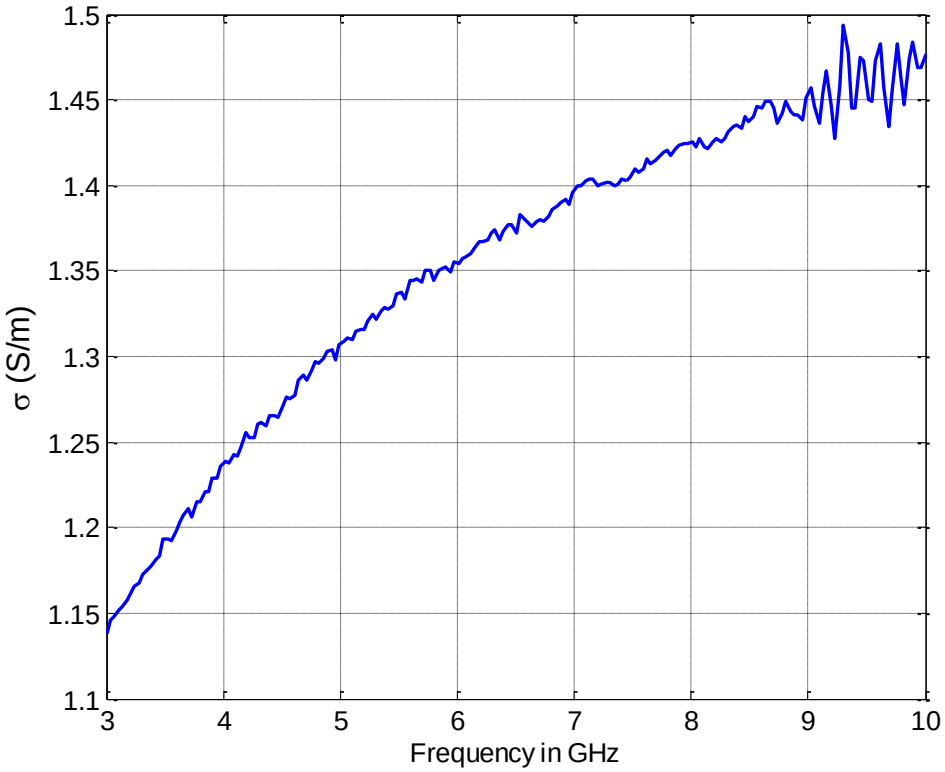

Fig. C.2. Conductivity of low-loss target phantom used in section 3.4 and section 4.2.1.

C.II. Dielectric properties of the low-loss background phantom used in section 4.2.2

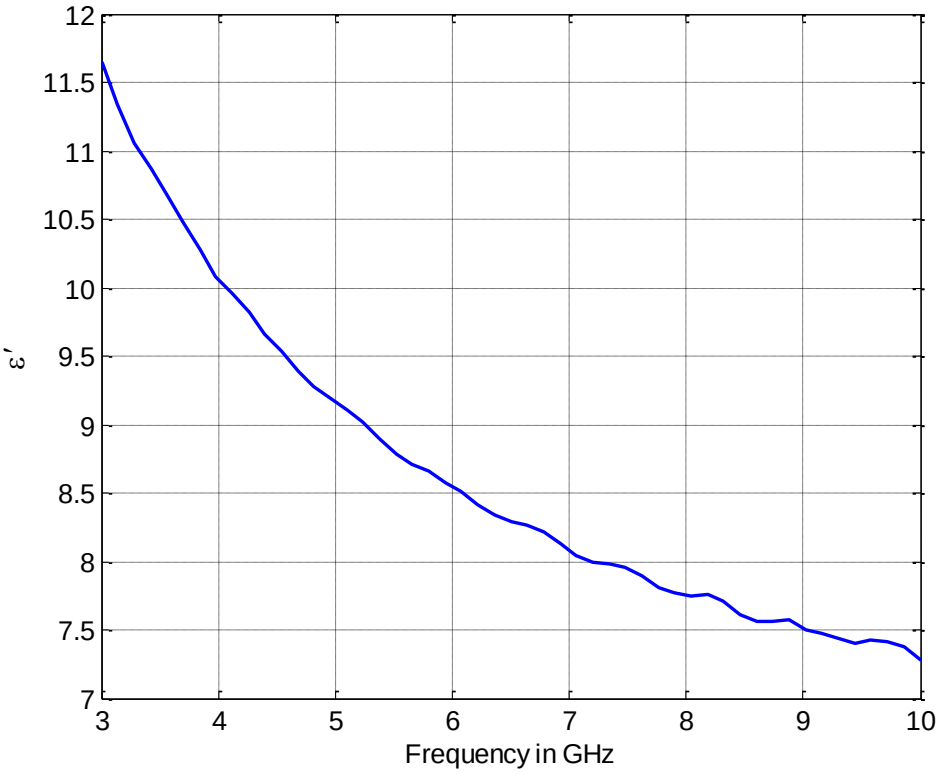

Fig. C.3. Relative permittivity of low-loss background phantom used in section 4.2.2.

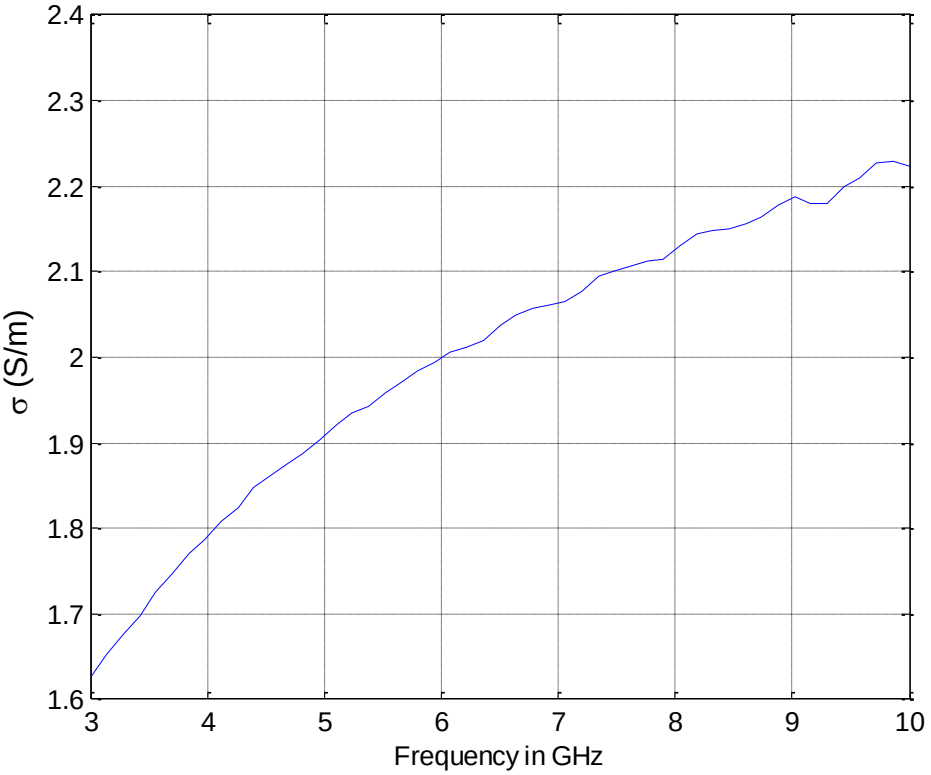

Fig. C.4. Conductivity of low-loss background phantom used in section 4.2.2.

C.III. Dielectric properties of the high-loss background phantom used in section 4.2.3

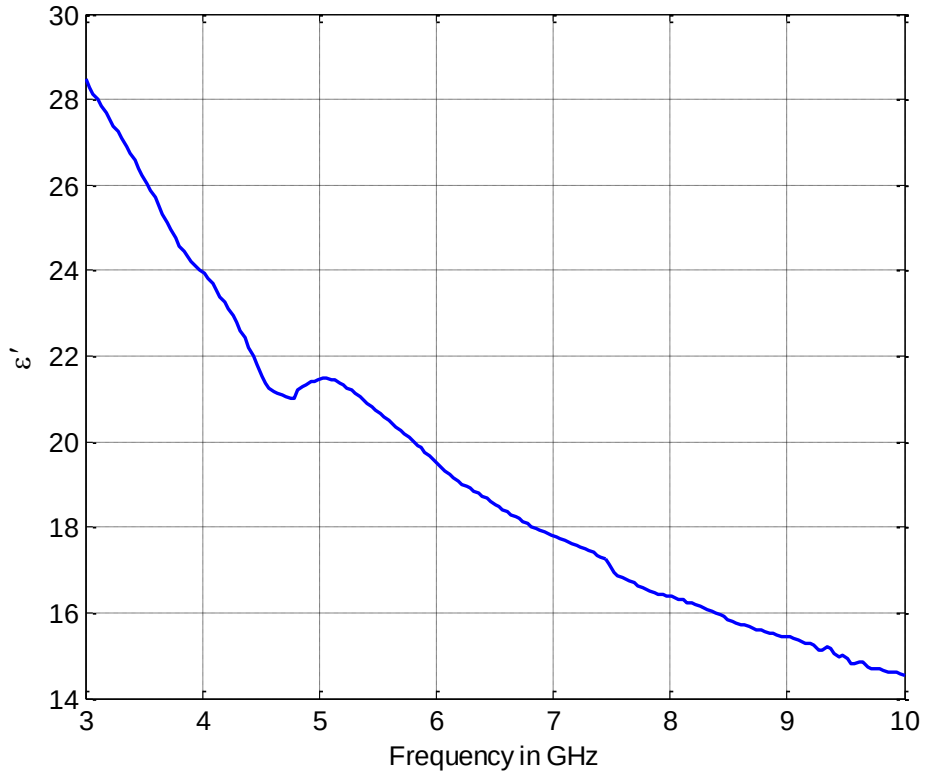

Fig. C.5. Relative permittivity of high-loss background phantom used in section 4.2.3.

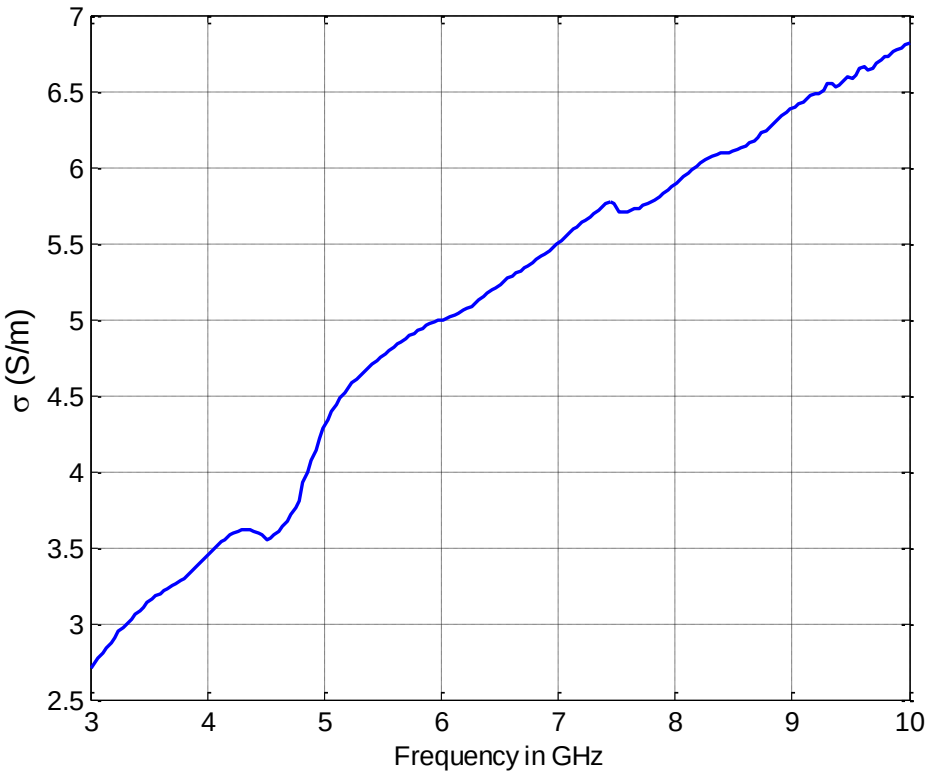

Fig. C.6. Conductivity of high-loss background phantom used in section 4.2.3.

BIBLIOGRAPHY

Advantest: R3860A/3770R3768 Operation Manual, Manual FOE-8440128F01, Advantest Corporation, Aug. 2003.

Agilent: Fundamentals of RF and microwave noise figure measurements, Application Note 57-1, Agilent Technologies, [Online] http://cp.literature.agilent.com/litweb/pdf/5952-8255E.pdf

R.K. Amineh, K. Moussakhani, H.H. Xu, M.S. Dadash, Y. Baskharoun, L. Liu and N. K. Nikolova, "Practical issues in microwave raster scanning," *Proc. of the 5th European Conference on Antennas and Propagation (EUCAP 2011)*, pp. 2901–2905, April 2011.

R.K. Amineh, M. Ravan, A. Trehan and N.K. Nikolova, "Near-field microwave imaging based on aperture raster scanning with TEM horn antennas," *IEEE Trans. Antennas and Propagation*, vol. 59, no. 3, pp.928–940, Mar. 2011.

Ansoft HFSS ver. 12, Ansoft Corporation, 225 West Station Square Drive, Suite 200, Pittsburgh, PA 15219 USA, 2011. [Online] http://www.ansoft.com.

J.-C. Bolomey and C. Pichot, "Microwave tomography: From theory to practical imaging systems," *Int. Journal of Imaging Systems and Technology*, vol. 2, pp. 144–156, 1990.

F.-C. Chen and W.C. Chew, "Time-domain ultra-wideband microwave imaging radar system," *Proc. of IEEE Instrumentation and Measurement Technology Conference 1998 (IMTC '98)*, vol. 1, pp. 648–650, May 1998.

F.-C. Chen, W.C. Chew, "Microwave imaging radar system for detecting buried objects," *IEEE International Geoscience and Remote Sensing Symposium 1997 (IGARSS '97)*, vol. 4, pp. 1474–1476, Aug 1997.

EEWeb Electrical Engineering Community. *25-pin Parallel Port pin Assignments* [Online]. http://www.circuit-projects.com/control-circuits/parallel-port-used-to-control-peripheral-electronics.html

M. Elsdon, M. Leach, S. Skobelev and D. Smith, "Microwave holographic Imaging of breast cancer," *2007 Int. Symp. Microwave, Antenna, Propagation and EMC Technologies for Wireless Communications*, pp.966–969, Aug. 2007.

D. Flores-Tapia, G. Thomas and S. Pistorius, "A wavefront reconstruction method for 3-D cylindrical subsurface radar imaging," *IEEE Trans. Image Processing*, vol. 17, no. 10, pp. 1908–1925, Oct. 2008.

H.A. Haus *et al*., "Description of the Noise Performance of Amplifiers and Receiving Systems," Sponsored by IRE subcommittee 7.9 on Noise, *Proc. of the IEEE*, vol. 51, no. 3, pp. 436-442, March,1963.

M. Hiebel, *Fundamentals of Vector Network Analysi.* Munchen, Germany: Rohde & Schwarz, 2005, pp. 84-85.

G. Junkin and A.P. Anderson , "Limitations in microwave holographic synthetic aperture imaging over a lossy half-space," *IEE Proc. F Communications, Radar and Signal Processing,* , vol. 135, no. 4, pp. 321–329, August 1988.

A. Khalatpour, R.K. Amineh, H.H. Xu, Y. Baskharoun, N.K. Nikolova, "Image quality enhancement in the microwave raster scanning method," *International Microwave Symposium (IMS 2011)*, June 2011.

H. Kitayoshi, B. Rossiter, A. Kitai, H. Ashida and M. Hirose, "Holographic imaging of microwave propagation," *IEEE MTT-S Int. Microwave Symposium Digest*, vol. 1, pp. 241–244, 1993.

M. Klemm, I.J. Craddock, J.A. Leendertz, A. Preece, and R. Benjamin, "Radar-based breast cancer detection using a hemispherical antenna array—experimental results," *IEEE Trans. Antennas and Propagation*, vol. 57, no. 6, pp. 1692–1704, Jun. 2009.

LabView ver. 8.5, National Instruments Corporation, 11500 N MoPac Expressway Austin, TX 78759-3504 USA, 2011. [Online] http://www.ni.com.

L.E. Larsen and J.H. Jacobi, "Microwave interrogation of dielectric targets. Part I: By scattering parameters," *Med. Phys.*, vol. 5, No. 6, 1978, pp. 500–508.

L.E. Larsen and J.H. Jacobi, "Microwave scattering parameter imagery of an isolated canine kidney" *Med. Phys.*, vol. 6, pp. 394–403, 1979.

L.E. Larsen, J.H. Jacobi and C.T. Hast, "Water-immersed microwave antennas and their application to microwave interrogation of biological targets," *IEEE Trans. Microwave Theory Tech.*, vol. MTT-27, no. 1, pp. 70–78, Jan. 1979.

C.-H. Liao, L.-D. Fang, P. Hsu and D.-C. Chang, "A UWB microwave imaging radar system for a small target detection," *IEEE Antennas and Propagation Society International Symposium 2008 (APS 2008)*, pp.1–4, July 2008.

MATLAB™ 2010, The MathWorks Inc., 3 Apple Hill Drive, Natick, MA, 2010. [Online] http://www.mathworks.com/.

P.M. Meaney *et al*., "A clinical prototype for active microwave imaging of the breast," *IEEE Trans. Microwave Theory and Techniques*, vol. 48, no. 11, 2000.

R.D. Orme and A.P. Anderson, "High-resolution microwave holographic technique. Application to the imaging of objects obscured by dielectric media," *Proc. IEE*, vol. 120, no. 4, pp. 401–406, April 1973.

M. Pastorino, *Microwave Imaging*. Hoboken, NJ: John Wiley & Sons, 2010, pp.1–3.

D. Pozar, *Microwave Engineering*. 2nd ed., Canada: John Wiley & Sons, 1998, pp. 555-559.

D.M. Sheen, D.L. McMakin and T.E. Hall, "Three-dimensional millimeter-wave imaging for concealed weapon detection," *IEEE Trans. Microwave Theory and Techniques*, vol. 49, no. 9, pp. 1581–1592, Sep 2001.